A THEORETICAL INVESTIGATION ON FORMATION DAMAGE MECHANISMS DURING HYDRAULIC FRACTURING

A Dissertation

by

RIZA ELPUTRANTO

Submitted to the Office of Graduate and Professional Studies of
Texas A&M University
in partial fulfillment of the requirements for the degree of

DOCTOR OF PHILOSOPHY

Chair of Committee, I. Yucel Akkutlu

Committee Members, John Killough

Marcelo Sanchez

Kan Wu

Head of Department, Jeff Spath

December 2019

Major Subject: Petroleum Engineering

ABSTRACT

The interactions between hydraulic fracturing fluid at lower temperature and salinity with the formation a cause non-uniform stress field. The formation experiences heat transfer to the fracture and local change in temperature, which in turn, leads to dynamically change in stress near the fracture. The changes in stress affects the formation porosity and permeability. Secondly, the chemical imbalance between the fresh fracturing water and saline formation water cause osmosis through semi-permeable clays in shale. Osmosis transfers the fresh water molecules, hence increases the net effective stress, which in turn leads to clay swelling. As a consequence formation porosity and permeability near the fracture could change. Finally, capillary end effect develops in tight gas and shale formations near hydraulic fractures as an additional formation damage mechanism during the flow-back of the treatment water and extends into the natural gas production period. It creates a high water saturation region inside the formation near the fracture.

This thesis investigates how the formation properties are sensitive to the non-uniform stress field changes during the shut-in period of hydraulic fracturing and during the flow-back, looking into the mechanisms of stress change and water saturation buildup near the hydraulic fracture. A new multi-phase flow numerical simulator coupled with chemo-thermo-poro-elastic geomechanical model is developed, which includes the thermo-elastic, chemo-elastic and capillary end effects, to understand the role of they play on the non-uniform stress field and saturation field development. The reservoir model has a matrix pore structure mainly consisting of a network of micro-fractures and cracks under stress. The simulation model yields high resolution water-gas flow in this network with a capillary discontinuity at the hydraulic fracture-matrix interface and predicts changes in formation porosity and permeability.

The simulation results show that the temperature difference and salinity imbalance between the formation and the fracture impacts the formation properties. The temperature difference reduces the mean normal stress of temperature which leads to lower porosity and permeability. Clay swelling has a reduction effect on the impact of temperature. The

capillary end effect causes significant formation damage during the production period by holding the water saturation near the fracture at levels higher than that due to water imbibition only. The effect makes water in the formation less mobile, or trapped, during the flow-back and tends to block gas flow during the production. The capillary end effect during the gas production is more important compared to the changing stress. The capillary end effect cannot be removed completely but can be reduced significantly by controlling the production rates.

DEDICATION

I dedicate this book to my beloved Family.

ACKNOWLEDGEMENTS

I would like to thank my committee chair, Dr. I. Yucel Akkutlu and my committee members, Dr. John Killough, Dr. Marcello Sanchez, and Dr. Kan Wu for their guidance, support and help throughout the course of this research.

Thanks also go to my friends and colleagues in Texas A&M University for their help, support and friendships.

Gratitude also goes to PERTAMINA, the Indonesia National Oil Company, which sponsored my studies at Texas A&M University.

Finally, I owe the greatest gratitude to my father and my mother for everything they have done. To my sisters, I appreciate and cannot thank enough for their love and support.

CONTRIBUTORS AND FUNDING SOURCES

Contributors

This work was supervised by a dissertation committee consisting of Professor I. Yucel Akkutlu [advisor], Dr. John Killough, and Dr. Kan Wu of the Department of Petroleum Engineering and Dr. Marcello Sanchez of the Department of Civil Engineering.

All work for the dissertation was completed independently by the student.

Funding Sources

Graduate study was supported by scholarship from PERTAMINA, National Oil Company of Indonesia.

NOMENCLATURES

A	Surface area [m^2]
A_{nm}	Flow surface between element n and m [m^2]
C	The trapping constant in imbibition relative permeability relationship
$C_a;\ C_c;\ C_s$	Anion, cation, and mean solute concentration
C_R	Heat capacity of the dry rock [J/kgK]
C_{EC}	Cation exchange capacity [mol/ m^3]
C_ϕ	Pore compressibility [Pa^{-1}]
D_β^κ	Free-diffusion coefficient of component κ in phase β [m^2/s]
E	Young's modulus [Pa]
F^κ	Flux term of component κ [kg/m^2s]
$F_\beta^\kappa\big\vert_{adv};\ F_\beta^\kappa\big\vert_{dif}$	Advective and diffusion mass flux of component κ in phase β [kg/m^2s]
g	Gravitational acceleration vector, [m/s^2]
H^{CH_4}	Henry's constant for CH_4
$h_A^{H_2O}; h_G^{H_2O}$	Water specific enthalpy in aqueous and gaseous phase [J/kg]
$h_G^{CH_4}$	CH_4 specific enthalpy in gaseous phase [J/kg]
h_β	Specific enthalpy at phase β
K	Bulk modulus of the elasticity [Pa]
$K_R; K_\beta$	Thermal conductivity rock and thermal conductivity at phase β [W/mK]
k	Absolute permeability [m^2]
	Crack permeability under stress [m^2]
k_0	Crack permeability at zero effective stress [m^2]
k_m	Permeability of porous medium acting as semi permeable membrane [m^2]

$k_{rg}; k_{ro}; k_{rw}$	Relative permeability of gas, oil, and water
$k_{rg}\|_{S_{iw}}$	Gas relative permeability at interstitial water saturation
$k_{rw}\|_{S_{gr}}$	Water relative permeability at residual gas saturation
$k_{r\beta}$	Relative permeability of phase β
L	The length of the grid block [m]
l_{IC}	Shape factor [m^{-2}]
m	Crack permeability model exponent
M^{κ}	Mass accumulation terms of component κ,
${M_w}^{\kappa}$	Molecular weight of component κ in phase β [kg/mol]
${M_w}^{CH_4}$	Molecular weight of CH_4 [kg/mol]
M_w^{salt}	Molecular weight of salt [kg/mol]
P	Pressure in the formation [Pa]
P_c	Capillary pressure [Pa]
P_{conf}	Confining pressure or overburden pressure [Pa]
P_d	Displacement pressure [Pa]
P_L	Pressure drop of entire grid block
P_1	Effective stress when the crack is completely closed [Pa]
$P_{A,I};\ P_{A,Clay}$	Aqueous pressure in inorganic micro-crack and clay pore [Pa]
P_β	Pressure of phase β [Pa]
$P^{CH_4}; P^{H_2O}$	Partial pressure of CH_4 and water [Pa]
$p_g; p_o; p_w$	Gas, oil, and water pressure [Pa]
$\check{p}$	Characteristic capillary pressure
$q_g; q_w$	Gas and water volumetric volume rate [m^3/s]
q^{κ}	Source/sink term of component κ [kg/m^3s]
R	Specific gas constant, equal to 0.461526 [kJ/kgK] or 8.3145 [J/mol K] or 0.082 [atm l/mol K]
$R_{ca\text{-}w}$, $R_{a\text{-}mw}$, $R_{ca\text{-}m}$	Ratio of the friction coefficients
r	Pore radius [m]

$R_n^{\kappa,k+1}$	Residuals of component κ of subdomain n at time k+1,
S_{gF}^*	Normalized "free" (mobile) gas saturation
S_{gi}^*	Normalized initial gas saturation
S_{gr}	Residual gas saturation
S_{iw}	Interstitial water saturation
$S_w; S_g$	Water and gas saturation
S_β	Saturation of phase β
T	Temperature [K]
T_r	Reduced temperature
t	Time [s]
V	Volume [m^3]
V_n	Volume of subdomain n [m^3]
w_A^κ	Mass exchange of component κ in phase β [kg/m^3s]
x	Distance from outlet boundary to the center of measured grid block [m]
X_i	Independent primary variable
x_β^κ	Mass fraction of component κ in phase β
y_β^κ	Molar fraction of component κ in phase β
$y_A^{CH_4}; y_G^{CH_4}$	Molar fraction of CH_4 in aqueous and gaseous phase
Z	Gas compressibility factor

Greek Letters

α	Effective stress or Biot's coefficient
β	Phase (aqueous and gaseous)
β_t	Pore thermal compressibility [K^{-1}]
	Linear thermal expansion coefficient

Γ_n	Surface area of subdomain n [m^2]
γ	Specific Gibbs free energy
γ^o	Ideal gas part of the Gibbs free energy
γ^r	Residual part of the Gibbs free energy
ε_{vol}	Volumetric strain
θ	Contact angle
κ	Component (H_2O, CH_4, salt)
λ	The pore size distribution index
λ_G	Thermal conductivity of gas phase
λ_r	Thermal conductivity of the rock
$\mu_g;\ \mu_o;\ \mu_w$	Gas, oil, and water viscosity [Pa s]
μ_β	Viscosity of phase β [Pa s]
$\overline{\mu_0};\ \overline{\lambda_0}$	Viscosity and thermal conductivity in the dilute-gas limit
$\overline{\mu_1};\ \overline{\lambda_1}$	The contribution to viscosity and to thermal conductivity due to finite density
$\overline{\mu_2};\ \overline{\lambda_2}$	The critical enhancement of viscosity and thermal conductivity
v	Dissociation coefficient of salt
	Poisson's ratio
ρ_β	Density of phase β [kg/m^3]
$\rho_g;\ \rho_w$	Gas and water density [kg/m^3]
$\rho_R;\ \rho_{Clay}$	Rock and clay density [kg/m^3]
$\rho_A;\ \rho_G$	Density in aqueous and gaseous phase
$\rho_A^{H_2O};\ \rho_G^{H_2O}$	Water density in aqueous and gaseous phase
$\rho_G^{CH_4}$	CH_4 density in gaseous phase
$\bar{\sigma}$	Mean normal stress [Pa]
σ	Clay membrane efficiency
	Interfacial tension between two immiscible fluids
τ_β	Tortuosity of phase β

ϕ	Porosity
ϕ_I, ϕ_{Clay}	Inorganic micro-crack and clay porosity
ω	Acentric factor
	Weighting factor

Subscripts

A; G	Aqueous phase (A), Gas phase (G)
$Clay$	Clay pore
n; m	Subdomain; grid block; element, inward unit normal vector
$init$; 0	Initial condition

TABLE OF CONTENTS

LIST OF FIGURES

Page

LIST OF TABLES

Page

1. INTRODUCTION

1.1. Background

Shale gas reservoirs received substantial recognition around the world as an alternative energy resource. EIA reported in 2013 that 95 basins with shale gas resource in 41 countries exist globally. In USA only, the total potential resources of natural gas from gas shale are estimated to range from 500 to 1,000 trillion cubic feet (Arthur et al., 2009). The success of the Barnett shale production has led to the development of other gas shale formations in North America such as Woodford, Fayetteville, Marcellus, and Haynesville. The favorable outcome of the Barnett shale play was due to contribution of horizontal drilling and hydraulic fracturing technologies.

Gas shale formations serve as the primary source rocks of hydrocarbon with varying degrees of maturity (i.e., heat exposure) as well as the reservoirs rocks. Shales are a heterogeneous sedimentary rocks consisting of a wide range of mineral composition, e.g., quartz, carbonates, feldspars and pyrites. They contain high clay-content (typically 40-60% vol/vol). Gas shale formations contain varying volumes of organic material also known as kerogen. Hydrocarbon gas is held in the pores of organic and inorganic materials; whereas the formation water in the inorganic material, mainly in the pores associated with the clays. The hydrocarbons in shale gas formations are dry gas which is primarily composed of at least 90% methane, although some shales, such as Eagle Ford, produce wet gas, condensate, or oil.

The production profile of shale gas wells show a large production rate at early time followed by a sharp decline. The decline rate at the first year of production can reach up to 90% of that recorded at the first day (Wasaki and Akkutlu, 2015). There are three factors, which make shale gas production economically viable (Arthur et al., 2008):

1. Horizontal drilling,
2. Multi-stage hydraulic fracturing,
3. Rapid increases in natural gas prices as a consequence of supply and demand.

Horizontal wells with multi-stage hydraulic fractures have been playing a key role in improving gas recovery in shale reservoirs. Soliman and Azari (1996) and many other argued that the most effective horizontal well completion suitable for the development of shale gas reservoirs is multiple-fractured horizontal wells because of the following reasons:

1. Restricted vertical flow due to the existence of shale streaks or low vertical permeability;
2. The existence of natural fracture in a direction different from that of induced fractures. So the hydraulically-induced fractures intercept the natural fractures in the formation;
3. Low hydrocarbon yield of the shale gas reservoirs due to low formation permeability;
4. Low stress contrast between the pay zone and the surrounding formations.

The direction of a horizontal well should be parallel or close to parallel, to the maximum in-situ principal stress so that the best well productivity can be achieved. With this direction, the completion engineers ensure that the fracture created will be near perpendicular to the borehole axis. This makes the hydraulic fracture created longitudinal and has a similar behavior to a vertical well.

The key to success in developing a shale gas reservoir is to create large and complex fracture network which integrates with a large reservoir volume (Mayerhofer et al., 2010). Hence, the hydraulic fracturing is required to deliver the most efficient and enhanced production from the ultra-tight shale gas reservoirs economically. The fracturing has been widely used as a proven technology to increase the gas well productivity for low permeable reservoirs since its first operation which was conducted on gas well in the Hugton Field, Kansas, USA in 1947 (Mueller et al., 2012).

Hydraulic fracturing can be used to prevent natural barriers in the formation, for instance a reduced permeability due to near-wellbore damage or the low permeability regions which are commonly present in shale formations. The goal of the stimulation is to

establish fractures or artificial cracks with much higher conductivity than the undisturbed formation, so that high-rate flow paths are constructed through which gas flows from the matrix formation to the well and improve the flow convergence in the reservoir. The fundamentals involving in creating such fracture is by pumping pressurized fracturing fluid with gels into the reservoir to overcome the minimum in-situ stress in the formation and initiate the fracture propagation.

1.2. A Brief Description of the Hydraulic Fracturing Operation

Hydraulic fractures can be divided into three categories (Fisher et al., 2005):

- A simple fractures, which can be described as a single bi-wing planar fractures with wellbore at the center of the two wings.
- Complex fractures.
- Very complex fractures.

Bi-wing planar fracture is common in conventional reservoirs (Weng et al., 2011). The latter category allows a fractured fairway to be created during a treatment with many fractures in multiple directions. Studies from the fields report that the hydraulic fracturing operations in unconventional reservoirs such as Barnett shale (Fisher et al., 2005; Warpinski et al., 2009) and Haynesville shale (Fan et al., 2010) are more likely to create very complex fracture systems rather than the bi-wing planar fractures. Warpinski et al. (2009) further separated the very complex fractures category into a complex fracture with fissure openings and complex fracture network. **Figure 1** illustrates how these fractures appear in the unconventional formations.

In the hydraulically fractured area, complexity is related with the interaction of the hydraulic fracture with a pre-existing rock material; for instance, cleats, fissures, or natural fractures (Cipolla et al., 2008). Complexity mostly grows due to excessive fluid leak off and/or reduced fracture width. In addition, the authors suggested that the hydraulic fractures growth can be categorized into four type:

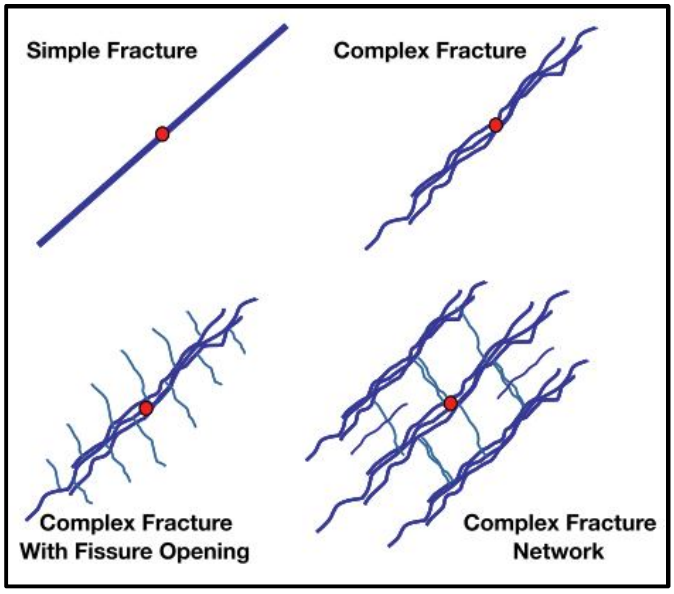

Fig. 1 – Schematic diagrams of levels of fracture complexity. Reprinted from Warpinski et al. (2009).

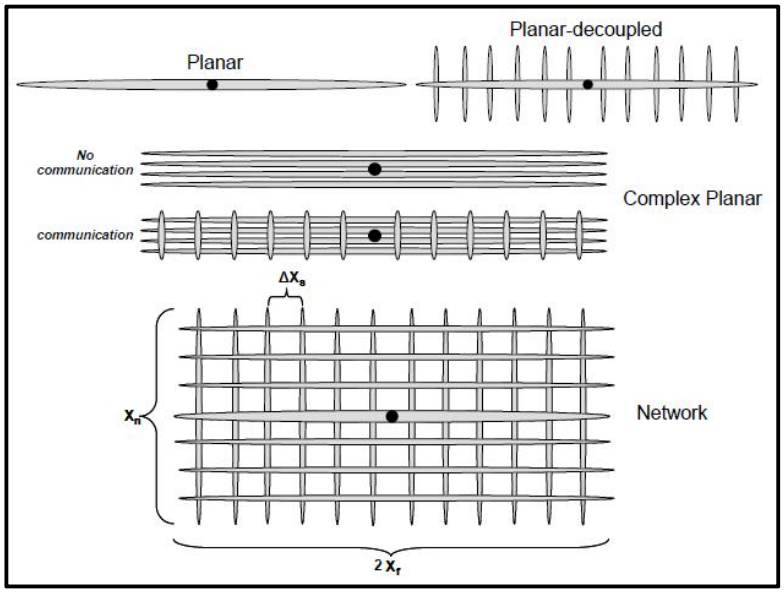

Fig. 2 – Schematic diagrams of complex fracture growth and complex scenarios. Reprinted from Cipolla et al. (2008)

- Planar-coupled growth.
- Planar-decoupled growth or fissure opening.
- Complex growth separated into communicating and non-communicating fractures.
- Network growth.

The illustration of the various type of fracture growth is shown in **Figure 2**. Two considerations during hydraulic fracturing are (Palisch et al., 2010):

1. Hydraulic fractures tend to reclose unless a propping agent is added.
2. Fracturing fluid initially injected needs to be viscous so that it can create appropriate fracture width for the proppant transport/replacement and minimal fluid leak-off.

Slick water, fresh water with friction reducing polymers, has been applied commonly as the primary fracturing fluid to create a more complex fracture geometry during the stimulation of tight gas and shale reservoirs (Palisch et al., 2010). However, as we will show in the following section, the implementation of the slick water brings in new formation damage considerations.

1.3. Formation Damage due to Hydraulic Fracturing

A hydraulic fracturing method used in shale reservoirs is different from in the conventional reservoirs. During the fracturing stimulation treatment, thousands of cubic meters of low-viscosity fluid (water) is pumped with up to 1 million pounds of proppants (i.e., frac-sand or ceramics) into the well. The injected water at high rate (around 75 – 150 bbl./ min.) applies the downhole force necessary for the fracture initiation and growth into the formation. The injection induces fracture complexity in the formation and places low-concentrations of proppants. Then the treatment is followed by a shut-in period, which could be a day, a few days, or occasionally a few months long. (Cipolla et al., 2010; Wang and Leung, 2015; Mcclure, 2016).

Following the treatment and the shut-in period, the well is produced and the injected fluids are flowed back to the surface. Only a small fraction of the injected water can be recovered, however, during the flow-back (Cheng, 2012). The volume of the recovered water may range from as low as 5% in the Haynesville shale to as much as 50% in certain areas of the Barnett and the Marcellus shales (King, 2012; Pagels et al., 2012). The recovery of the injected fluid during the first few months of production is typically in the range of 10 – 20% (Fan et al., 2010; Makhanov et al., 2012; Pagels et al., 2013). Hence, a large portion of the water is left behind in the fractures as the residual water. Generally, about 5 million gallons of fracturing water are injected into one horizontal well. With the average of treatment water recovery of 20% that means that about 4 million gallons of fracturing water "disappear" in the formation during the treatment (Pagels et al., 2012).

The large portion of injected water stays behind in the fracture and the rest of the water lost to the formation creates a region of fluid invasion and high-water saturation as shown in **Figure 3.** Water invasion into the formation begins when the injected water contacts the formation during hydraulic fracturing and continues after the fracturing during the shut-in and flow-back. The formation damage is mainly triggered by this first contact of the fracturing water with the formation and the subsequent invasion.

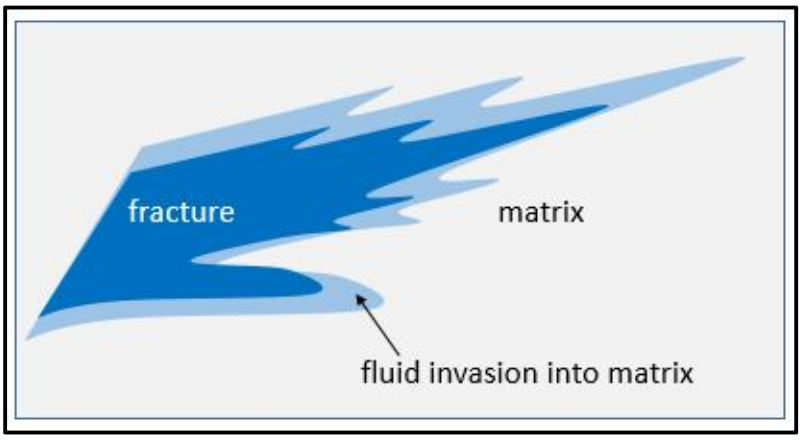

Fig. 3 – Diagram showing the invasion of the fresh slick water into the formation.

In their study, Pagels et al. (2012) presented three possible mechanisms of the fracturing water remaining in the formation. First, the closing of the fracture network in the direction of the highest stress due to fluid pressure drop in the fracture at the end of hydraulic fracturing. This situation prevents the water at the outer end of the fracture connect with the main part of the fracture. Second, the branching fractures, which are usually small, creates large capillary forces in the shale formation. This results in an amount of water transported from the main hydraulic fracture spontaneously into the interconnected fracture network and remain therein. Third, the shale matrix has small pores, which provide large capillary pressure in the pore network within the matrix, which gives major contribution on the imbibition process.

The last mechanism is discussed by several other studies. They argued that, during the treatment, forced imbibition of the fracturing water into the water-wet clayey inorganic portion of the formation as a major reason for the fracturing fluid loss and for the low levels of flow-back rates (Bennion and Thomas, 2005; Shaoul et al., 2011; Cheng, 2012; Eveline et al., 2017).

Shale reservoirs with multi-scale pore network could have significant molecular diffusion and water imbibition compared to the high- porosity and -permeability sandstone (Shen et al., 2016). Shale matrix, micro-cracks, and fractures could imbibe a portion of the unrecovered fracturing fluid because of the capillary forces. Fracturing fluid in shale also has tendency to penetrate deep into the matrix even after the initial imbibition takes place. Scott et al. (2007) and Zhou et al. (2015) showed that spontaneous imbibition of fracturing fluid into the shale matrix could impair and severely reduce the permeability of the shale matrix through clay swelling and dispersion.

Another complication that comes in due to cold water injection during the hydraulic fracturing. A volume of fracturing fluid with a cooler temperature than the formation temperature is injected into the formation during hydraulic fracturing. A region of changing temperatures will be formed near the fracture. When the matrix adjacent to the fracture cools due to injection of colder water, the rock has tendency to contract, or shrink. This process reduces the initial rock compressive stress and builds tensile stress in

the cold region. The thermo-elastic stress may decrease about 11 psi/^{o}F during the cooling and grow linearly with the temperature change during the heat transfer (Svendson et al., 1991).

In addition, during shut-in period, the cooler fracturing fluid in the formation experiences changes in the saturation distribution due to capillary forces that change with temperature due to heat transfer from the reservoir. The temperature of the fracturing fluid increases over time. The latter effects could further change the stress field and decrease the tensile stress near the fractures in an un-predictive way, which may cause further implications to the subsequent production period. Because of the reduction in stress during the shut-in, the reservoir properties such as porosity and permeability near the fracture could dynamically change.

In other situations during the shut-in, the injected fracturing fluid may damage the formation near the fracture due to chemical effects (Fakcharoenphol et al., 2016). These effects are caused by the chemical potential imbalance between the fracturing water and the formation water. The fracturing water is low-salinity, meanwhile, the brine trapped within clay sheets are high-salinity. The salinity contrast between the two water leads to a substantial osmotic pressure gradient. Once low-salinity water imbibes and contacts the clay surfaces, the water molecules will diffuse through the nano-pores within the clay aggregates in shale. During the diffusion, the clays act as a semi-permeable membrane, which cause diffusion to build up the clay pore pressure and trigger the clay swelling. The increase in clay pore pressure changes the local stress further and drive the fracturing fluid further into the shale matrix through the surrounding fractures in the network. (Eveline et al., 2017). The chemical damage may affect the stress in the invaded zone and contribute to reduction in formation permeability. In the end, it leads to deplete gas production and well performance. However, this observation is under isothermal conditions which means the impact of temperature change on porosity and permeability is neglected.

In tight formation, chemical and thermal effects have contribution on the fluid movement that are several times bigger than hydraulic fluid transport (Ghassemi and Diek,

2002). Several evidences have been recorded in the literature that chemical and thermal effects have significant role in the alteration of shale properties. The experimental results of Dirksen (1969) observed a significant mass transport through clays due to a temperature gradient. Another study of Chen et al. (2003) investigated the role of chemical effect and thermal diffusion on pore pressure reduction and stress accretion during cooler mud injection in drilling operation. All these studies were mainly related to drilling operation. Work by Perkins and Gonzales (1984) indicated that the changes in stress by injecting cool water into hot formation caused reduction in the hydraulic fracturing pressure. However, the result did not include the osmosis pressure and was conducted during the injection period only.

The interaction between the fracturing fluid and the formation fluid causes a non-uniform stress field, which in turn leads to formation damage. The non-uniform stress field occurs due to temperature difference or salt concentration imbalance, which may change how the water volume is distributed in the formation. In field operations involving shale gas reservoirs, long well shut-in period after hydraulic fracturing is believed to improve the reservoir permeability. However, the impact of this interaction is recorded after several months of shut-in period and in particular with high maturity source rocks. Taylor et al. (2009) argued that shut-in time is important for regaining the permeability after leak-off. Further, long shut-in can disperse the water deep into the formation. However, Bostrom et al. (2014) showed that the increasing permeability due to well shut-in is only observed in certain areas. Another study shows that shut-in can have a negative effect and reduce the fracture-matrix connectivity (Noe and Crafton, 2013). In addition, if the well is shut too long, it will give significant negative economic impact because of significantly delayed production.

Therefore, the impact of non-uniform stress field due to temperature and chemical imbalance between fracture and formation, specifically during the shut-in period of hydraulic fracturing on shale formation needs to be investigated so that we can develop a better understanding of the production issues.

The imbibition and the non-uniform stress field due to temperature and chemical imbalance during shut-in period is not the only formation damage mechanism responsible for the fracturing fluid loss. The injected water to the formation may cause the high water saturation, which may lead to liquid blocking during the gas flow. The liquid blocking is the unfavorable saturation condition that holds back the gas near the fracture during the production (Shaoul et al., 2011). The liquid blocking may result in significant loss in gas relative permeability. The liquid region may not only lead to the tensile stresses or to the swelling of the clays (Scott et al., 2007; Eveline et al., 2017) but also to the capillary end effect. These studies have previously shown the potential flow impairment mechanisms in tight gas and shale formations and discussed, to a certain extent, that they may influence a well performance during the production. However, they did not consider the existence of capillary end effect near the fracture-matrix interface.

In ultra-low permeability formations, such as tight gas and shale, the sizes of the pores and cracks contributing to the transport of fluids are significantly reduced. Hence, once the fresh fracturing water invades, the formation experiences large gas-water capillary pressure. Consequently, the two-phase flow dynamics during the flow-back could be controlled by the capillary forces. In the presence of strong capillarity in the formation, the capillary discontinuity occurs near the fracture-matrix interface during flow-back of hydraulic fracturing operation, which causes accumulation of the water and creates CEE. As a result, the distribution of water saturation along the formation become non-uniform. CEE will retain the injected water within the formation during flow-back and production period. This retention could cause high levels of immobile water saturation near the fracture and significantly amplify the liquid blocking in the formation. Therefore, CEE during production from hydraulically-fractured tight gas wells needs to be investigated in order to have a better understanding of the well's productivity.

1.4. Conceptual Shale Gas Formations Petro-physical Model

Shale is a sedimentary rock that contains fine-grained particles including clay minerals (Passey et al., 2010). The fine-grained particles build the lower end of the multi-scale,

multi-porosity nature of the shale matrix. The shale matrix mostly contains of quartz, carbonates, feldspars, pyrite, kerogen, and clay minerals. Some measurements in both laboratory and regional studies have obtained permeability of shale in the range of 10^{-23} and 10^{-17} m^2 when porosity is between 0.1 and 0.4, respectively (Neuzil, 1994). Meanwhile, porosity in gas shale formations ranges from 2 to 10% (Curtis, 2002). Commonly, high quality shale gas formation has high initial gas saturation and low initial water saturation, e.g., less than 30% (Boyer et al., 2006; Stoneburner, 2009). This low water saturation causes a strong capillary suction of water which prevents water from flowing (Wang et al., 2009).

There are three ranges of pore sizes in the shale formation. The macro-pores, which have size more than 50 nanometers (nm), mostly consist of fractures, micro-fractures and cracks, and the inter-particle space between aggregates of clay. The meso-pores, which have diameter from 2 to 50 nm, are predominately the space between clay particle and within kerogen. The last type has diameter less than 50 nm and comprise mainly of kerogen pores and inter-crystalline pore between clay platelets and is called micro-pores. The matrix pores within gas shale formation consists of nano-scale pores within the categories of micro-, meso-, and macro-pores (Davies et al., 1991; Bustin et al., 2008). Productive gas shale system contains round shape organic pores, micro-cracks, and clay pores, (Wasaki and Akkutlu, 2015; Eveline et al., 2017) as shown in **Figure 4.** Meanwhile, the interaction between these pores and the dominant transport mechanisms are shown in **Figure 5.**

Kerogen in gas shale formations has porosity that is five times larger than the porosity associated with the inorganic material (Wang et al., 2009). The porosity of organic matter ranges from 0 to 25% (Reed et al, 2007). The fragment of organic material can be acted as a separate porous medium in shale formation. The organic pores within the kerogen is stored as adsorbed gas and free gas, which increase linearly with total organic content (TOC).

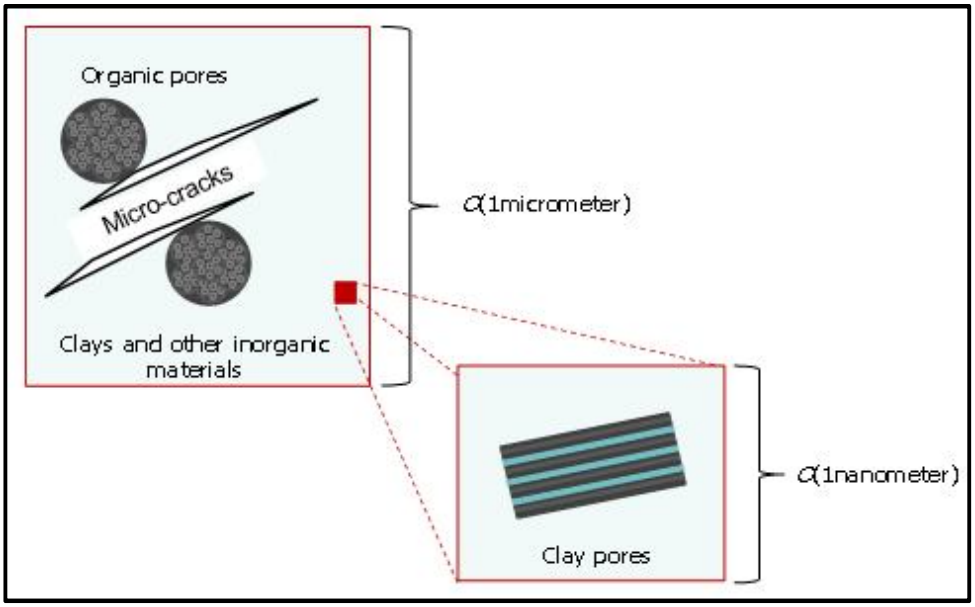

Fig. 4 – A shale formation model contains organic and, inorganic micro-cracks and clay pores (Adopted from Eveline et al., 2017).

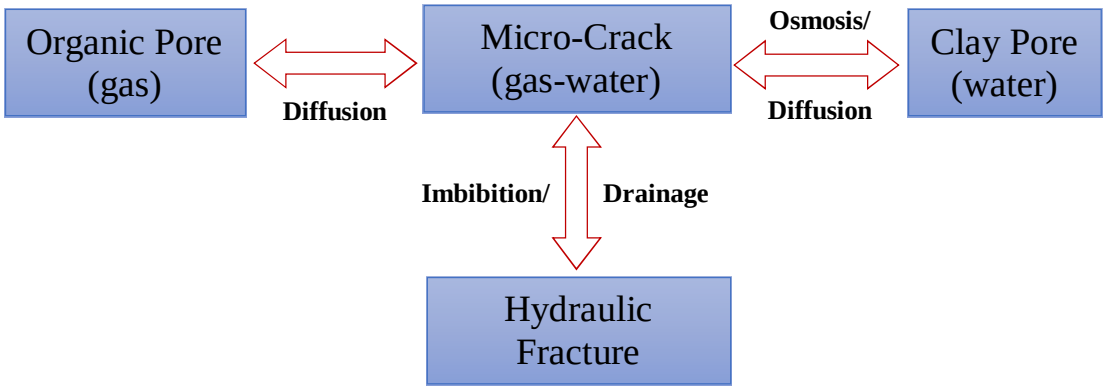

Fig. 5 – Flow paths among hydraulic fractures and organic pores, micro-crack, and clay pores, and the dominant flow/transport mechanisms and fluids.

A large portion of the kerogen pores is nano-scale with pore sizes ranging from 5 to 1,000 nm (Reed et al, 2007). Pore spaces are roughly estimated to have formed by thermal maturation when hydrocarbon fluids were generated over the geological time scale. Organic pores are oil- or gas-wet and works as nano-filter of hydrocarbon transport. Therefore, hydrocarbons flow through organic material are predominantly a continuous single-phase without residual water (Perrodon, 1983). Permeability values in organic-rich gas shale formation ranges from nano-Darcy to tens of nano-Darcy (Soeder, 1988; Davies et al., 1991; Guidry et al., 1996; Bustin et al., 2008). The organic pores could possibly be the hidden tortuous pathways to gas production when the kerogen pores connect to the natural or artificially induced hydraulic fracture.

The micro-fractures and cracks are located in the shale matrix. These are the secondary porosity developed, when the generated hydrocarbons maintain pressure in excess of the local hydrostatic pressure. They follow orientation perpendicular to the local minimum stress. Therefore, the micro-cracks have a narrow channel of micro-crack geometry with the length varies from one to ten micrometers. In contrast to the kerogen pores, micro-fractures and cracks are considered hydrophilic and has a strong affinity to water. Hence, apart from gas storage, water film is manifested as an irreducible water on the walls of the micro-fractures and cracks (Sun, et al., 2017). The micro-fractures and cracks can connect hydraulically to the organic pores and the other inorganic or clay pores.

Lastly, the clay pores are the spaces between interlayer clay sheets where the formation water bridges. The presence of clay pore in shale can be associates with the dominance of the illite-smectitic clay but some illite, montmorillonite, kaolinite, and chloride are also observed (Orangi et al., 2011; Kuila and Prasad, 2013). The affinity of shale for water is particularly influenced by the clay mineral type. For example, smectite adsorbs more water than kalinite or illite (Lal, 1999). The illitic-smectite group of clay pore are identified into different scale: meso-pores (diameter around 3 nm), large meso-pores or fine macro-pores (diameter around 50-100 nm), and micro-pores (diameter around 2000 nm). The smaller pores are lesser affected from stress changed (Kuila and Prasad, 2013). Clay pores have water and low permeability.

The formation water associated with clays is divided into different types. Inter-crystalline water with the cations. This water is able to neutralize the charges caused by the elemental substitution. Osmotic water corresponds with the clay surface charges and exists as an adsorbed surface layer. This is the water that is related to the swelling mechanism that occurs during the shut-in. Bound water is formed as structurally bonded hydrogen and hydroxyl groups. Under the extreme temperature condition, bound water will separate from the clay to form free water. Lastly the free water fills only the pore space between the grains (Lal, 1999).

1.5. Transport Processes and Their Relation to Stress

Micro-fractures and cracks are the main flow paths in tight gas and shale formations (Ougier-Simonin, 2016; Alafnan and Akkutlu, 2017). Therefore, the shale permeability is sensitive to the effective confining pressure varying by two to three orders of magnitude. This behavior is characteristically different than the sandstone permeability specifically at low confining pressure because of the presence of micro-cracks in the shale (Dong et al., 2010; Wasaki and Akkutlu, 2015). Moreover, the existence of water film not only reduces the apparent permeability but also increases the stress sensitivity of the shale permeability (Gensterblum et al., 2014).

1.5.1. Flow in Micro-Cracks and Gangi's Crack Permeability Model

In the shale formation, the non-uniform stress field develops and changes the shale permeability. The stress changes are due to the following reasons:

- Formation pore pressure change due to shut-in and production operations;
- Formation pore pressure change due to temperature imbalance;
- Clay pore pressure change due to osmosis of the fresh fracturing water;

One practical consequence of change in the stress is that the permeability of the micro-fractures and cracks could change dynamically during the shut-in, flow-back and production periods.

During the fluids withdrawal from the formation, the permeability decreases as the net effective stress ($P_{conf} - \alpha P$) increases. This phenomenon could be captured using Gangi's crack permeability model (Gangi, 1978; Wasaki and Akkutlu, 2015; Eveline et al., 2017).

$$k = k_0 \left\{ 1 - \left(\frac{P_{conf} - \alpha P}{P_1} \right)^m \right\}^3 \qquad (1)$$

Here, k_0 is the permeability at zero effective stress, P_{conf} is the confining pressure, α is the Biot's coefficient, m is the crack walls roughness coefficient, and P_1 is the effective stress when the cracks are closed completely.

1.6. Statement of the Problem

Gas shale formations with ultra-low matrix permeability are produced at economic rates using horizontal wells with hydraulic fractures. The main challenge in hydraulic fracturing in shale is a large volume of trapped water in the formation.

Water loss in the formation during extended shut-in time, right after the hydraulic fracturing, and during the flow back could lead to formation damage. The very tight pores in shale matrix cause the capillary pressure within the matrix become high. This environment forces the fresh water to imbibe spontaneously into the shale matrix. Several formation damage mechanisms could develop during the shut-in and flow back periods and exacerbate the situation by changing dynamically the characteristics of the fluid and rock properties of the shale formation, i.e., porosity, permeability, fluid saturations, capillary pressure, and relative permeability.

Understanding the fundamentals of shale/water interactions and the mechanisms affecting the reservoir system properties is crucial in order to design the field procedure during the operations. In this research, I am interested in studying the formation damage mechanisms involving fracturing water-shale interaction.

The first mechanism is the porosity and permeability alteration due to local stress change. The local stress is influenced by two major mechanisms. First mechanism is the temperature alteration occurring following the injection of the low-temperature fracturing fluid. I will investigate the stress behavior during the shut-in period following the cool water injection due to complex heat and mass transfer occurring near the hydraulic fracture. The second mechanisms is osmosis. The latter is induced by the difference of the salt concentration between the clay-bound water and the hydraulic fracturing water. Osmosis causes clay to swell which leads to stress build-up and further change the porosity and permeability.

The other mechanism, which is poorly understood, is the capillary end effect. The CEE develops during the flow-back, increases the water saturation near the fracture and creates liquid blocking. During the flow back period, the relative permeability to gas flow is reduced adjacent to the fracture. CEE in hydraulically-fractured tight gas and shale formations can be minimized during flow back and production by use of high flow rates. Nevertheless, allowing high rates of production may not be practical for some gas wells producing from highly over-pressured reservoirs since high rates could lead to mechanical significant mechanical damage to the formation and fractures. One practical application of this study is to identify the critical flow rate levels needed to minimize CEE.

In this study, I do not consider other potential mechanism that might cause the change in rock and fluid properties of the shale, including the closing of micro crack, the alterations of wettability, chemical adsorption, solids precipitation, clay dispersion, formation dissolution, and the osmosis mechanism induced by electrical potential gradient in the material.

1.7. Scope of the Work and Limitation

In this thesis I show that porosity and permeability alteration because of the non-uniform stresses and due to CEE play a major role on the trapping of the injected water in the tight gas and shale formations. A mathematical modeling and numerical simulation is used to build a newly-developed reservoir flow simulation model for the investigation of these problems. The procedure begins by building a conceptual petro-physical model for gas shale system involving multi-scale pore network. The procedure is followed by the development of a system of coupled governing equations for fluid, which is related to the petro-physical model.

The petro-physical model of shale matrix considers the major pore network of gas shale formations as shown in **Figure 5**. The pore network includes three pore types which are, organic pores, clay pores and inorganic micro-cracks. In this petro-physical model, the clay pores and the organic pores are directly connected each other to the micro-cracks. Meanwhile, the connection from clay pores and organic pores to the hydraulic fracture may pass through the micro-cracks, which makes the contribution of the transferred fluid mass insignificant. Since the cracks caused by the hydraulic fracturing tends to close in time, the fluid transfer to the hydraulic fracturing is going to disconnect when the micro-cracks are completely closed

After the process of building the petro-physical model, the next procedure is to set up a one dimensional problem to represent the invasion of the fresh slick water into the formation during shut-in and flow-back periods with the appropriate initial and boundary conditions as shown in **Figure 6.** One-dimensional models are useful to simplify the simulation on single channel flow during investigation of physical and chemical processes in the absence of multidimensional and geometrical effects. I need to setup initial and boundary conditions representative of the shut-in and flow-back periods. The initial/boundary value problem is then solved using a numerical simulation approach.

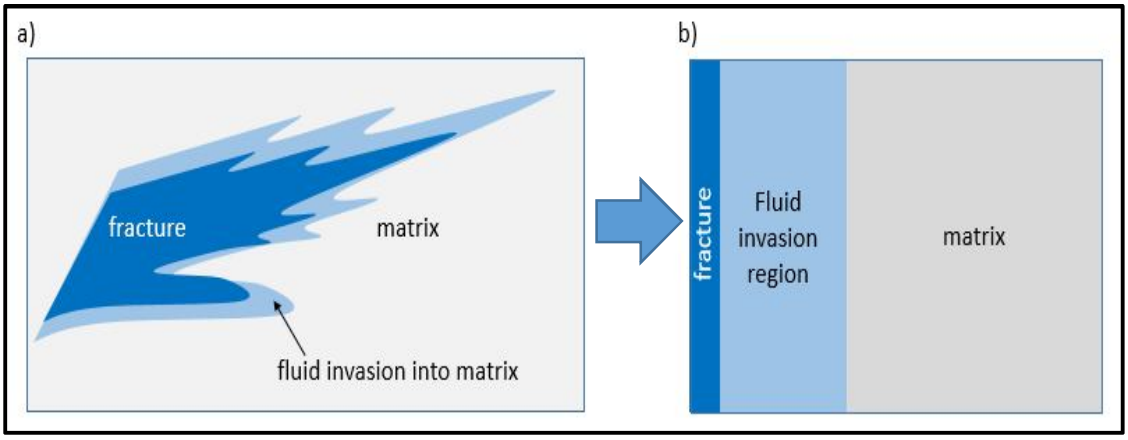

Fig. 6 – a) Diagram showing the invasion of the fresh slick water into the formation; b) One-dimensional representation used in numerical modeling of the invasion of the fresh slick water into the formation.

The numerical simulation is developed as an extension of TAMU-FTsim, the flow and transport simulator developed at the Lawrence Berkeley National Laboratory, which is based on the TOUGH+ code (Moridis et al., 2014). This simulator has been designed to provide the built-in capability for solving the traditional coupled equation of mass and heat balances for two-phase flow so that it can simulate flow and transport through porous media as long as Darcy's law is applied and the representative volume of the domain and subdivision can be defined. It considers, however, a uni-pore reservoir model with a constant porosity and permeability. Fluid flow and transport mechanisms in this simulation included advective and diffusion mechanisms. For my advanced study, I have modified the simulator significantly to include a multi-porosity medium and to consider the heat/mass exchange between the medium components along with the coupled mean normal stress, i.e., thermo-chemo-poro-elastic formulation. In addition, CEE correction has been added into the simulator. The numerical model for CEE includes chemo-poro-elastic formulation under the isothermal condition. I validated the modified simulator with previously published experimental works. The last step of this study is to run several

forward simulation cases that may develop in the field following the hydraulic fracturing operation.

In the first study, the reservoir parameters used for the investigation are introduced and a forward simulation study is performed to predict formation behavior during the well shut-in (or shut-in) period. The shut-in simulations are performed under non-uniform stress field due to temperature and chemical imbalance between fracture and formation. The changes in reservoir properties such as formation pressure, capillary pressure, water saturation, permeability are investigated near the fracture-matrix interface during the shut-in.

Next, for the second study, the water invasion into the formation is simulated. The invasion gives the necessary initial conditions of saturations and pressures for the subsequent simulation of the flow-back. The water invasion can be envisioned as the immediate shut-in period which follows the fracturing treatment. The impact of CEE during the flow-back and production is investigated and compared to the drainage of water from the formation without CEE. In addition, the critical flow rate levels needed to minimize CEE is identified in this study. The study was specifically conducted to understand the alteration that occurred to the shale and fluid properties near the fracture due to CEE during the flow-back and production. The study also quantifies the alteration impact on the water flow back and gas production during the first few months of production.

2. REVIEW OF THE FORMATION DAMAGE MECHANISM

Formation damage in shale gas reservoirs can occur during hydraulic fracturing operation because of the interaction between the fracturing fluid and the formation fluid near the fracture-matrix interface. This chapter discusses the mechanisms of formation damage in further detail, which are expected to induce water invasion into the formation and the formation properties change during the shut-in and flow-back periods, which trap the invaded fracturing water. I start with the imbibition, which, in my study develops with the first contact of the fracturing water to the formation, and followed by thermal and chemical effects. Later on, during the flow-back period, CEE takes over as the major formation damage mechanism.

2.1. Imbibition

Imbibition is the mechanism by which one immiscible fluid such as water displaces another immiscible fluid such as gas or oil in porous medium. Imbibition resulting from hydraulic fracturing can cause water invasion into the matrix, liquid blocking during gas flow, and clay swelling (Qin, 2007; Ghanbari et al., 2014). Imbibition mechanism is considered as the major reason of fracturing water invasion and penetration into matrix. The water invasion due to imbibition is also a reason for low water recovery during the production.

There are two types of spontaneous imbibition of water in shale. The first type is called co-current imbibition. In this imbibition, the wetting (water) and non-wetting (gas) phases flow in the same direction of main flow. Typically, the co-current imbibition is influenced by capillary and gravity forces as the primary driving force. In the second type, the wetting phase imbibes into the matrix and displaces the non-wetting phase out of the matrix, in our case out to the fracture. This imbibition is called counter-current imbibition. The counter-current imbibition is likely to reduce the formation damage caused by liquid blocking during hydraulic fracturing operation (Meng et al., 2015).

On their study in the Horn River shale formation, Makhanov et al. (2012) found that spontaneous imbibition was influenced by the matrix-fracture interface, shut-in time, fluid properties, and matrix mineralogy. Ghanbari and Dehghanpour (2014) added that, when the water imbibes into the formation, water induces micro-cracks, which are mainly oriented parallel to lamination. The micro-cracks later slightly expand and increase the porosity and horizontal permeability. Additionally, hydrophobic organic materials, which are oriented along the lamination, may hinder the water flow perpendicular to lamination. As a result, the water imbibition rate is higher when the fracture direction is parallel to lamination rather than perpendicular to the lamination. Furthermore, they observed that higher initial water saturation tends to decrease the water imbibition rate.

The imbibition rate is a function of fluid and porous medium properties such as viscosity, wettability, interfacial tension, relative, and absolute permeability (Zhang et al., 1996). The net effect of capillary pressure driving force and the opposing viscous resistance to flow dominates the rate of imbibition. The domination is affected by the water saturation (Zhou et al., 2014). Meanwhile, the imbibition volume is controlled by other factors, such as extraneous fluid chemistry, formation fluid chemistry, and rock mineralogy. The smallest pores next to the interface are usually invaded first due to strong capillary forces. In shale reservoirs, spontaneous imbibition mostly appears in micro-pores. The micro-pores can imbibe plenty of water from other pores, particularly the main flowing channels (Meng et al., 2015).

The initial water saturation in gas shale formations could be under the sub-irreducible saturation condition. The capillary pressure dominates the imbibition process when the water saturation is low. As injection water arrives to the pores, which contain native formation water, the whole reservoir system dynamically changes not only the water saturation and water salinity but also some of the rock properties. The capillary pressure becomes smaller along with the increased volume of imbibed fluid in the formation.

2.2. Thermo-Elastic Effect

Temperature variations can induce various changes and processes in shale reservoir system. The following sections describe the impact of thermal processes near the hydraulic fractures in the gas shale reservoirs.

2.2.1. The Impact of Thermo-Poro-Elasticity in the Formation

Several authors have investigated the relation between thermal effect and the poro-elasticity. Timoshenko and Goodier (1951) presented a thermo-elastic theory which described that the process of heating the wellbore tends to increase the compressive stresses around the borehole (as cited in Gonzales et al., 2004).

Later Perkin and Gonzales (1985) studied that the fracturing pressure can significantly drop in the formation due to large volume of liquid injection, which is cooler than the reservoir temperature.

Charles et al. (1996) argued that thermal conduction influences the formation temperature near the fracture during shut-in period. They showed that the impact of this conduction only slightly changes temperature distribution and does not have ability to warm up the reservoir formation. On the other hand, Tang and Luo (1998) explained that the tensile stress of the near-fracture is reduced in a gradual way during the shut-in period right after the injection of cold mud into a formation. These authors did not consider rapid invasion of cold fracturing water due to imbibition.

More recently, several authors created models which included thermal effects along with the effect of poro-elasticity. In general, they argued that the difference in thermal expansion of the shale and the formation fluids, along with differences in thermal and fluid diffusivities within the low-permeability shales, might cause a significant time-dependence of near-wellbore stresses and pore pressure. In addition, the radial and tangential stresses around the wellbore is likely to be affected over time by changes in the near-wellbore pore pressure. However, the studies neglect the contribution of convective

heat transfer from fluid movement, due to presence of imbibition. The heat transfer was due solely to conduction (Li et al., 1998; Choi and Tan., 1998; Yu et al., 2001; Chen and Ewy, 2003).

The largest impact of thermal effects occurs at early time. The injection fluid, which is colder than the reservoir, prevents shear failure of the formation at the early time because of the reduction of the pore pressure and compressive force near the fracture. On the contrary, the hotter temperature injection fluid increases the pore pressure and compressive force. It raises the risk of shear failure at the early times (Li et al., 1998). When the temperature in the fracture is lower than formation temperature, it reduces the effective fracture gradient. As a result, the formation parting pressure drops significantly (Chen and Ewy, 2003). During shut-in period following the cold fluid injection, the formation and the in-situ fluids warm the adjacent formations. In consequence, the compressive stress in the near-fracture increases which also leads to increase in the fracturing pressure. The longer the formation is heated, the larger temperature causes the fracture to close, as demonstrated in a case study from the Elgin Field in the UK North Sea (Maury and Idelovici, 1993). On the other hand, the reduction in the local stress occurs due to formation cooling near the fracture face.

Thermal processes can be influenced by several factors. The most significant factor that affects thermal processes is the specific heat capacity of the fracturing fluid. The heat transfer process such as convection and conduction also has great impact on the thermal processes. Since flow rate of injection influences both the heat transfer and the hydraulic energy by forced convection, the slight alterations in the flow rate will be followed by a significant changes in the wellbore temperature.

2.2.2. Temperature Contribution on Thermo-Poro-Elastic System

Shale has low permeability and because of that the fluid movement into the formation during hydraulic fracturing is not dominated by hydraulic transport. In fact, the thermal

effects has more significant contribution during hydraulic fracturing to efficient production because heat transfer in the formation takes place faster than the hydraulic diffusion. As a consequence, the alteration of temperature during early time of shut-in period will dominate over pore pressure changes and impact the rock stress.

Perkins and Gonzales (1984) analyzed that thermal stress could generate secondary fractures in the formation, reduce the resistance to flow significantly, and increase the system efficiency. In detail, they mentioned that injecting cold water to the formation would form a region of low-temperature in the formation as shown in **Figure 7**. Stress within the region of changed temperature, as well as stress in the nearby area, will be altered due to the contraction of the rock matrix within the low-temperature region. The expansion of the rock later on during the heating will lead to reduced stress near the injection well. As a result, hydraulic fracturing pressure can be much lower.

In their following study of thermo-elastic stress, Perkins and Gonzales (1985) showed that the fracture initially is a bi-wing planar fracture, which propagates perpendicular to the direction of the minimum main horizontal stress. The fracture extends a further distance and the cold fluid region enlarges in shape with the larger cold water injection rate. This condition tends to reduce the stress in the cold fluid region. A flatter shape of cold fluid region occurs when the injection is continued. This causes the stresses across the fracture become larger than those parallel to the fracture. As a result, the fractures perpendicular to the principal bi-wing planar fracture would likely open as a secondary fracture and thus creating a complex fracture network.

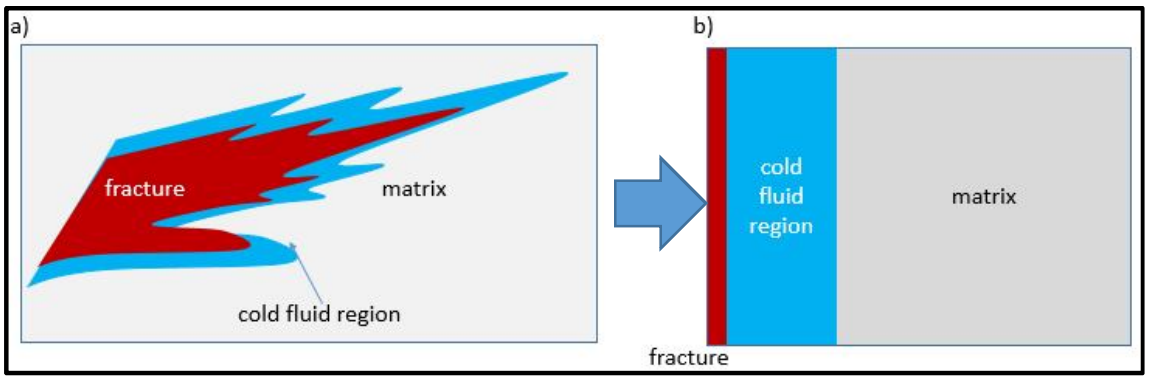

Fig. 7 – a) Diagram showing the invasion of the cold fresh slick water into the formation creates the cold fluid region near the fracture; b) One-dimensional representation used in numerical modeling of the invasion of the cold fresh slick water into the formation, which consists of fracture, cold fluid region, and matrix domain.

Various researchers have previously investigated the relationship between stress and strain in a fluid-filled porous medium under temperature alteration. The change of stress induced by pressure-temperature changes can be predicted in a same treatment when the porosity and permeability are assumed independent of stress level (Lubinski, 1954). Winterfeld and Wu (2016) have developed the geomechanical formula for the mean normal stress –a primary variable– and volumetric strain –a rock property– along with the associated fluid heat flow equation as followed.

$$\frac{3(1-v)}{1+v}\nabla^2\bar{\sigma} + \nabla F_b - \frac{2(1-2v)}{1+v}\sum_j \left[\alpha\nabla^2 P_j + 3\beta_t K\omega_j \Delta T\right] = 0 \qquad (2)$$

Here, $\bar{\sigma}$ is the mean normal stress, v is Poisson's ratio, α is Biot's coefficient, β_t is the coefficient of thermal expansion, K is the bulk modulus of elasticity, and F_b is the body force vector per unit volume. This formula can be used for multi-porosity non-isothermal. The subscript j refers to multi-porosity-continua of the formation. Each

temperature term is weighted by the porous continuum volume fraction (ω_j), if the temperature between the multi-porosity continua is vary. In addition to previous formula, they described porosity (ϕ) as a function of a volumetric strain (ε_{vol}) as followed:

$$\phi = \phi_{init} + \left(\varepsilon_{vol,init} - \varepsilon_{vol}\right) \quad (3)$$

where the subscript $init$ refers to initial conditions. Here, porosity could change dynamically following the alteration of volumetric strain, which is sensitive to temperature gradient and modeled as function of the mean normal stress:

$$\varepsilon_{vol} = \frac{3(1-2v)}{E}\left(\bar{\sigma} - \left[\alpha P_{A,I} + 3\beta_t K \omega \Delta T\right]\right) \quad (4)$$

Here, E is Young's modulus. As we can see from those formulae above, porosity will be affected by the changes in pressure and temperature. The mean normal stress also changes when temperature imbalance is high. Temperature imbalance develops when a cooler water is injected into hot formation during hydraulic fracturing. The heat transfer from hot formation into the cold fluid region during shut-in period reduces the mean normal stress. As the result, the confining pressure decreases and permeability of the formation induces.

Temperature also controls capillary pressure in a complex way. Capillary pressure is defined as the pressure difference between two immiscible fluids in contact and can be expressed using the Young-Laplace equation as follows Brook and Corey (1964):

$$P_c = \frac{2\sigma cos\theta}{r} \quad (5)$$

The above equation shows that capillary pressure in the reservoir is related to contact angle (θ), pore radius (r), and interfacial tension between the two immiscible fluids (σ). The interfacial tension decreases when temperature increases as proposed by Firoozabadi and Ramey (1988):

$$\sigma = \left[\frac{1.58(\rho_w - \rho_g) + 1.76}{T_r^{0.3125}}\right]^4 \quad (6)$$

where, ρ_w and ρ_g are water and gas density and T_r is the reduced temperature. Meanwhile, pore radius is proportional to the formation permeability according Carman-Kozemy equation (Carman, 1956):

$$k = \frac{\phi r^2}{8\tau} \quad (7)$$

where τ is tortuosity. Substituting equations (5) – (7) provides a capillary pressure formula as a function of temperature:

$$P_c = \left[\frac{1.58(\rho_w - \rho_g) + 1.76}{T_r^{0.3125}}\right]^4 \times \sqrt{\frac{\phi}{k}} \quad (8)$$

Based on equation above, capillary pressure is sensitive to temperature changes. Since porosity and permeability are temperature dependent, the changes in both properties due to the temperature alterations add the impact to capillary pressure directly.

2.3. Chemical Osmosis Effect

Osmosis phenomenon is one of the key processes to control the chemical transport, water flow, and deformation behavior of clays. The osmotic pressure forces low salinity water molecules in the fractures and cracks diffuse through the semi-permeable membrane clays into the shale matrix. The following section describes the impact of chemical process in the shale gas reservoirs.

2.3.1. Stress-Dependent Permeability due to Chemical Osmosis Effect

Osmosis is a diffusive transport mechanism for the fresh fracturing water molecules through a selective permeable material (usually composed of clays or clay-rich sediments), which acts as a semi-permeable membrane. An uncharged solvent (usually water) driven by the chemical potential difference tend to be transported from the region with low salt concentration to the region with high salt concentration pass through the clay membrane. On the other hand, the passage of solute molecules (salts) or ions (both cations and anions) are inhibited through the pore of the compacted clay membrane as shown in **Figure 8** (Marine and Fritz, 1981; Medved and Cherny, 2013).

The pore body and the surface of clay particle within shale formation have a net negative charge because of ion substitution. The negative charge attracts the cation to adsorb into clay surface and forms the electro double layer as a semipermeable barrier around the clays as shown in **Figure 9.** The semi-permeable membrane allows some water molecules in fresh water to flow through it thus causing osmotic water transport. The semi-permeable membrane restricts the flow of some salt ions in the clay pores. The membrane should have some characteristics, such as water-wetness, and be capable of achieving acceptable capillary pressure. Liu et al. (2015) argued that the ideal membrane should be impermeable to all the salts, freely permeable to water.

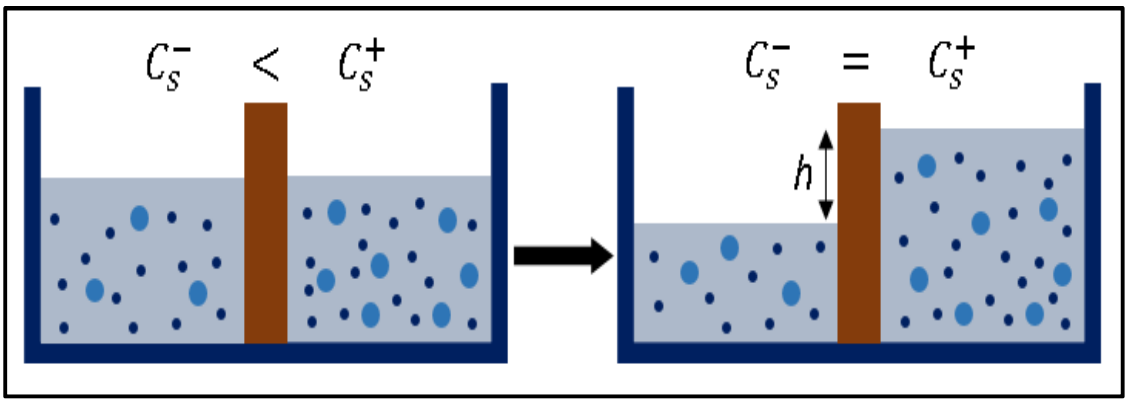

Fig. 8 – Illustration of chemical osmosis. A porous material, which acting as semipermeable membrane allows the passage of the solvent (water) but not the solute (adopted from Medved and Cerny, 2013).

The ability of material to act as an osmotic membrane is quantitatively indicated by the osmotic efficiency, also known as the reflection coefficient (σ). Its value ranges from 0 for a non- permeable selective material and 1 for a material with ideal membrane behavior.

The fluid transport caused by osmosis not only occurs because of the concentration difference (chemo-osmosis), but also the gradient of electrical potential in the material can force the fluid to flow pass through the membrane (electro-osmosis) (Casagrande, 1949). Additionally, the difference in temperature also can lead the fluid to transport from hot to cold region and vice versa (thermo-osmosis) controlled by the difference of the fluids enthalpy between the fluids in the clay pore and the pore water affected by the clay interactions (Goncalves and Tremosa, 2010). The contribution of chemical and thermal effects in shales are often several times bigger than the hydraulic fluid transport due to a very low permeability (order of nano-darcy) (Ghassemi and Diek, 2001). A significant mass transport through clay membrane due to a temperature and concentration gradient has been investigated in laboratory (Dirksen, 1969; Marine and Fritz, 1981; Medved and Cherny, 2013).

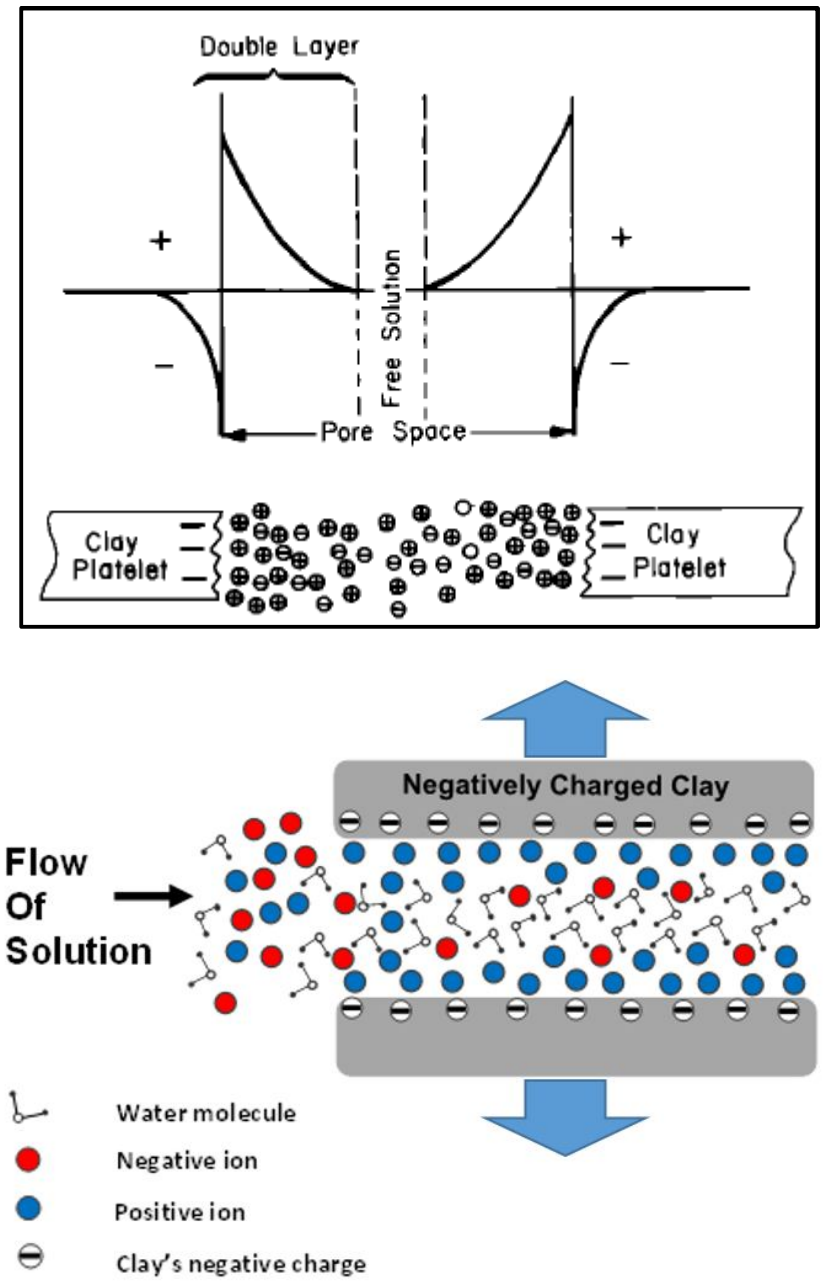

Fig. 9 – Illustration of double layer in a clay pore that act as a semi-permeable membrane because the negative charge in clay surface allows cation and reflects anion. (Reprinted from Marine and Fritz, 1981; Eveline and Akkutlu, 2017).

In the shale system, the osmosis occurs when the fracturing fluids solution with different salt concentration from solution inside the clay make a contact. The osmosis reduces the fluid pressure in the region with low salt concentration and increases the pressure inside the clay with high salt concentration. The two pressures will counter each other until the equilibrium is reached and cause clay swelling as illustrated in **Figure 9.** The swelling pressure is accumulated from the van der Waals attraction, the electrostatic Born repulsions, and short-range repulsive and attractive forces that are derived from hydration/solvation of clay surface and the adsorbed or free ions within interlayer spacing (van Oort, 2003). On the shale system, clay swelling pressure is considered as additional confining stress which affect crack permeability change (Eveline and Akkutlu, 2017).

The swelling of clay occurs when the layer structure of the clay minerals and the cations adsorbed for the charged reach equilibrium. The clay swelling behavior can change by cation exchange. There are two categories of swelling, which are the inner-crystalline swelling and osmotic swelling (Madsen and Müller-Vonmoos, 1989).

The first category, the inner-crystalline swelling appears because of the hydration of the exchangeable cations of the dry clay. In this state, the exchangeable interlayer cations lie so close together as shown in **Figure 10**. The contact with the water cause the cations adsorb the water and place themselves on a plane halfway between the clay layers. As a results, the swelling occurs due to the spacing between the layers become wider.

The second category, osmotic swelling happens because of the large difference in the ion concentration, especially in the cation concentration, close to the clay surface and in the pore water. Inside the formation, the repulsive forces between the overlapping double layer of the clay particles and the overburden pressure are at equilibrium. When the water is available, the water disturb the equilibrium by intruding between the clay layers and pushing them apart as shown in **Figure 11**. The swelling continues until the new balance between resisting forces is reached.

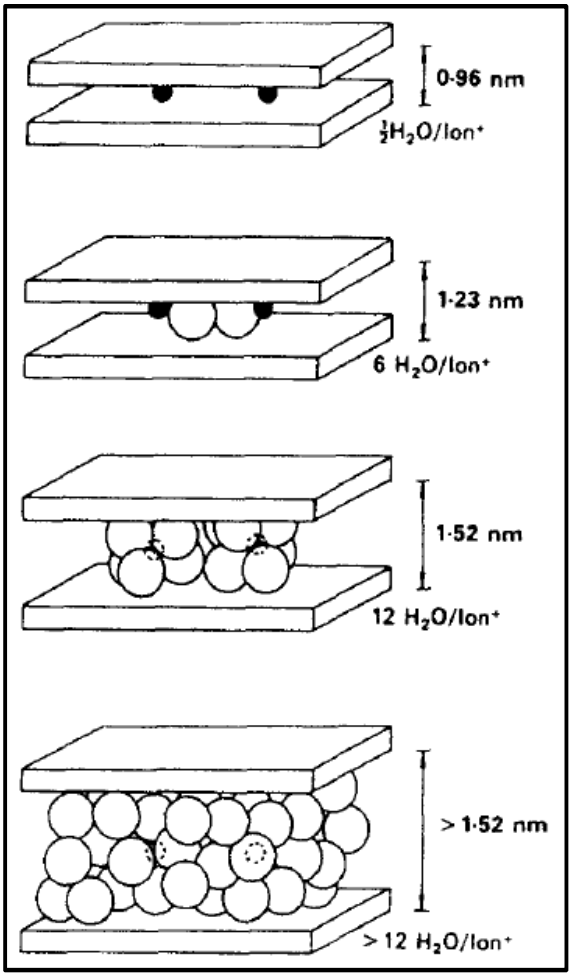

Fig. 10 – Inner-crystalline swelling of sodium montmorillonite. Reprinted from Madsen and Müller-Vonmoos (1989).

When the formation has contacted with the formation fluids, reservoir property changes in the shale matrix region near to the hydraulic fracture because the fracturing water imbibition into the shale matrix. This region is called the altered zone. Osmosis induces formation damage in the altered zone by decreasing micro-crack or micro-crack permeability due to swelling pressure build up inside clay pore.

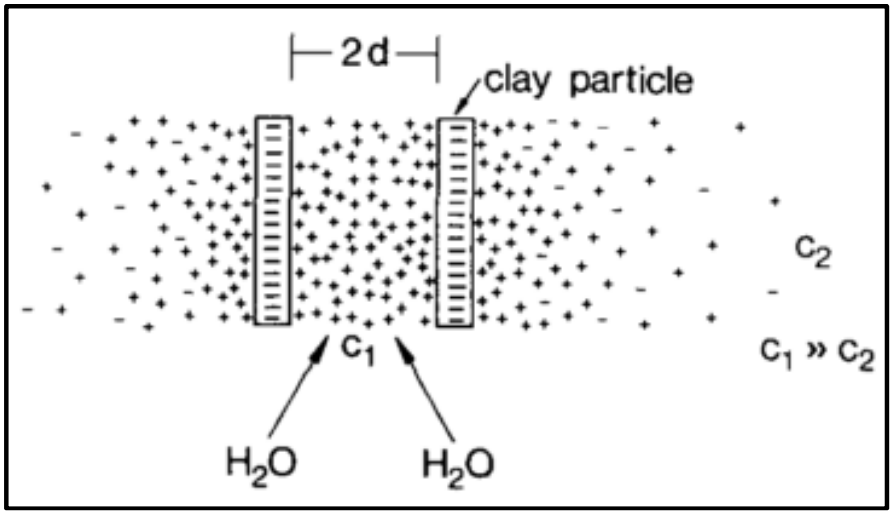

Fig. 11 – Two negatively charged clay layers with the ion concentration C_1 between the layers much higher than the ion concentration C_2 in the water surrounding the clay particle. An equilibration can only be reached by water penetrate into the clay interlayer space, since the interlayer cations are fixed electrostatically by the negative charge of the layers (osmotic swelling). Reprinted from Madsen and Müller-Vonmoos (1989).

The permeability can be reduced significantly with the use of fresh water even with the use of brine with low salinity as the fracturing fluids, when the formation fluid in the clay pores has high salinity or when the shale matrix has a sub-irreducible water saturation level. In the previous section, I already discussed that permeability is a function of effective stress, $(P_{conf} - \alpha P)$. The swelling pressure inside the clay pores gives additional stress to the micro-crack pressure. As a result, the confining pressure increases and induces the permeability reduction in the micro-cracks. On their study, Eveline et al. (2017) showed that the high swelling pressure in the clay pores is a function of the salt type, the clay membrane efficiency, and the salt concentration difference.

2.3.2. Chemical Contribution on Chemo-Thermo-Poro-Elastic System

Following the invasion of the hydraulic fracturing fluid into the formation, the fracturing fluid contacts with the clays in the shales formation, there will be a chemical potential imbalance between the invaded water and the clay pores water. The brine salinity of the shale reservoir could reach up to 300000 ppm (Haluszczak et al., 2013) while the salinity of slick water is generally in the range of 1000 ppm (Fakcharoenphol et al., 2016; Wang et al., 2017). This imbalance allows the migration of invasion water molecules which have low salt concentration water into the clay pores between aggregates, particles, and basal planes of crystal, which contain high salt concentration water. This mechanism is known as osmosis. Here, the negative charges on clay particles surface act as a semi permeable membrane and restrict the dissolved salt ions to pass through the clay surface. Only water is transported.

Swelling is a mechanical deformation of the clays in the tight gas and shale formations due to diffusion of the fluid molecules in the interlayer clay pores. These clay pores were initially filled fully or partially with saline formation water. Since clays are semi-permeable membranes, the dissolved ions in the saline water may not efficiently diffuse out of the pores but the fresh fracturing treatment water molecules are allowed to diffuse in. Osmosis leads to pressure build up and clay swelling in clay pores. The clay swelling pressure enlarges the effective stress by adding confining pressure with the increased pressure inside the clay pores. This changes add the micro-cracks permeability reduction.

By following Eveline et al. (2017) approach, the mass exchanges of component κ between the clay pores and the silt-shaped pores, which are driven by hydraulic pressure and chemical potential gradient, are added into mass balance equation, which will be discussed in the following chapter as a coupling term. The mass exchanges cause pressure build up inside the clay pores or clay swelling pressure, which affects confining pressure on Equation (1). Mass exchange functions of component H_2O and CH_4 are defined as:

$$w_A^{\kappa} = l_{IC}\left\{x_A^{\kappa}\frac{k_m\rho_A}{\mu_A}\left(P_{A,I}-P_{A,Clay}\right) - \nu RT x_A^{\kappa}\rho_A\frac{\sigma k_m}{\mu_A M_w^{salt}}\left(x_{A,I}^{salt}-x_{A,Clay}^{salt}\right) + \phi_{Clay}S_A\tau_A\rho_A D_A^{\kappa}\left(x_{A,I}^{\kappa}-x_{A,Clay}^{\kappa}\right)\right\} \quad (9)$$

Here, l_{IC} is the shape factor, k_m is the permeability of porous medium acting as semi permeable membrane, R is gas constant, M_w^{salt} is the molecular weight of salt, and ν is the dissociation coefficient of salt. The subscript I and $Clay$ refer to inorganic micro-crack and clay pores. Mass exchange function of component salt is defined in the following equation:

$$w_A^{salt} = (1-\sigma)l_{IC}\left\{x_A^{salt}\frac{k_m\rho_A}{\mu_A}\left(P_{A,I}-P_{A,Clay}\right) - \nu RT x_A^{salt}\rho_A\frac{\sigma k_m}{\mu_A M_w^{salt}}\left(x_{A,I}^{salt}-x_{A,Clay}^{salt}\right) + \phi_{Clay}S_A\tau_A\rho_A D_A^{salt}\left(x_{A,I}^{salt}-x_{A,Clay}^{salt}\right)\right\} \quad (10)$$

This function depends on the membrane efficiency (σ), which ranges from 0 as no solute restriction to 1 as an ideal membrane. The membrane efficiency is affected by several factors such as the composition and stress of the material and the type and concentration of the solute in the pore water, In general, the membrane efficiency reduces with the solute concentration and increases with the effective stress. The following equation can be used for calculating the membrane coefficient (Marine and Fritz, 1981):

$$\sigma = 1 - \frac{\left(\frac{C_a}{C_s}\right)(R_{ca-w}+1)}{\left\{\left[R_{ca-w}\left(\frac{C_a}{C_c}\right)+1\right] + R_{a-mw}\left[R_{ca-m}\left(\frac{C_a}{C_c}\right)+1\right]\right\}\phi_c} \quad (11)$$

where C_s is the arithmetic mean solute concentration of the solution pair and C_a and C_c are anion and cation concentrations within membrane pores, which can be calculated as a function of the cation exchange capacity (C_{EC}) by the following equation (Hanshaw, 1962; Fritz, 1986):

$$C_a = -\frac{1}{2}C_{EC}\rho_{Clay}\left(1-\phi_{Clay}\right) + \frac{1}{2}\left[\left(C_{EC}\rho_{Clay}\left(1-\phi_{Clay}\right)\right)^2 + 4C_s^2\phi_{Clay}^2\right]^{1/2} \quad (12)$$

$$C_c = C_a + C_{EC}\rho_{Clay}\left(1-\phi_{Clay}\right) \quad (13)$$

2.4. Capillary End Effect (CEE)*

The impact of CEE on the formation damage during the flow-back and production periods are investigated using theoretical description and numerical modeling. CEE phenomenon has been considered previously in several studies. This section will discuss the influence of CEE during relative permeability measurements and core flooding experiment. Moreover, the approach to correct the measurement data due to CEE will also be explained here.

* Part of this chapter is reprinted with permission: "Near Fracture Capillary End Effect on Shale Gas and Water Production" by Elputranto, R., & Akkutlu, I. Y., 2017. In *Unconventional Resources Technology Conference, Houston, Texas, 23-25 July 2018* (pp. 756-769). Society of Exploration Geophysicists, American Association of Petroleum Geologists, Society of Petroleum Engineers., whose permission is required for further use.

2.4.1. Capillary End Effect during the Relative Permeability Measurements

Relative permeability is a fundamental quantity in reservoir engineering. Relative permeability is measured using the relative permeability vs saturation data which is obtained from flow experiment with cores in the laboratory. In general, there are two methods to derive the displacement data. First method is by injecting both of the immiscible fluids into the core simultaneously or as known as steady states flow experiment. The total flow-rate of both of the immiscible fluids is usually kept constant while their ratio is change at the exit of the core. The second one is unsteady state flow experiment in which one of the fluids displaces the other.

The advantages of the steady state experiment is allowing data collection over the whole saturation range. These results are easy to interpret. However, this method also has some drawbacks. It is very difficult to achieve a constant average saturation of the fluids using this method and this experiment also need longer time to provide the saturation after each change because the pressure drop and the effluent flow ratio in the core need to reach equilibrium before collecting data. On the contrary, the unsteady state experiment can be conducted relatively faster but will give more complex results which make the data interpretation more complicated (Civan and Donaldson, 1989).

In both cases, the capillary forces in the displacement process is assumed negligible. On the other hand, the capillary pressure is related to saturation and saturation history of the rock. Some errors can be found during the experiment because capillary forces trigger the boundary effect when the relative permeability measurement is conducted at low flow rates (Richardson et al., 1952; Virnovsky et al., 1995). This means that the rates much higher than reservoir flow rate has to be used during displacement experiment. The higher rates lead to flow instability and fines migration. (Gabriel and Inamdar, 1983; Archer and Wang, 1973).

At lower rates, on the other hand, the capillary discontinuity (end effect or boundary effect) develops at the outlet end of the sample where the fluids pass through the core sample during laboratory measurement. The discontinuity accumulate the wetting

phase at the sample end which affect saturation distribution and pressure drop across the length of the sample (Gupta and Maloney, 2016). The saturation distribution along the core become non-uniform and the pressure drop is different in each phase.

A recent study during the relative permeability measurement of Eagle Ford shale samples mentions CEE occurrence in low permeability unconventional rocks with much smaller capillaries and cracks. The high capillary pressure causes a significant liquid hold-up and leads to CEE at the outlet during the flow measurement, thus leads to incorrect relative permeability estimation (Moghaddam and Jamiolahmady, 2019).

CEE could be extremely significant in small scale laboratory experiment (Leverett, 1941). However, the importance of CEE decreases as the fluids viscosities, the length of the core, or the rate on injection are increased (Kyte and Rapoport, 1958). CEE can take place in the single segment of composite core (Hinkley and Davis, 1986). The steady-state technique is considered to have less impact of CEE (Braun and Blackwell, 1981).

2.4.2. Capillary End Effect in the Laboratory and in the Field

CEE has long been recognized as an important phenomenon in the laboratory during the drainage process at the effluent end of the core samples (Leverett, 1941; Huang and Honarpour, 1998; Liang et al., 2017), and in the field during production from naturally fractured oil reservoirs at the circumferences of the wells (Bear, 1988; Christiansen, 2005). In 1956, Hadley and Handy doing a core flooding experiment to prove the existence of capillary end effect. They put a sample core that has been saturated with oil and water into core plug as shown in **Figure 12.** They conduct a drainage process by injecting the core plug with oil, so the oil will displace the water to outer boundary. When, the fluid reach the outer boundary, there is flow from core with high capillary pressure into empty space with no capillary pressure, which makes a capillary discontinuity happened (Hadley and Handy, 1956).

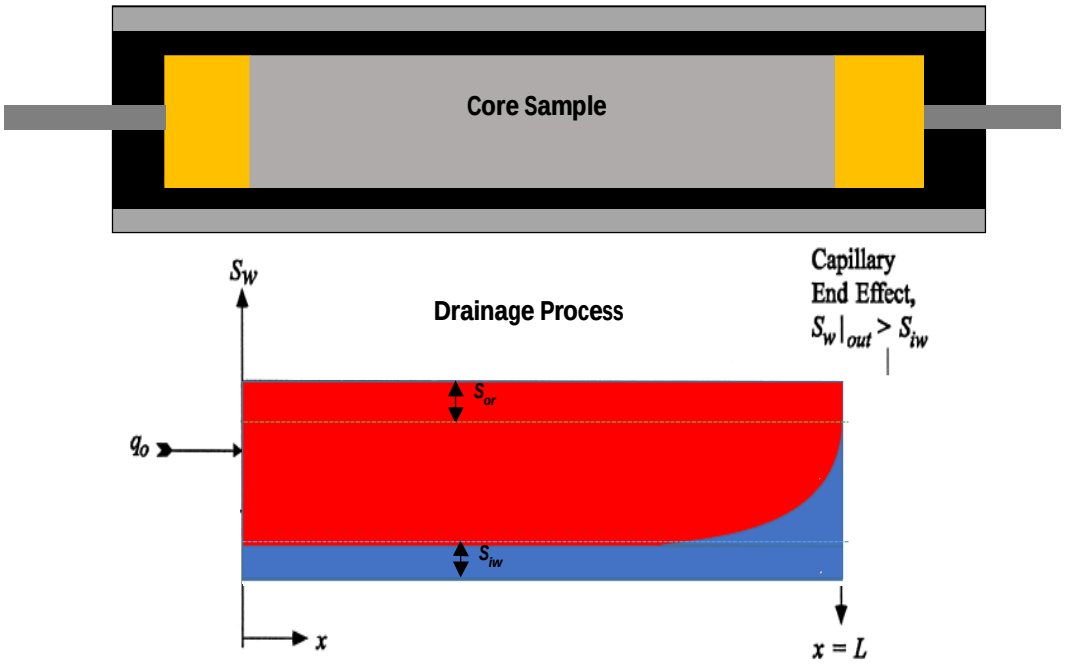

Fig. 12 – Schematic diagrams of Hadley and Handy experiment. Capillary end effect occurred during drainage process of oil flooding.

At the fracture-matrix interface, the flowing fluids leave the tight formation in the presence of high capillary pressure and enter the fracture with negligible capillary pressure. As the consequence of this capillary discontinuity, a non-uniform interstitial water saturation distribution develops along the formation as a boundary layer of rapid transitions in capillary pressure and water saturation in the shale formation near the fracture, **Figure 13**. Capillary discontinuity also could develops when the local capillary pressure increases rapidly after snap-off events during water invasion in water-wet permeable media. The snap-off event is the situation when the water in pore throat swells until it is in a pressure non-equilibrium state. The capillary pressure drops rather abruptly and it becomes more difficult for the water to leave the boundary. This leads to build up of the water saturation locally. Consequently, it becomes more difficult for the gas to displace the water and reach into the fracture (Hadley and Handy, 1956).

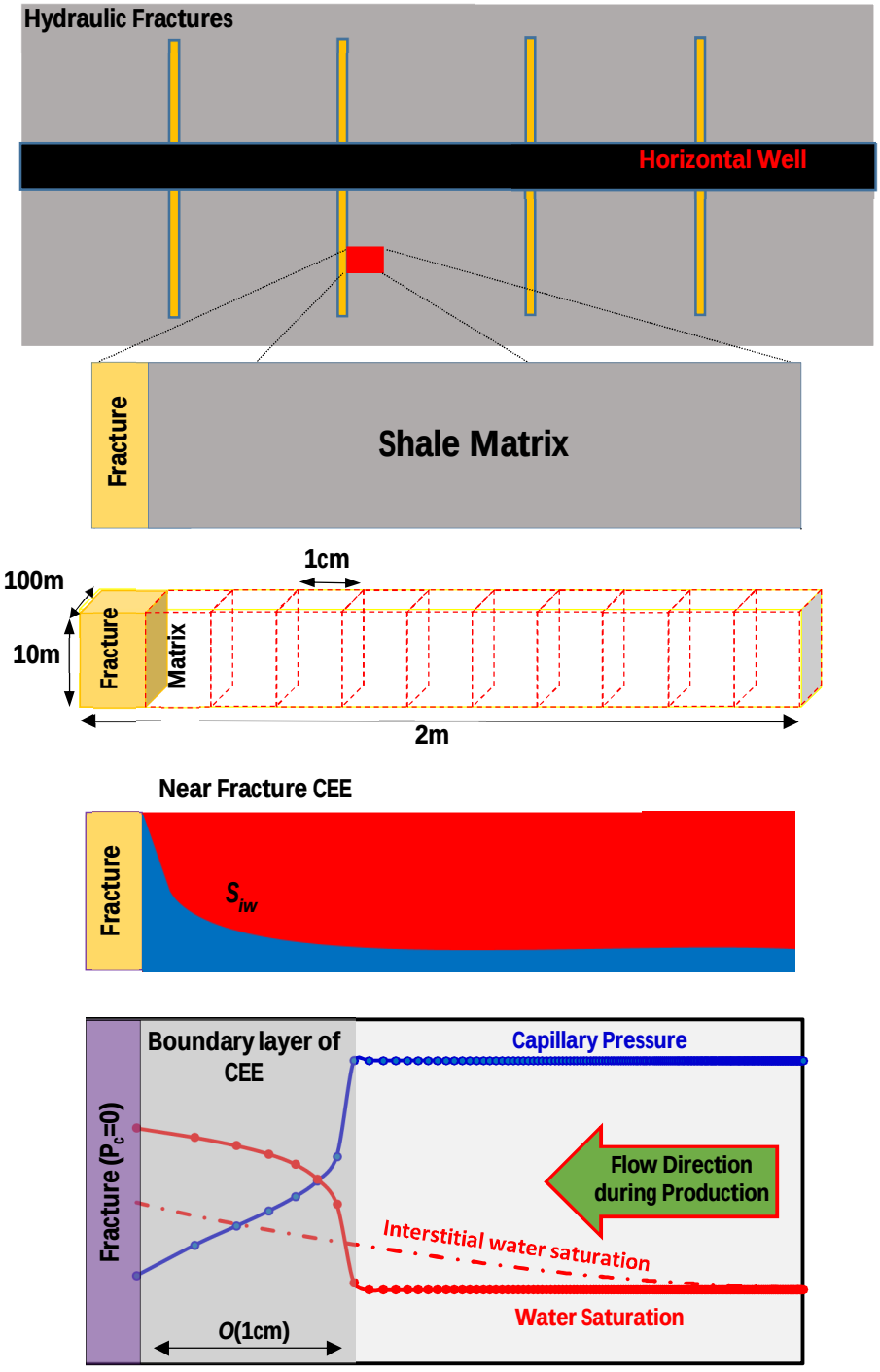

Fig. 13 – Diagram showing the capillary end effect (CEE) in tight gas and shale formation near the fracture during gas flow and production.

CEE causes accumulation in the water phase and an excessive water saturation in the boundary (Osoba et al., 1951; Richardson, 1952). At the leading edge of the boundary, on the right, the capillary forces could be still high enough and exceed the drawdown pressure. Consequently water may continue to imbibe into the formation during the gas production. Based on this discussion it is anticipated that the two-phase flow dynamics of water and gas varies significantly near the fracture.

CEE develops in the fractured tight formations during the flow back period while the natural gas displaces the fracturing water. In this study, CEE in a shale formation is modeled by considering a segment of reservoir near a hydraulic fracture perpendicular to the horizontal well as shown in **Figure 13**. This segment problem includes the shale matrix as the domain of two-phase flow and the fracture as the boundary of a semi-infinite flow system.

2.4.3. Capillary End Effect Models in the Literature

During the modeling and simulation of the two-phase flow in the presence of CEE, the main technical problem is in determining the formation interstitial water saturation build-up as a function of the distance to the hydraulic fracture. The distance significantly influences the saturation levels attained in the boundary layer and the associated end-point relative permeability. Several approaches have previously been proposed to correct the relative permeability and capillary pressure under steady-state (Hadley and Handy 1956; Virnovsky et al., 1995; Huang and Honarpour, 1998) and unsteady-state (Ashrafi and Helalizadeh, 2014) conditions. This section presents a brief review of each approach.

Ashrafi and Helalizadeh (2014) included the capillary end effect into the calculation of saturation and relative permeability during unsteady state displacement by modifying the outlet boundary condition into three distinct stages of water flood. The first stage includes only oil is produced and the water saturation at $x = L$ is kept at the irreducible level ($S_w = S_{iw}$). In the second stage, water saturation at $x = L$ increases from S_{iw} to $1 - S_{or}$ with only oil is still produced. In the last stage, the water saturation at $x =$

L keep fixed at the $1 - S_{or}$, but now all the fluids (water and oil) are produced. The continuity equation, which they used to simulate the displacement can be described as follows:

$$\frac{\partial S_w}{\partial T} + \frac{df_w}{dS_w}\frac{\partial S_w}{\partial X} + \frac{1}{L\mu_o u_t}\frac{\partial}{\partial X}\left(k_{ro}(S_w) f_w \frac{dP_c(S_w)}{dS_w}\frac{\partial S_w}{\partial X}\right) = 0 \qquad (14)$$

where x is the distance along core, L is the length of system, k_{ro} is relative permeability of oil, μ_o is oil viscosity, and u_t is a total fluid velocity. The dimensionless parameters are obtained with the following relations:

$$X = \frac{x}{L} \qquad (15)$$

$$T = \frac{u_t t}{L\phi} \qquad (16)$$

Hadley and Handy (1956) determined the steady-state saturation profile and pressure profile as a function of the distance from the outlet end of the system by introducing two dimensionless numbers (N_{RL} and N_{REK}) into one dimensional system with incompressible flow and displacement. N_{RL} or the Rapoport-Leas number is an essential measure of the ratio of the capillary forces to the viscous forces in the system. Meanwhile, N_{REK} or the relative Engelbeard-Klinkenberg number is a measure of the ratio of gravitational forces to the viscous forces in the system. These two dimensional numbers can be defined as follows:

$$N_{RL} = \frac{k\check{p}}{\mu_o L q} \quad (17)$$

$$N_{REK} = \frac{k(\rho_w - \rho_o) g \sin\theta}{\mu_o q} \quad (18)$$

In the equation above, the authors define $\check{p}$ as the most characteristic capillary pressure in the system or the pressure in a simple capillary tube model where the slope of the capillary pressure is a minimum. Then, the dimensionless distance or X (as equal to Equation (15)) is calculated as a function of saturation and $\check{p}$ can be found as a function of X as the following:

$$1 - X = -N_{RL} \int_{S_{wr}}^{S} \frac{\beta dS}{\mathcal{F}_w - \alpha} \quad (19)$$

and the oil pressure as a function of saturation is calculated as follows:

$$\Delta p_o = \int_{S_{wr}}^{S} \frac{\left((1 - \mathcal{F}_w) + k_{ro} N_{EK}^{o}\right) \beta dS}{(\alpha - \mathcal{F}_w)} \quad (20)$$

where p_o is oil pressure, S_{wr} is residual water saturation, and the other parameters are defined as follows:

$$\mathcal{F}_w = \alpha + N_{RL} \beta \frac{\partial S}{\partial X} \quad (21)$$

$$N_{EK}^{o} = \frac{k\rho_o g \sin\theta}{\mu_o q} \quad (22)$$

$$\alpha = F_w(1 - N_{REK}k_{ro}) \quad (23)$$

$$\beta = F_w k_{ro}\frac{dP_c}{ds} \quad (24)$$

$$F_w = 1 + \left[\frac{k_{ro}\mu_w}{k_{rw}\mu_o}\right]^{-1} \quad (25)$$

Another approach to include CEE during the relative permeability measurements at a steady state procedure is given by Virnovsky et al. (1995). The derivatives is used in analytical corrections to calculate saturation and relative permeability at the inlet from average values and change in values with change in total flow rate. Their technique considers the saturation at inlet is independent of the pressure. The saturation only depend on measured volume as the following equations:

$$k_{ri}(S^0) = \tilde{k}_{ri}\left[1 - \frac{u_t}{\tilde{k}_{ri}}\frac{d\tilde{k}_{ri}}{du_t}\right]^{-1} \quad (26)$$

where the correction to the saturation can be written as follows:

$$S^0 = \frac{d(\bar{S}u_t)}{du_t} = \bar{S} + u_t \frac{d\bar{S}}{du_t} \quad (27)$$

In the equations above, S^0 is saturation at the core, and $\bar{S}$ is the average saturation.

The last approach for CEE correction during steady state measurement or relative permeability is by Huang and Honarpour (1998). Their approach has been used by several studies of CEE (Romanenko and Balcom, 2013; Moghaddam and Jamiolahmady, 2018). Here in this study we perform the investigation using the approach proposed by Huang and Honarpour (1998) to introduce CEE into a two-phase flow simulator and quantify the its impact on the water flow back and gas production during the first few months of production. The detail explanation about the approach of saturation profile correction by Huang and Honarpour (1998) is discussed in the following section.

2.4.4. Huang and Honarpour Method

Huang and Honarpour (1998) derived a formula to distribute the non-uniform saturation profile at the steady-state based on Darcy's law. For gas-water system, the derivation can be described as follows:

$$\frac{q_w}{A} = -\frac{kk_{rw}}{\mu_w}\frac{\partial p_w}{\partial x} \quad (28)$$

$$\frac{\partial P_c}{\partial x} = \frac{dP_c}{dS_w}\frac{\partial S_w}{\partial x} \quad (29)$$

$$P_c = p_g - p_w \quad (30)$$

In equations above, q_w is water flow rate, A is surface area, x is a distance from the inlet, k is absolute permeability, k_{rw} is relative permeability of water, p_w and p_g is water and gas pressure, μ_w is water viscosity, S_w is water saturation, and P_c is capillary pressure. Combining Equations (28) – (30) obtain:

$$\frac{\partial P_c}{\partial x} = \frac{1}{kA}\left(\frac{q_w \mu_w}{k_{rw}} - \frac{q_g \mu_g}{k_{rg}}\right) \quad (31)$$

where q_g is gas flow rate, μ_g is gas viscosity, and k_{rg} is relative permeability of gas. The capillary pressure is only a function of water saturation. Substituting with Equation (31) gives:

$$\frac{\partial P_c}{\partial x} = \frac{dP_c}{dS_w}\frac{\partial S_w}{\partial x} \quad (32)$$

$$\frac{\partial S_w}{\partial x} = \frac{1}{kA}\left(\frac{q_w \mu_w}{k_{rw}} - \frac{q_g \mu_g}{k_{rg}}\right) \Big/ \frac{dP_c}{dS_w} \quad (33)$$

Since water saturation is not a function of time during steady-state, the integration of Equation (33) can be used to predict the saturation profile as a function of distance. In the presence of gas residual, it can be written as:

$$\int_x^L dx = kA \int_{S_w}^{1-S_{gr}} \left[\frac{dP_c}{dS_w} \Big/ \left(\frac{q_w \mu_w}{k_{rw}} - \frac{q_g \mu_g}{k_{rg}}\right)\right] dS_w \quad (34)$$

Here, S_{gr} is the residual gas saturation and L is the total length of the core. The capillary pressure and fluids relative permeability on Equation (34) can be represented by Brooks and Corey (1964) as follow:

$$P_c = P_d \left(\frac{S_w - S_{iw}}{1 - S_{iw} - S_{gr}} \right)^{\frac{-1}{\lambda}} = P_d (S_w^*)^{-\frac{-1}{\lambda}} \quad (35)$$

$$k_{rg} = k_{rg}\big|_{S_{iw}} (1 - S_w^*)^2 \left[1 - (S_w^*)^{\frac{2}{\lambda}+1} \right] \quad (36)$$

$$k_{rw} = k_{rw}|_{S_{gr}} (S_w^*)^{\frac{2}{\lambda}+3} \quad (37)$$

Here, P_d is the displacement pressure or known as threshold pressure, S_{iw} is interstitial water saturation, $S_w^*$is the normalized water saturation based on the mobile saturation range of $1 - S_{iw} - S_{gr}$ and λ is a core-dependent constant for P_c as known as Corey's exponent. The subscript represents the parameter value measured at the certain saturation point. Combining Equations (34) – (37), the profile equation becomes:

$$\frac{L - x}{L} = \psi \int_{S_w^*}^{1} \left[\frac{1}{\lambda} \frac{(S_w^*)^{\frac{-1}{\lambda}-1} \left[(S_w^*)^{\frac{2}{\lambda}+3} \right] \left[(1 - S_w^*)^2 \left[1 - (S_w^*)^{\frac{2}{\lambda}+1} \right] \right]}{\left[(S_w^*)^{\frac{2}{\lambda}+3} \right] - \frac{q_w \mu_w k_{rg}\big|_{S_{iw}}}{q_g \mu_g k_{rw}|_{S_{gr}}} \left[(1 - S_w^*)^2 \left[1 - (S_w^*)^{\frac{2}{\lambda}+1} \right] \right]} \right] dS_w^* \quad (38)$$

where

$$\psi = \frac{kk_{rg}\big|_{S_{iw}} AP_d}{Lq_g\mu_g} \qquad (39)$$

Consider single-phase gas injection, where no water co-injection, the normalized inlet-end water saturation ($S^*_{w,inlet}$) is generated where $x = 0$ as follows:

$$1 = \psi\frac{1}{\lambda}\int_{S^*_{w,inlet}}^{1}\left[\frac{(1-S^*_w)^2\left[1-(S^*_w)^{\frac{2}{\lambda}+1}\right]}{(S^*_w)^{\frac{1}{\lambda}+1}}\right]dS^*_w \qquad (40)$$

Integrating term by term Equation (40) gives following equation:

$$\begin{aligned}1 = \psi\Bigg[&\left(S^*_{w,inlet}\right)^{-\frac{1}{\lambda}} - \frac{2\lambda^2(\lambda+2)(6\lambda^2+\lambda+1)}{(\lambda^2-1)(4\lambda^2-1)(3\lambda+1)} + \frac{2}{\lambda-1}\left(S^*_{w,inlet}\right)^{1-\frac{1}{\lambda}} \\ &- \frac{1}{2\lambda-1}(S^*_w)^{2-\frac{1}{\lambda}} + \frac{1}{\lambda-1}\left(S^*_{w,inlet}\right)^{1+\frac{1}{\lambda}} \\ &- \frac{2}{2\lambda+1}\left(S^*_{w,inlet}\right)^{2+\frac{1}{\lambda}} + \frac{1}{3\lambda-1}\left(S^*_{w,inlet}\right)^{3+\frac{1}{\lambda}}\Bigg]\end{aligned} \qquad (41)$$

The average water saturation over the whole core ($\bar{S}^*_{iw}$) after combine with Equations (34) – (40) can be written as follows:

$$\bar{S}_{iw}^{*} = \frac{1}{L}\int_{0}^{L} S_w^{*}\, dx = \frac{\psi}{\lambda}\int_{S_{w,inlet}^{*}}^{1}\left[\frac{(1-S_w^{*})^2\left[1-(S_w^{*})^{\frac{2}{\lambda}+1}\right]}{(S_w^{*})^{\frac{1}{\lambda}}}\right] dS_w^{*} \qquad (42)$$

Integrating term by term Equation (42) gives:

$$\begin{aligned}\bar{S}_{iw}^{*} = \psi\Bigg[&\frac{2\lambda^2(\lambda+2)(18\lambda^2+\lambda+1)}{(9\lambda^2-1)(4\lambda^2-1)(4\lambda+1)(\lambda-1)} - \frac{1}{\lambda-1}\left(S_{w,inlet}^{*}\right)^{1-\frac{1}{\lambda}} \\ &+ \frac{2}{2\lambda-1}(S_w^{*})^{2-\frac{1}{\lambda}} - \frac{1}{3\lambda-1}(S_w^{*})^{3-\frac{1}{\lambda}} \\ &+ \frac{1}{2\lambda+1}\left(S_{w,inlet}^{*}\right)^{2+\frac{1}{\lambda}} - \frac{2}{3\lambda-1}\left(S_{w,inlet}^{*}\right)^{3+\frac{1}{\lambda}} \\ &+ \frac{1}{4\lambda+1}\left(S_{w,inlet}^{*}\right)^{4+\frac{1}{\lambda}}\Bigg]\end{aligned} \qquad (43)$$

The pressure drop within the core can be obtained by integrating the Darcy's law because of steady state and no water injection as follows:

$$\begin{aligned}\Delta P|_x &= -\frac{q_g\mu_g}{Ak}\int_0^x \frac{1}{k_{rg}}dx \\ &= -\frac{q_g\mu_g}{Ak}\int_0^x \frac{1}{k_{rg}}\frac{dx}{dS_w^{*}}\frac{dS_w^{*}}{dP_c}dP_c \\ &= \frac{q_g\mu_g}{Ak}\int_{P_c(S_{w,inlet}^{*})}^{P_c(S_w^{*})}\frac{1}{k_{rg}}\frac{Akk_{rg}}{q_g\mu_g}dP_c \\ &= \int_{P_c(S_{w,inlet}^{*})}^{xP_c(S_w^{*})} dP_c \\ &= P_d\left[(S_w^{*})^{-\frac{1}{\lambda}} - \left(S_{w,inlet}^{*}\right)^{-\frac{1}{\lambda}}\right]\end{aligned} \qquad (44)$$

The average relative permeability (based on the entire core pressure drop), $\bar{k}_{rg}\big|_{\bar{S}_{iw}}$ from Darcy's law is calculated using Equation (43) gives:

$$\bar{k}_{rg}\big|_{\bar{S}_{iw}} = \frac{Lq_g\mu_g}{(-\Delta P_L)Ak} = \frac{Lq_g\mu_g}{P_dAk}\left[\left(S^*_{w,inlet}\right)^{-\frac{1}{\lambda}} - 1\right]^{-1} \quad (45)$$

$$\frac{k_{rg}\big|_{S_{iw}}}{\bar{k}_{rg}\big|_{\bar{S}_{iw}}} = \psi\left[\left(S^*_{w,inlet}\right)^{-\frac{1}{\lambda}} - 1\right] \quad (46)$$

The normalized average interstitial water saturation, Equation (43) and ratio of the actual terminal gas relative permeability to the averaged terminal gas relative permeability $\left(\frac{k_{rg}\big|_{S_{iw}}}{\bar{k}_{rg}\big|_{\bar{S}_{iw}}}\right)$ as a function of the ratio of the displacement pressure to the viscous pressure drop over the entire core (ΔP_L), Equation (46) can be generated using the solution as shown in **Figure 14** and **Figure 15.**

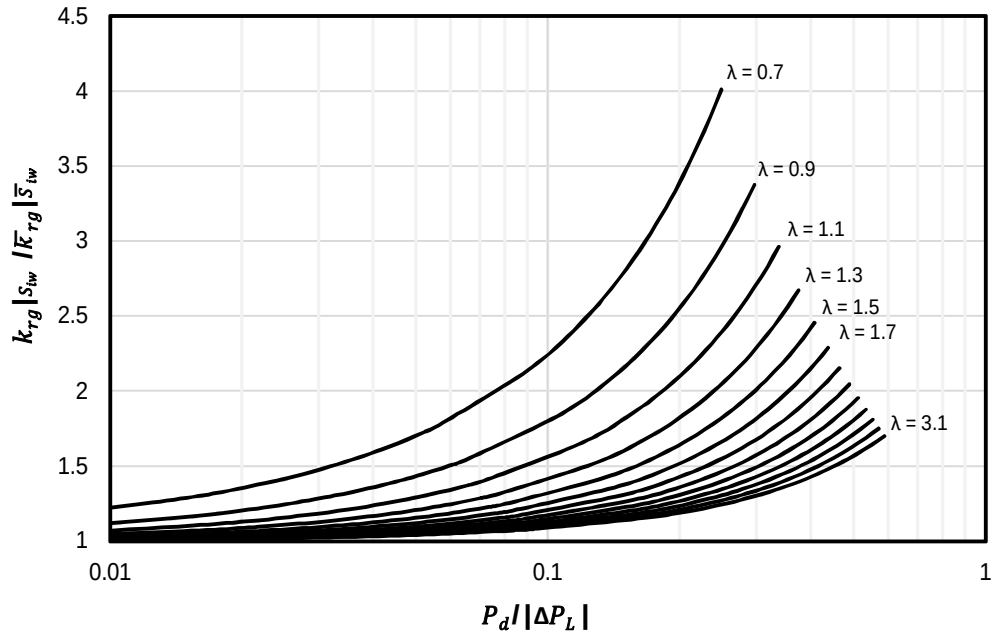

Fig. 14 – The correlation curves for correcting terminal relative permeability used in Huang and Honarpour (1998) approach.

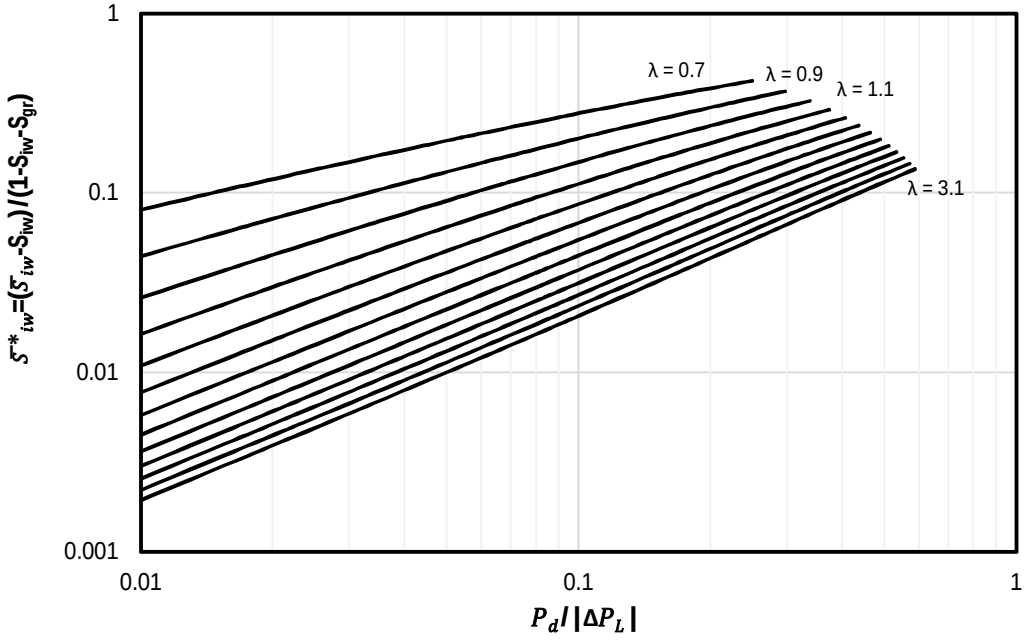

Fig. 15 – The correlation curves for correcting interstitial water saturation used in Huang and Honarpour (1998) approach.

3. MATHEMATICAL FORMULATION AND NUMERICAL MODEL DEVELOPMENT

This chapter discusses the mathematical formulation and numerical model for simulation development. The numerical simulation used for the two-phase (aqueous and gaseous) flow study is introduced briefly. I developed the model as an extension of TAMU-FTsim, the flow and transport simulator developed at the Lawrence Berkeley National Laboratory, which is based on the TOUGH+ code (Moridis et al., 2014). This simulator has been designed to provide the built-in capability for solving the traditional equations of two-phase flow at high resolution. It considers a uni-pore reservoir model with a constant porosity and permeability.

3.1. General Mass and Energy Balance Equation

The mass and heat balances for the two-phase flow problem are considered in every subdomain (gridblock), n. The simulation domain is subdivided by the integral finite difference method as follows (Pruess et al., 1998):

$$\frac{d}{dt}\int_{V_n} M^{\kappa} dV = \int_{\Gamma_n} F^{\kappa} \cdot n d\Gamma + \int_{V_n} q^{\kappa} dV \qquad (47)$$

where V is the volume of subdomain, t is time, Γ is the surface area of subdomain, q is the source or sink term, and the superscript represents component κ. The mass accumulation (M^{κ}) and the mass fluxes (F^{κ}) for every component under equilibrium conditions are given as follows:

$$M^{\kappa} = \sum_{\beta \equiv A,G} \phi S_{\beta} \rho_{\beta} x_{\beta}^{\kappa} \qquad (48)$$

$$F^{\kappa} = \sum_{\beta = A,G} F_{\beta}^{\kappa}\big|_{adv} + \sum_{\beta = A,G} F_{\beta}^{\kappa}\big|_{dif} \qquad (49)$$

where ϕ is the porosity of the porous medium, x_{β}^{κ} is mass fraction of component κ in phase β, S is the saturation, ρ is the density, and the subscript β refers to the phase of the component which may be aqueous (A) and gas (G) phases. The advective and diffusive mass fluxes for component κ are described as follows:

$$F_{\beta}^{\kappa}\big|_{adv} = -x_{\beta}^{\kappa}\left\{k\frac{k_{r\beta}\rho_{\beta}}{\mu_{\beta}}\left(\nabla P_{\beta} - \rho_{\beta} g\right)\right\} \qquad (50)$$

$$F_{\beta}^{\kappa}\big|_{dif} = -\phi S_{\beta} \tau_{\beta} \rho_{\beta} D_{\beta}^{\kappa} \nabla x_{\beta}^{\kappa} \qquad (51)$$

Here, g is the gravitational acceleration, k_r is the relative permeability, μ is the viscosity, τ is the tortuosity, and D_{β}^{κ} is the free-molecular diffusion coefficient of component κ in phase β. The superscript κ represents the component, which consists of water, methane gas, and salt. The subscript β represents the phase of the component, which consists of aqueous and gaseous phase. When the two phases, aqueous and gaseous phase coexist in the micro-crack, the following relation applied:

$$P_G = P_A + P_c \qquad (52)$$

In equation above, P_A and P_G are aqueous and gaseous pressure, respectively.

3.2. Discretization of Mass and Energy Balance Equations

The mass and energy balance equations are discretized in space using the integral finite difference method (Narasimhan and Witherspoon, 1976). The appropriate volume averages can be written as follows:

$$\int_{V_n} M dV = V_n M_n \qquad (53)$$

where M is a volume-normalized extensive quantity and M_n is the average value of M over V_n. Meanwhile, surface integrals are estimated as a discrete sum of averages over surface segments A_{nm} as follows:

$$\int_{\Gamma_n} F \bullet \mathrm{n} d\Gamma_n = \sum_m A_{nm} F_{nm} \qquad (54)$$

Here, F_{nm} is the average value of the (inward) normal component of F over the surface segments A_{nm} between volume elements V_n and V_m. The subscript nm represents a suitable averaging at the interface between grid block n and m such as interpolation, harmonic weighting and upstream weighting.

Substituting Equations (53) and (54) into the governing Equation (47) gives a set of first-order ordinary differential equation as follows:

$$\frac{dM_n^\kappa}{dt} = \frac{1}{V_n}\sum_m A_{nm}F_{nm}^\kappa + q_n^\kappa \qquad (55)$$

Time is discretized as a first-order finite difference, and the flux and sink/source terms are evaluated fully implicitly at the new time level t^{k+1} to acquire the numerical stability for efficient calculation in nonlinear problems. The resulting algebraic equations are shown in the following set of coupled non-linear algebraic equations:

$$R_n^{\kappa,k+1} = M_n^{\kappa,k+1} - M_n^{\kappa,k} - \frac{\Delta t}{V_n}\left[\sum_m A_{nm}F_{nm}^{\kappa,k+1} + V_n q_n^{\kappa,k+1}\right] = 0 \qquad (56)$$

Here, $R_n^{\kappa,\mathrm{k+1}}$ is the residuals of component κ at time $k+1$, in element n and Δt is the time step. Equation (56) represents a total of $N_E \times N_\kappa$ coupled non-linear equation where N_E is the number of elements (grid block) and N_κ is the number of equations for each volume element. Therefore, the unknowns are the $N_E \times N_\kappa$ independent primary variables (X_i, for $i = 1, \dots, N_E \times N_\kappa$).

The Equation (56) is solved using Newton/Raphson method. The residual $R_n^{\kappa,k+1}$ is expanded at iteration step $(p+1)$ in a Taylor series at index p as follows:

$$R_{n\,(X_{i,p+1})}^{\kappa,k+1} = R_{n\,(X_{i,p})}^{\kappa,k+1} + \sum_i \left.\frac{\partial R_n^{\kappa,k+1}}{\partial X_i}\right|_p \left(X_{i,p+1} - X_{i,p}\right) + \cdots = 0 \qquad (57)$$

Retaining the first order as a set of $N_E \times N_\kappa$ linear equation for the increments $\left(X_{i,p+1} - X_{i,p}\right)$ as follows:

$$-\sum_i \left.\frac{\partial R_n^{\kappa,k+1}}{\partial X_i}\right|_p \left(X_{i,p+1} - X_{i,p}\right) = R_n^{\kappa,k+1}{}_{(X_{i,p})} \qquad (58)$$

which all terms of $\frac{\partial R_n^{\kappa,k+1}}{\partial X_i}$ are used in the Jacobian matrix and evaluated by numerical differentiation. Iteration is proceeded until the residuals $R_n^{\kappa,k+1}$ are reduced below a preset convergence tolerance (ϵ_1) as follows:

$$\left|\frac{R_{n,p+1}^{\kappa,k+1}}{M_{n,p+1}^{\kappa,k+1}}\right| \leq \epsilon_1 \qquad (59)$$

An absolute convergent criterion is forced when the accumulation terms are less than ϵ_2 as follows:

$$R_{n,p+1}^{\kappa,k+1} \leq \epsilon_1 \epsilon_2 \qquad (60)$$

Here, the default value for ϵ_1 is in the range of 10^{-5} – 10^{-6} and ϵ_2 is 1. The nonlinearity of the problem affects the number or iteration to convergence. Frequently, convergence is achieved in three to ten iterations for well-behaved problems. In case convergence cannot be attained within a certain number of iterations, a new iteration process is started with smaller time step size, Δt.

3.3. Constitutive, Equilibrium Restriction and Constrain Equations

This section discusses the equations and correlations which are applied in numerical simulation. These consist of several equations and correlations for rock porous medium properties and for fluids thermo-physical properties.

3.3.1. The Equations of Porous Medium Properties

The porosity of porous medium is estimated as an exponential function of pressure, temperature, compressibility, and expansivity as follows:

$$\phi = \phi_{init} \mathrm{e}^{\left(C_{\phi}(P-P_{init})+\beta_t(T-T_{init})\right)} \qquad (61)$$

In the previous equation, C_{ϕ} is pore compressibility, β_t is pore thermal expansion, and the subscript $init$ represents the initial condition.

Meanwhile, the permeability of porous medium is correlated to the porosity based on the following exponential function of porosity (Rutqvist and Tsang, 2002; as a modifed equation from Davis and Davis, 1999):

$$k = k_0 e^{\left[22.2\left(\frac{\phi}{\phi_0}-1\right)\right]} \qquad (62)$$

where the subscript 0 represents the initial condition.

The thermal conductivity of the porous medium (λ_r) is calculated as a function of saturation in aqueous phase (Somerton et al., 1974) and rewritten as follows:

$$\lambda_r = \lambda_{r,dry} + \sqrt{S_A}\left(\lambda_{r,wet} - \lambda_{r,dry}\right) \quad (63)$$

3.3.2. The Thermo-Physical Properties of Water Equations

The thermo-physical properties of water, such as density and specific enthalpy are calculated using the IAWPS formulation, 1997 (Wagner et al., 2000). The water density in aqueous phase ($\rho_A^{H_2O}$) and the specific enthalpy in aqueous phase ($h_A^{H_2O}$) are related to pressure and temperature according to the following equations:

$$\rho_A^{H_2O} = \frac{P}{\pi R T \gamma} \quad (64)$$

$$h_A^{H_2O} = \tau R T \gamma \quad (65)$$

where R is the specific gas constant of ordinary water as equal to 0.461526 kJ kg^{-1} K^{-1} and γ is the dimensionless form of specific Gibbs free energy and expressed as follows:

$$\gamma = \sum_{i=1}^{34} n_i (7.1 - \pi)^{I_i} (\tau - 1.222)^{J_i} \quad (66)$$

In the Equations (64) – (66), the coefficient n_i and exponents I_i and J_i are listed in **Table 1**, while the parameters π and τ can be expressed as follows:

$$\pi = \frac{P}{16.53\ MPa} \quad (67)$$

$$\tau = \frac{T}{1386\ K} \quad (68)$$

Meanwhile, the water density in gaseous phase ($\rho_G^{H_2O}$) and the specific enthalpy in gaseous phase ($h_G^{H_2O}$) are related to pressure and temperature according to the following equations:

$$\rho_G^{H_2O} = \frac{P}{\pi RT\left(\frac{\partial \gamma^o}{\partial \pi} + \frac{\partial \gamma^r}{\partial \pi}\right)} \quad (69)$$

$$h_G^{H_2O} = \tau RT\left(\frac{\partial \gamma^o}{\partial \tau} + \frac{\partial \gamma^r}{\partial \tau}\right) \quad (70)$$

The equation for the ideal gas part of the dimensionless Gibbs free energy (γ^o) and the form of the residual part of the dimensionless Gibbs free energy (γ^r) for previous equations can be expressed as follows:

$$\gamma^o = \ln \pi + \sum_{i=1}^{9} n_i^o \tau^{J_i^o} \quad (71)$$

Table 1 – Coefficients and Exponents of the Dimensionless Form of Specific Gibbs Free Energy (Adopted from the IAWPS Formulation, 1997)

i	I_i	J_i	n_i	i	I_i	J_i	n_i
1	0	-2	1.4632971213167E-01	18	2	3	-4.4141845330846E-06
2	0	-1	-8.4548187169114E-01	19	2	17	-7.2694996297594E-16
3	0	0	-3.7563603672040E+00	20	3	-4	-3.1679644845054E-05
4	0	1	3.3855169168385E+00	21	3	0	-2.8270797985312E-06
5	0	2	-9.5791963387872E-01	22	3	6	-8.5205128120103E-10
6	0	3	1.5772038513228E-01	23	4	-5	-2.2425281908000E-06
7	0	4	-1.6616417199501E-02	24	4	-2	-6.5171222895601E-07
8	0	5	8.1214629983568E-04	25	4	10	-1.4341729937924E-13
9	1	-9	2.8319080123804E-04	26	5	-8	-4.0516996860117E-07
10	1	-7	-6.0706301568574E-04	27	8	-11	-1.2734301741641E-09
11	1	-1	-1.8990068218419E-02	28	8	-6	-1.7424871230634E-10
12	1	0	-3.2529748770505E-02	29	21	-29	-6.8762131295531E-19
13	1	1	-2.1841717175414E-02	30	23	-31	1.4478307828521E-20
14	1	3	-5.2838357969930E-05	31	29	-38	2.6335781662795E-23
15	2	-3	-4.7184321073267E-04	32	30	-39	-1.1947622640071E-23
16	2	0	-3.0001780793026E-04	33	31	-40	1.8228094581404E-24
17	2	1	4.7661393906987E-05	34	32	-41	-9.3537087292458E-26

Table 2 – Coefficients and Exponents of the Dimensionless Form of the Ideal Gas Part of Specific Gibbs Free Energy (Adopted from the IAWPS Formulation, 1997; Wagner et al., 2000)

i	J_i^o	n_i^o
1	0	-9.6927686500217E+00
2	1	1.0086655968018E+01
3	-5	-5.6087911283020E-03
4	-4	7.1452738081455E-02
5	-3	-4.0710498223928E-01
6	-2	1.4240819171444E+00
7	-1	-4.3839511319450E+00
8	2	-2.8408632460772E-01
9	3	2.1268463753301E-02

$$\gamma^r = \sum_{i=1}^{43} n_i \pi^{I_i} (\tau - 0.5)^{J_i} \qquad (72)$$

where, the coefficient n_i^o and exponent J_i^o for Equation (71) are listed in **Table 2**, and the coefficient n_i and exponent I_i and J_i used in Equation (72) are listed in **Table 3.**

Table 3 – Coefficients and Exponents of the Dimensionless Form of the Residual Part of Specific Gibbs Free Energy (Adopted from the IAWPS Formulation, 1997; Wagner et al., 2000)

i	I_i	J_i	n_i
1	1	0	-0.17731742473213E-2
2	1	1	-0.17834862292358E-1
3	1	2	-0.45996013696365E-1
4	1	3	-0.57581259083432E-1
5	1	6	-0.50325278727930E-1
6	2	1	-0.33032641670203E-4
7	2	2	-0.18948987516315E-3
8	2	4	-0.39392777243355E-2
9	2	7	-0.43797295650573E-1
10	2	36	-0.26674547914087E-4
11	3	0	0.20481737692309E-7
12	3	1	0.43870667284435E-6
13	3	3	-0.32277677238570E-4
14	3	6	-0.15033924542148E-2
15	3	35	-0.40668253562649E-1
16	4	1	-0.78847309559367E-9
17	4	2	0.12790717852285E-7
18	4	3	0.48225372718507E-6
19	5	7	0.22922076337661E-5
20	6	3	-0.16714766451061E-10
21	6	16	-0.21171472321355E-2
22	6	35	-0.23895741931404E+2
23	7	0	-0.59059564324270E-17
24	7	11	-0.12621808899101E-5
25	7	25	-0.38946842435739E-1
26	8	8	0.11256211360459E-10
27	8	36	-0.82311340897998E+1
28	9	13	0.19809712802088E-7
29	10	4	0.10406965210174E-18
30	10	10	-0.10234747095929E-12
31	10	14	-0.10018179379511E-8
32	16	29	-0.80882908646985E-10
33	16	50	0.10693031879409E+0
34	18	57	-0.33662250574171E+0
35	20	20	0.89185845355421E-24
36	20	35	0.30629316876232E-12
37	20	48	-0.42002467698208E-5
38	21	21	-0.59056029685639E-25
39	22	53	0.37826947613457E-5
40	23	39	-0.12768608934681E-14
41	24	26	0.73087610595061E-28
42	24	40	0.55414715350778E-16
43	24	58	-0.94369707241210E-6

The viscosity of water is calculate using the IAWPS formulation, 2008 (Cooper and Dooley, 2008) as follows:

$$\bar{\mu} = \overline{\mu_0} + \overline{\mu_1} + \overline{\mu_2} \qquad (73)$$

The first factor $\overline{\mu_0}$ represents the viscosity in the dilute-gas limit and is calculated as follows:

$$\overline{\mu_0} = \frac{100\sqrt{\bar{T}}}{\sum_{i=0}^{3} \frac{H_i}{\bar{T}^i}} \qquad (74)$$

with the coefficients H_i are given in **Table 4**.

The second factor $\overline{\mu_1}$ represents the contribution to viscosity due to finite density and is calculated by:

$$\overline{\mu_1} = exp\left[\bar{\rho}\sum_{i=0}^{5}\left(\left(\frac{1}{\bar{T}} - 1\right)^i \sum_{j=0}^{6} H_{ij}(\bar{\rho} - 1)^j\right)\right] \qquad (75)$$

with the coefficients H_{ij} are given in **Table 5**.

The third factor $\overline{\mu_2}$ represents the critical enhancement of the viscosity, which is assumed to be 10^{-6} for the industrial formulation.

Table 4 – Coefficients H_i in Equation for $\overline{\mu_0}$ (Adopted from the IAWPS Formulation, 2008; Cooper and Dooley, 2008)

i	H_i
0	1.67752
1	2.20462
2	0.6366564
3	-0.241605

Table 5 – Coefficients H_{ij} in Equation for $\overline{\mu_1}$ (Adopted from the IAWPS Formulation, 2008; Cooper and Dooley, 2008)

i	j			
	0	**1**	**2**	**3**
0	0.5200940	0.2225310	-0.2813780	0.1619130
1	0.0850895	0.9991150	-0.9068510	0.2573990
2	-1.0837400	1.8879700	-0.7724790	0
3	-0.2895550	1.2661300	-0.4898370	0
4	0	0	-0.2570400	0
5	0	0.1205730	0	0

i	j		
	4	**5**	**6**
0	-0.0325372	0	0
1	0	0	0
2	0	0	0
3	0.0698452	0	-0.0043567
4	0	0.0087210	0
5	0	0	-0.0005933

The thermal conductivity of water is calculate using the IAWPS formulation, 2011 (Huber et al., 2012) as follows:

$$\bar{\lambda} = \overline{\lambda_0} + \overline{\lambda_1} + \overline{\lambda_2} \qquad (76)$$

The first factor $\overline{\lambda_0}$ represents the thermal conductivity in the dilute gas limit and is calculated by:

$$\overline{\lambda_0} = \frac{\sqrt{\bar{T}}}{\sum_{k=0}^{4} \frac{L_k}{T^k}} \qquad (77)$$

with the coefficients L_k are given in **Table 6**.

The second factor $\overline{\lambda_1}$ represents the contribution to thermal conductivity due to finite density and is calculated by:

$$\overline{\lambda_1} = exp\left[\bar{\rho}\sum_{i=0}^{4}\left(\left(\frac{1}{\bar{T}}-1\right)^i \sum_{j=0}^{5} L_{ij}(\bar{\rho}-1)^j\right)\right] \qquad (78)$$

with the coefficients L_{ij} are given in **Table 7**.

The third factor $\overline{\lambda_2}$ represents the critical enhancement of the thermal conductivity, which is assumed to be 1 for the industrial formulation.

Table 6 – Coefficients L_k in Equation for $\overline{\lambda_0}$ (Adopted from the IAWPS Formulation, 2011; Huber et al, 2012)

k	L_k
0	2.443221E-03
1	1.323095E-02
2	6.770357E-03
3	-3.454586E-03
4	4.096266E-04

Table 7 – Coefficients L_{ij} in Equation for $\overline{\lambda_1}$ (Adopted from the IAWPS Formulation, 2011; Huber et al, 2012)

i	j					
	0	**1**	**2**	**3**	**4**	**5**
0	1.6039736	-0.6460135	0.1114439	0.1029974	-0.0504124	0.0060986
1	2.3377184	-2.7884378	1.5361617	-0.4630455	0.0832827	-0.0071920
2	2.1965053	-4.5458079	3.5577724	-1.4094498	0.2754183	-0.0205939
3	-1.2105138	1.6081299	-0.6211781	0.0716373	0	0
4	-2.7203370	4.5758633	-3.1836925	1.1168348	-0.1926831	0.0129138

3.3.3. The Thermo-Physical Properties of Methane Gas Equations

The thermo-physical properties of CH_4 gas, such as the density and specific enthalpy of CH_4 gas are estimated using Peng and Robinson (1976) equation of state. The density of CH_4 gas ($\rho_G^{CH_4}$) can be expressed as follows:

$$\rho_G^{CH_4} = \frac{P{M_w}^{CH_4}}{ZRT} \quad (79)$$

where ${M_w}^{CH_4}$ is the molecular weight of CH_4 gas and Z is the gas compressibility factor, which can be rewritten as follows:

$$Z^3 - (1 - B)Z^2 + (A - 3B^2 - 2B)Z - (AB - B^2 - B^3) = 0 \quad (80)$$

In the two-phase region, the largest root is for the compressibility factor of the vapor, while the parameter A and B can be expressed as follows:

$$A = \frac{a\alpha P}{R^2T^2} \quad (81)$$

$$B = \frac{bP}{RT} \quad (82)$$

which at the critical point, the variables a, α, and b can be expressed as follows:

$$a = 0.45724\frac{R^2T_c^2}{P_c} \quad (83)$$

$$B = 0.0778\frac{RT_c}{P_c} \quad (84)$$

$$\alpha^{0.5} = 1 + \kappa\left(1 - \left(\frac{T}{T_c}\right)^{0.5}\right) \quad (85)$$

Here, κ is a constant characteristic of each substance. This constant has been correlated against the acentric factor (ω) according to the following equation:

$$\kappa = 0.37464 + 1.54226\omega - 0.26992\omega^2 \quad (86)$$

Meanwhile, the specific enthalpy of CH_4 gas ($h_G^{CH_4}$) is obtained by using the following equation:

$$h_G^{CH_4} = h_{G,ideal}^{CH_4} + h_{G,departure}^{CH_4} \quad (87)$$

The specific enthalpy of ideal gas for CH_4 is calculated as a function of temperature (Poling et al., 2001) as follows:

$$h_{G,ideal}^{CH_4} = (4.568 - 8.975 \times 10^{-3}T + 3.631 \times 10^{-5}T^2 - 3.407 \times 10^{-8}T^3 + 1.091 \times 10^{-11}T^4)R \quad (88)$$

While, the enthalpy departure is calculated using thermodynamic equation (Peng-Robinson, 1976) as follows:

$$h_{G,departure}^{CH_4} = RT(Z-1) + \frac{T\frac{d(a\alpha)}{dT} - a\alpha}{2\sqrt{2b}} \ln\left(\frac{Z + 2.414B}{Z - 0.414B}\right) \quad (89)$$

The other thermo-physical properties, which are the viscosity and the thermal conductivity of CH_4 gas, are calculated using gas correlation (Sun and Mohanty, 2005). The viscosity correlation of gas phase (μ_G) as a function of temperature and gas density (ρ_G) is described as follows:

$$\mu_G = 2.4504 \times 10^{3} + 2.8764 \times 10^{-5}T + 3.279 \times 10^{-9}T^2 - 3.7838 \times 10^{-12}T^3 + 2.0891 \times 10^{-5}\rho_G + 2.5127 \times 10^{-7}\rho_G^2 + 5.822 \times 10^{-10}\rho_G^3 + 1.8378 \times 10^{-13}\rho_G^4 \quad (90)$$

Meanwhile the thermal conductivity correlation of gas phase (λ_G) is explained as a function of temperature, in the range of temperature between 97 and 1400 K. The equation is given as follows:

$$\lambda_G = -0.00935 + 1.4028 \times 10^{-4}T + 3.318 \times 10^{-6}T^2 \quad (91)$$

3.3.4. The Properties of Aqueous and Gaseous Phase Equations

The constraints for the mass fraction for each phase are applied as follows:

$$\sum_{\kappa} x_{\beta}^{\kappa} = 1 \quad (92)$$

The mass fractions of component κ in phase β, under equilibrium conditions are given as follows:

$$x_\beta^\kappa = \frac{y_\beta^\kappa {M_w}^\kappa}{\sum_\kappa \left(y_\beta^\kappa {M_w}^\kappa\right)} \quad (93)$$

where y_β^κ is the molar fraction of component κ in phase β and ${M_w}^\kappa$ is the molecular weight of component κ in phase β. The same constrains are also applied for the molar fractions for each phase as follows:

$$\sum_\kappa y_\beta^\kappa = 1 \quad (94)$$

The molar fraction of CH_4 gas in aqueous phase ($y_A^{CH_4}$) is predicted as follows:

$$y_A^{CH_4} = \frac{P^{CH_4}}{H^{CH_4}} \quad (95)$$

Here, H^{CH_4} is the Henry's constant for CH_4 gas, which can be explained as following equation (Sun and Mohanty, 2005):

$$\ln H^{CH_4} = 1.0E3\left(5.1345 + \frac{7837.0}{T} - \frac{1.509E6}{T^2} + \frac{2.06E7}{T^3}\right) \quad (96)$$

Meanwhile, the molar fraction of CH_4 gas in gaseous phase ($y_G^{CH_4}$) is calculated as following equation:

$$y_G^{CH_4} = \frac{P^{CH_4}}{P_G} \quad (97)$$

where P_G is the total pressure in gaseous phase, which can be described as the sum of partial pressure of CH_4 gas (P^{CH_4}) and water (P^{H_2O}) as follows:

$$P_G = P^{CH_4} + P^{H_2O} \quad (98)$$

The densities of each phase β within pore are described by following equation:

$$\rho_\beta = \sum_{\kappa=CH_4,H_2O,salt} x_\beta^\kappa \rho_\beta^\kappa \quad (99)$$

4. THE IMPACT OF CHEMO-THERMO-PORO-ELASTIC CHANGE ON SHALE RESERVOIR DURING SHUT-IN PERIOD

The objective of this modeling effort is to investigate the impact of non-uniform stress field due to temperature and chemical imbalance between fracture and formation during shut-in period of hydraulic fracturing on shale formation.

4.1. Mathematical Model of Non-Uniform Stress Field in Chemo-Thermo-Poro-Elastic System

The following sections will discuss the development of the numerical simulator, which including chemo-thermo-poro-elastic system, to understand the non-uniform stress field effect in shale formation. The main focus of this study is to see the contribution of temperature and chemical imbalance between fracturing fluids and formation fluids during shut-in period of hydraulic fracturing process.

4.1.1. Mathematical Model of Thermo-Poro-Elastic System

The simulation model for this study is based on mass and heat balances for the two-phase flow problem, which have been described in **Chapter 3**. In addition, the simulation model in this chapter has been modified to include heat balance and coupled with multi-porosity medium equation (Fakcharoenphol et al., 2013), which the detail derivation of this formulation can be seen at the **Appendix**. Meanwhile, the heat accumulation (M^{Θ}) is calculated as:

$$M^{\Theta} = (1-\phi)\rho_R C_R T + \sum_{\beta=A,G} \phi S_\beta \rho_\beta U_\beta \qquad (\ 100\ )$$

In equation above, C is the heat capacity, T is temperature, U is the specific internal energy, and the subscript R refers to properties of the rock. The specific internal energy is related to the specific enthalpy (h) and is estimated from:

$$U_\beta = h_\beta - \frac{P_\beta}{\rho_\beta} \qquad (101)$$

and the heat flux (F^Θ) is calculated as:

$$F^\Theta = -\left[(1-\phi)K_R + \sum_{\beta=A,G} \phi S_\beta K_\beta\right]\nabla T + \sum_{\beta=A,G} h_\beta F_\beta^\Theta \qquad (102)$$

In equation above, K is thermal conductivity. The conduction and convection heat transfer are describes in the first and second terms of the right hand side equation. The conductive-convective heat transfer may occur in intermediate-permeable formation or in a permeability range of 1 micro-Darcy to 1 mili-Darcy, while heat convection may have significant influence in a high permeability formation or for the permeability more than 1 mili-Darcy. In most studies (Perkins and Gonzales (1984)), heat transfer from the wellbore into the formation is due solely to conduction. Meanwhile heat convection can be neglected during heat transfer process because the extremely low fluid velocity in shale formation. This assumption has been strengthen by study of Wang and Papamichos (1994). According to them, heat conduction is more dominate than heat convection during heat transfer process in low-permeable porous medium like shale formation. However, in this study we still consider convection still occurred during heat transfer as shown in previous equation. The heat balance for multi-phase flow system including geomechanical formula is given below:

$$\frac{d}{dt}\left\{\left[1-\left[\frac{3(1-2v)}{E}(\bar{\sigma}-[\alpha P_A+3\beta_t K\omega\Delta T])\right]\right][1-\phi_I]\rho_R C_R T+\phi_I S_A\rho_A\left(h_A-\frac{P_A}{\rho_A}\right)+(\phi_I S_G\rho_G)\left(h_G-\frac{P_G}{\rho_G}\right)\right\}=\nabla\left\{[-[(1-\phi_I)K_R+\phi_I S_A K_A+\phi_I S_G K_G]\nabla T]+\left[h_A k\frac{k_{rA}\rho_A}{\mu_A}(\nabla P_A-\rho_A g)+h_G k\frac{k_{rG}\rho_G}{\mu_G}(\nabla P_G-\rho_G g)\right]\right\}+q^{heat} \quad (103)$$

4.1.2. Mathematical Model of Chemo-Thermo-Poro-Elastic System

In this section, the chemical contribution will be added into thermo-poro-elastic system. The impact of chemical osmosis on shale formation will be investigated during non-isothermal condition. In order to model the swelling that happened in the matrix, the shale matrix by the fracture is treated as multi-scale porosity medium including inorganic slit-shaped and interlayer clay porosity fields.

The developed simulator is modified by including water and gas phases with H_2O, CH_4, and salt components. The inorganic pores contain H_2O, CH_4, and salt components in aqueous and gas phases. Lastly, the clay pores contain H_2O, CH_4, and salt components in aqueous phase only. Flow and transport between the discretized grids only pass through the inorganic micro-cracks. The complete mass balance equations for water, CH_4, and salt and heat balance equation for dual porosity system are written as follows:

Mass Balance Equation for H_2O:

$$\frac{d}{dt}\left\{\phi_I S_A\rho_A x_A^{H_2O}+\phi_I S_G\rho_G x_G^{H_2O}\right\}=\nabla\left\{-x_A^{H_2O}k\frac{k_{rA}\rho_A}{\mu_A}(\nabla P_A-\rho_A g)-\phi_i S_A\tau_A\rho_A D_A^{H_2O}\nabla x_A^{H_2O}-x_G^{H_2O}k\frac{k_{rG}\rho_G}{\mu_G}(\nabla(P_A+P_c)-\rho_G g)-\phi_i S_G\tau_G\rho_G D_G^{H_2O}\nabla x_G^{H_2O}\right\}+w_A^{H_2O}+q^{H_2O} \quad (104)$$

Mass Balance Equation for CH_4:

$$\frac{d}{dt}\{\phi_I S_A \rho_A x_A^{CH_4} + \phi_I S_G \rho_G x_G^{CH_4}\} = \nabla\left\{-x_A^{CH_4} k \frac{k_{rA}\rho_A}{\mu_A}(\nabla P_A - \rho_A g) - \phi_i S_A \tau_A \rho_A D_A^{CH_4} \nabla x_A^{CH_4} - x_G^{CH_4} k \frac{k_{rG}\rho_G}{\mu_G}(\nabla(P_A + P_c) - \rho_G g) - \phi_i S_G \tau_G \rho_G D_G^{CH_4} \nabla x_G^{CH_4}\right\} + w_A^{CH_4} + q^{CH4} \quad (105)$$

Mass Balance Equation for Salt:

$$\frac{d}{dt}\{\phi_I S_A \rho_A x_A^{salt}\} = \nabla\left\{-x_A^{salt} k \frac{k_{rA}\rho_A}{\mu_A}(\nabla(P_A + P_c) - \rho_A g) - \phi_i S_A \tau_A \rho_A D_A^{salt} \nabla x_A^{salt}\right\} + w_A^{salt} + q^{salt} \quad (106)$$

Heat Balance Equation:

$$\frac{d}{dt}\left\{\left[1 - \left[\frac{3(1-2v)}{E}\left(\bar{\sigma} - \left[\alpha\left(P_{A,I} + P_{A,Clay}\right) + 3\beta_t K \omega \Delta T\right]\right)\right]\right][1 - (\phi_I + \phi_{Clay})]\rho_R C_R T + (\phi_I S_A \rho_A + \phi_C \rho_{Clay})\left(H_A - \frac{P_A}{\rho_A}\right) + (\phi_I S_G \rho_G)\left(H_G - \frac{(P_A + P_c)}{\rho_G}\right)\right\} = \nabla\left\{-[(1-\phi_I)K_R + \phi_I S_A K_A + \phi_I S_G K_G]\nabla T + h_A k \frac{k_{rA}\rho_A}{\mu_A}(\nabla P_A - \rho_A g) + h_G k \frac{k_{rG}\rho_G}{\mu_G}(\nabla(P_A + P_c) - \rho_G g)\right\} + q^{heat} \quad (107)$$

There are three thermo-physical states establish in the matrix and fracture domains during simulation. The states are the aqueous single-phase, the gaseous single-phase, and the aqueous-gaseous two-phase in matrix domain and the two-aqueous-gaseous phase in fracture domain. Each domain and each state consist of seven primary variables (X_i) as the unknown to solve seven residual equations. These primary variables are described in **Table 8**, which consist of aqueous pressures in micro-crack and clay pores ($P_{A,}, P_{A,Clay}$), molar fractions of methane gas, water, and salt components in aqueous and gaseous phases ($y_A^{CH_4}, y_G^{CH_4}, y_A^{Salt}, y_{A,Clay}^{Salt}$), mean normal stress ($\bar{\sigma}$), gaseous saturation ($S_G$), and temperature ($T$).

Table 8 – Primary Variables and States in Multi-Porosity Shale Gas Reservoir System

Primary Variable (X_i)	State
$P_A, y_A^{CH_4}, y_A^{Salt}, y_{A,Clay}^{Salt}, \overline{\sigma}, P_{A,Clay}, T$	Aqueous single-phase
$P_A, y_G^{CH_4}, y_{A,Clay}^{Salt}, y_{A,Clay}^{H_2O}, \overline{\sigma}, P_{A,Clay}, T$	Gaseous single-phase
$P_A, S_G, y_A^{Salt}, y_{A,Clay}^{Salt}, \overline{\sigma}, P_{A,Clay}, T$	Aqueous-gaseous two-phase

In table above, the subscript $Clay$ following parameter molar fractions ($y_{A,Clay}^{Salt}; y_{A,Clay}^{H_2O}$) and aqueous pressure ($P_{A,Clay}$) represents that the variables are simulated in the clay pores. Other unknown variables are solved by using constitutive, equilibrium restriction, and constraint equations, which have been explained in previous **Chapter 3**.

4.2. Validation of the Numerical Model with the Experiment

The numerical simulation and mathematical model of single-phase flow through clay with osmosis effect are validated by comparing with a simple clay experiment has previously been performed by Keijzer (2000) and described in Bader and Kooi (2005). The experiment was performed to investigate the semi-permeable behavior of clayey material. The experiment was conducted by letting a uniform flow of a salt solution through bentonite clay sample, which is confined by two porous stone. The porous stone separates the clay from one end of the sample, which is connected to a closed reservoir containing high salt concentration solution with the other side of the sample, which is connected to an open reservoir containing low salt concentration solution, as shown in **Figure 16**. The parameters used in core flooding experiment are given in **Table 9.** For the numerical simulation, the single water phase and the salt type of NaCl is used in the simulation. The closed boundary with no-flow is applied at the wall of the porous stone I and the constant pressure of 72.5 psi is applied at the wall of the porous stone II. The simulation was run on 25 grid blocks which have the porous stone and clay sample characteristics by keeping

a constant pressure on the open porous stone. The comparison between values from simulation results and experiment data is shown in **Figure 17**.

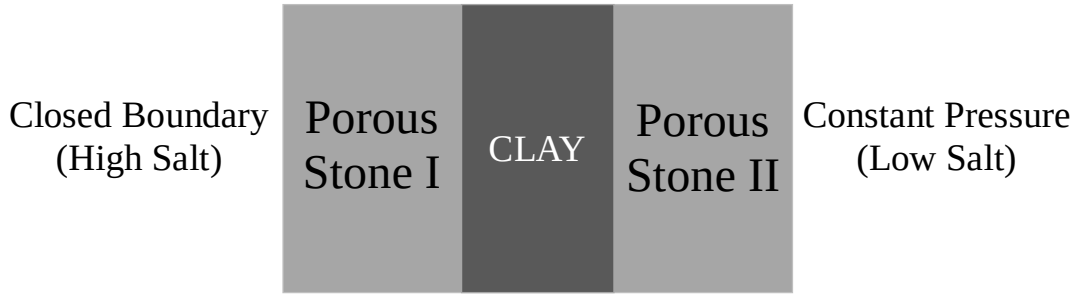

Fig. 16 – Modeling domain Keijzer experiment, adapted from Bader and Kooi (2005)

Table 9 – Parameter Input Used in the Simulation of the Keijzer Experiment (Keijer, 2000; Bader and Kooi, 2005)

Parameter	Porous Stone I	Clay	Porous Stone II	Unit
Pressure	72.5	72.5	72.5	psi
Temperature	25	25	25	^{o}C
Porosity	0.5	0.56	0.5	
Permeability	1.00E-13	1.20E-19	1.00E-13	m^2
Salt concentration	0.1	0.1	0.01	mol/L
Membrane efficiency	0	0.019	0	
Salt diffusion coefficient	1.20E-10	2.60E-13	1.20E-10	m^2/s

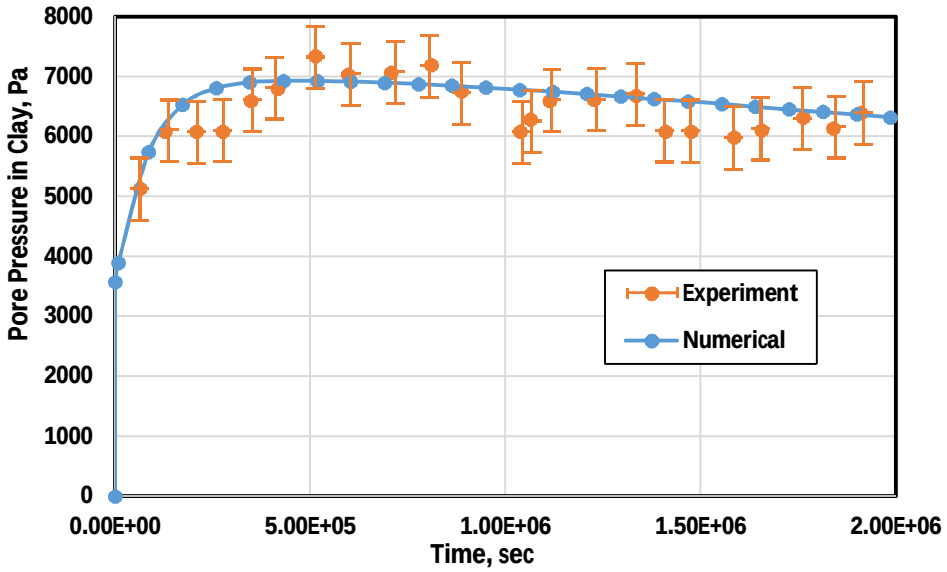

Fig. 17 – Comparison of the simulation results with the osmosis experiment results on clay sample data (Keijner, 2000; Bader and Kooi, 2005). The experimental data is the solid red circles and the numerical simulation results are shown as the solid blue circles.

4.3. Initial, Boundary Conditions, and Reservoir Parameters

In the first study, a one-dimensional uni-pore reservoir flow simulation model is considered to represent a quarter of a single vertical hydraulic fracture perpendicular to a horizontal well and the adjacent stimulated shale gas volume. The model has length of 5.5m on x-direction, which is divided into 55 grid blocks with the first grid block on the left considered as the fracture element as illustrated in **Figure 18**. The input parameters for matrix elements used in the simulation study are presented in **Table 10**.

At initial time, the water saturation of the matrix grid blocks is assumed to be at 29% irreducible water saturation with maximum capillary pressure value. The initial temperature of matrix grid blocks is varies from 75^{o}C to 105^{o}C considering 5 separate cases in order to show the impact of temperature imbalance during shut-in period. Meanwhile, the fracture element, which has quite large permeability relative to the other reservoir elements, is assumed to hold 100% of fresh fracturing water. The initial

temperature of the fracture is 35ºC for the isothermal case and 75ºC for non-isothermal cases. There is no capillary pressure within the fracture because only water exists. The pressure is initially uniform and equal to 3,800 psi in all the elements.

In the second study of non-uniform stress field, the contribution of osmosis mechanism will be considered during simulation. Instead of 18% inorganic porosity, which is used in previous study, the matrix elements porosity in current simulation model consists of 8% inorganic porosity and 10% clay porosity. Hence the total porosity is partitioned but still adds up to the base case porosity value. The inorganic micro-cracks porosity contains CH_4, H_2O, and salt components in both aqueous and gas phases, while the clay porosity contains those three components only in the aqueous phase. The clay pores fluid flows and transports the components between the discretized elements through the inorganic micro-cracks. Initially, the formation fluid contains salt mass fraction of 0.1, while the fracturing fluid is nearly fresh water with salt mass fraction of 0.02. The additional parameters on matrix element which are used for simulating osmosis mechanism on shale formation are displayed on **Table 11**.

The simulation model then is run for 2.4 hours of shut-in by using closed boundary with no-flow at both the inner and outer matrix grid block to perform shut-in period.

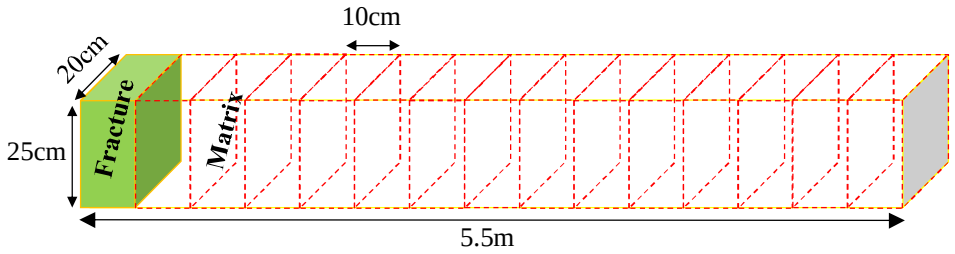

Fig. 18 – One dimensional simulation system model (55 x 1 x 1) to represent a single vertical hydraulic fracture that perpendicular to horizontal well.

Table 10 – Input Reservoir Parameters and their Base Values for the Simulation Study

Parameter	Value	Unit
Initial pore pressure	3800	psi
Initial temperature	75	Celsius
Porosity	0.18	
Permeability	66	nD
S_{iw}	29	percent

Parameter	Value	Unit
v	0.3	
α	0.5	
E	3.00E+10	Pa
β_t	0	
Grid System	5.5m x 0.25m x 0.2m (55x1x1)	

Table 11 – The Additional Input Parameters and Their Base Values for the Second Simulation Study

Clay Parameter	Value	Unit
Initial pore pressure	3800	psi
Porosity	0.1	fraction
Permeability	0.1	nD
Shape factor	0.01	dimensionless
C_{EC}	40	meq/100gr

Gangi Model Parameter	Value	Unit
k_0	0.01	mD
m	0.5	dimensionless
P_1	26000	psi
P_{conf}	15000	psi
α	0.5	dimensionless

4.4. Simulation Result and Discussion

This section discusses the simulation results of non-uniform stress field during shut-in period into three parts. First, the impact of temperature imbalance during shut-in periods will be investigated. The second part will discuss the impact of osmosis mechanism as addition of temperature effect. The last part will discuss the sensitivity of simulation on brine salinity.

4.4.1. The Impact of Temperature Imbalance on Shale Formation

The simulation included only 2.4 hours of shut-in period because the impact of temperature in the formation develops fast during the early time period. There are two transport mechanisms during simulation of non-isothermal cases. The heat transfer occurs from hot formation into cold fluid region near the fracture and the fracture water absorption by the matrix due to spontaneous imbibition. As shown in **Figure 19,** the fracture temperature of non-isothermal cases (color lines), which is initially lower than formation (35ºC), starts rising fast to balance the formation temperature (75ºC – 105ºC). The system has reached equilibrium at the first fifteen minutes of shut-in periods. In this graph, the isothermal case is shown by the black line.

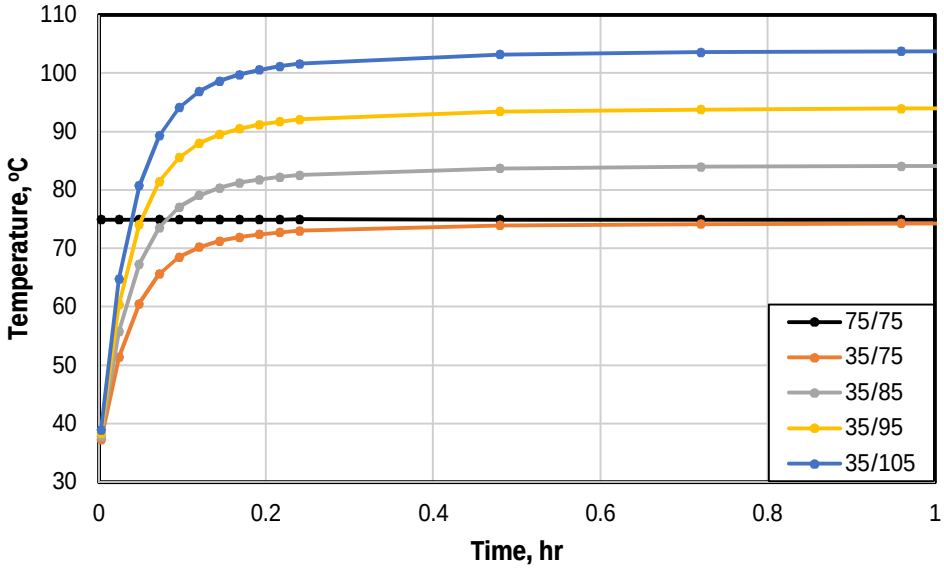

Fig. 19 – Simulation results of temperature on the first matrix grid block during shut-in period. The black line represents isothermal case and the color lines represent non-isothermal cases. The legend of 35/75 represents the fracture temperature of 35ºC and the formation temperature of 75ºC. The system has reached equilibrium at the first fifteen minutes of shut-in periods.

The first reservoir quality which is influenced by the temperature difference between fracture and formation is water saturation distribution. As we can see in **Figure 20**, the water saturation in the first matrix element adjacent to the fracture increases constantly in time during shut-in period under isothermal condition (black line). Meanwhile, in the non-isothermal cases, the hotter formation fluid tends to increase the water absorption during shut-in period because capillary pressure increases with the formation temperature escalation. High capillary pressure causes the water absorption because spontaneous imbibition becomes stronger. High temperature also increases rock expansion so that it reduces the pore volume of the formation and leads to increase in water saturation. However, the change in water saturation due to temperature alteration is less significant since the water saturation only increases around 5% for maximum reservoir temperature.

The main impact of temperature on water saturation can be seen more clearly on the change of water saturation curve behavior. The figure shows that the water saturation increases persistently all the time in the isothermal case. Meanwhile there are three phases of water saturation absorption during shut-in period in cases of non-isothermal condition. First, the water saturation rises fast in the very early time following drastic changes in temperature. Then, the water saturation reaches a plateau when temperature between the fracture and the formation closes each other. Finally, the water saturation increases steadily when temperature imbalance between formation and fracture disappears.

Figure 21 shows the pressure profile after the well is shut-in for 0.1, 1, 4, 8, 15 minutes and 2.4 hours. As soon as the shut-in period begins, the adjacent shale formation elements which initially have 29% water saturation start absorbing water fast and reaching to 100% saturation levels close to the fracture which contains the cold fracturing fluid. This initial mass flux is due to the spontaneous imbibition caused by high capillary pressure in the nearby shale matrix elements. This leads to drop in the fracture pressure around 60 psi because no fluid flows from inner boundary to maintain the pressure. The computed pressure decreases propagating from the grid block adjacent to the fracture toward the outer boundary.

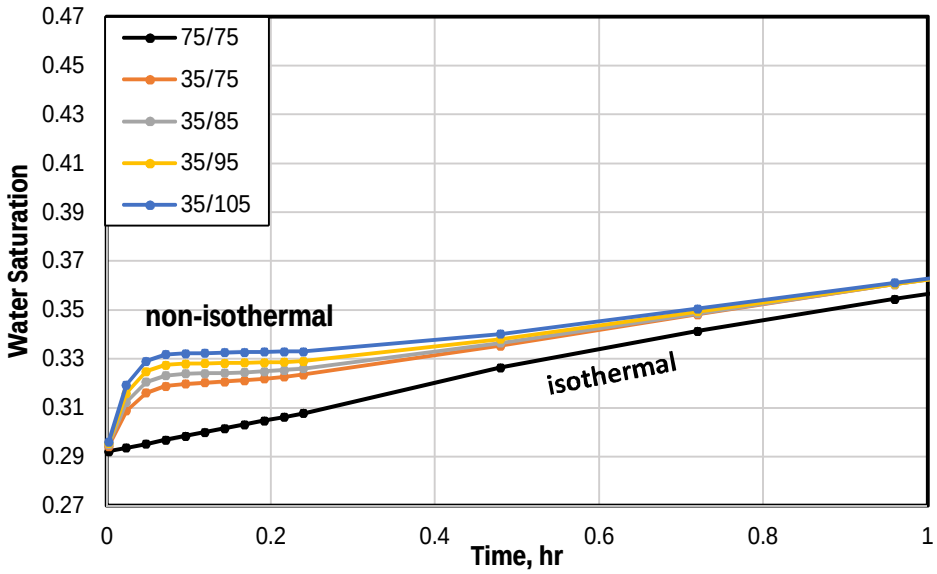

Fig. 20 – Simulation results of the computed water saturation vs time on the first matrix grid block during shut-in period. The black line represents isothermal case and the color lines represent non-isothermal cases. Temperature imbalance influences the water near the fracture.

The heat transfer process to balance the temperature in the fracture and formation causes additional pressure drop in the non-isothermal case. The larger difference between formation and the fracture temperatures tends to give additional pressure drop. The pressure drop occurs 15 cm away from the fracture, where the cold fluid region is located. However, the drop is too small to make a significant impact to water pressure as shown in **Figure 21**.

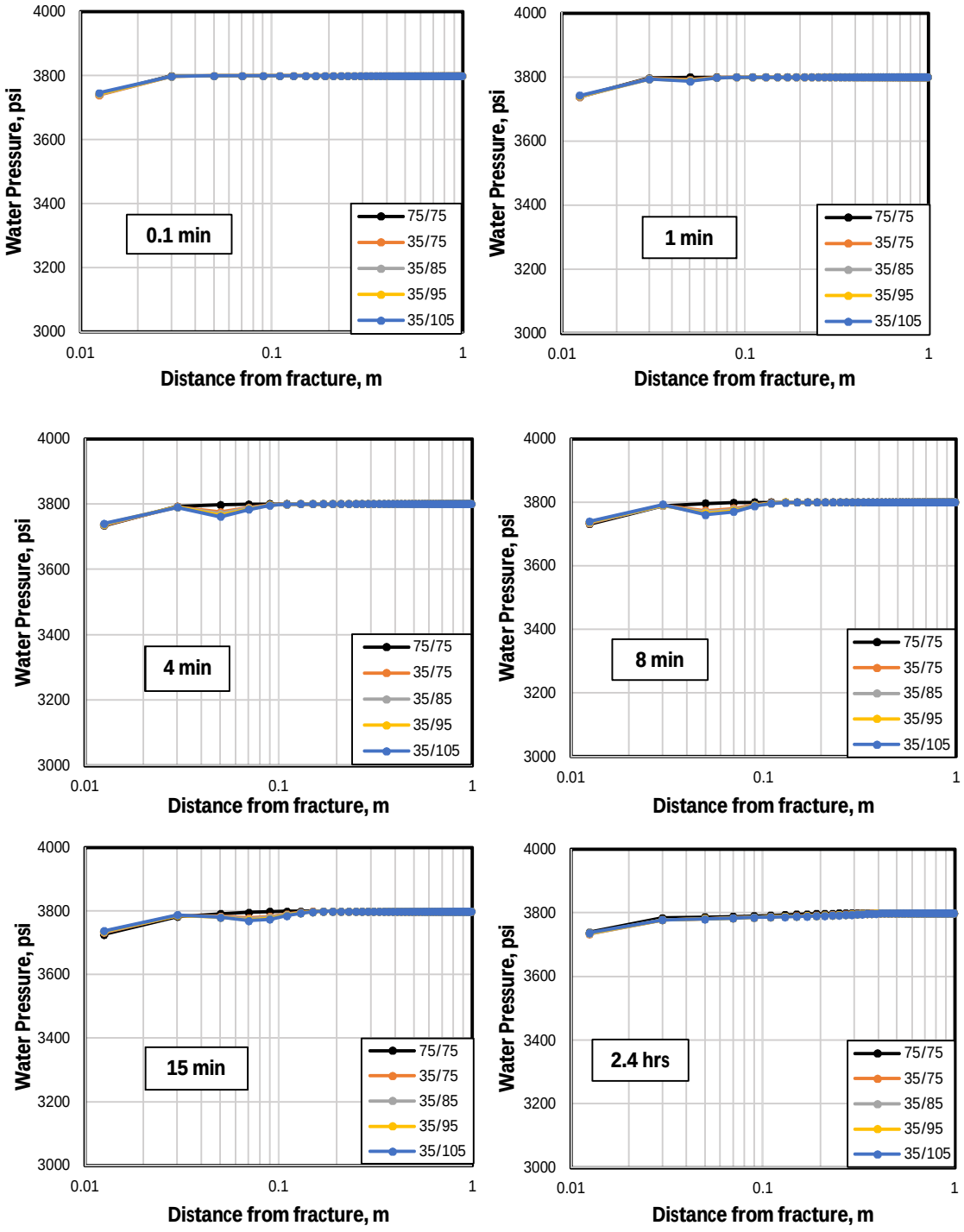

Fig. 21 – Simulation results of the computed pressure profile. The black line represents isothermal case and the color lines represent non-isothermal cases. Larger temperature imbalance tends to lower the compute pressure drops.

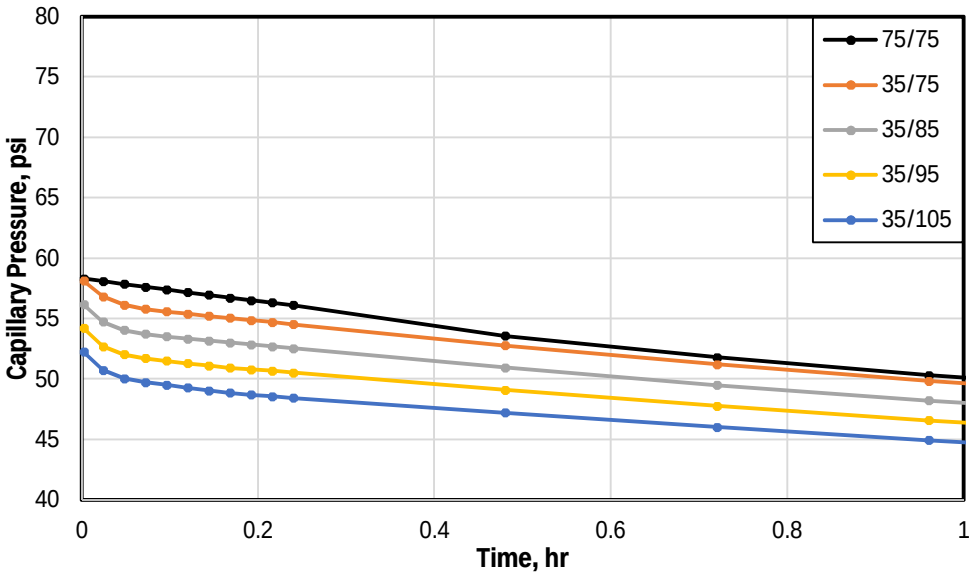

Fig. 22 – Simulation result of capillary pressure vs time on the first matrix grid block during shut-in period. The black line represents isothermal case and the color lines represent non-isothermal cases. Higher formation temperature tends to lower the capillary pressure. Rapid decline rate at early time due to heat transfer.

Capillary pressure is another parameter sensitive to temperature change since capillary pressure is not only affected by temperature directly but also by the changes in fluids densities, porosity, and permeability. Higher formation temperature tends to lower capillary pressure as shown in **Figure 22**. Higher temperature also reduces fluids densities and porosity and increases permeability. As a result, the capillary pressure drops significantly. The capillary pressure drops faster at the very early time when temperature imbalance between fracture and formation occurs. However, decline rates of capillary pressure are all similar regardless of the temperature difference. The decline rate becomes slower when fracture temperature has already close to formation temperature.

The impact of temperature during shut-in period is traced more clearly on mean normal stress profile after 4 minutes shut-in as shown in **Figure 23**. The computed mean normal stress ($\bar{\sigma}$) decreases drastically at 3 cm away from the fracture under non-

isothermal condition. The larger gap between fracture and formation temperature tends to lower normal mean stress. We can see here the shortest temperature gap (orange line) drops the mean normal stress around 375 psi while the longest temperature gap (blue line) drops the mean stress around 900 psi.

The impact of temperature imbalance is reduced after 2.4 hours shut-in as shown in **Figure 24**. The mean normal stress reduction become smaller for all non-isothermal cases. The mean normal stress only drops 40 to 70 psi. However, the impact of temperature gap still affects the reduction. The reduction is only noticeable 5 cm away from the fracture, where the cold fluid region is formed. Outside cold fluid region, the mean normal stress back to its initial. Meanwhile, there is not any significant impact on mean normal stress during isothermal case.

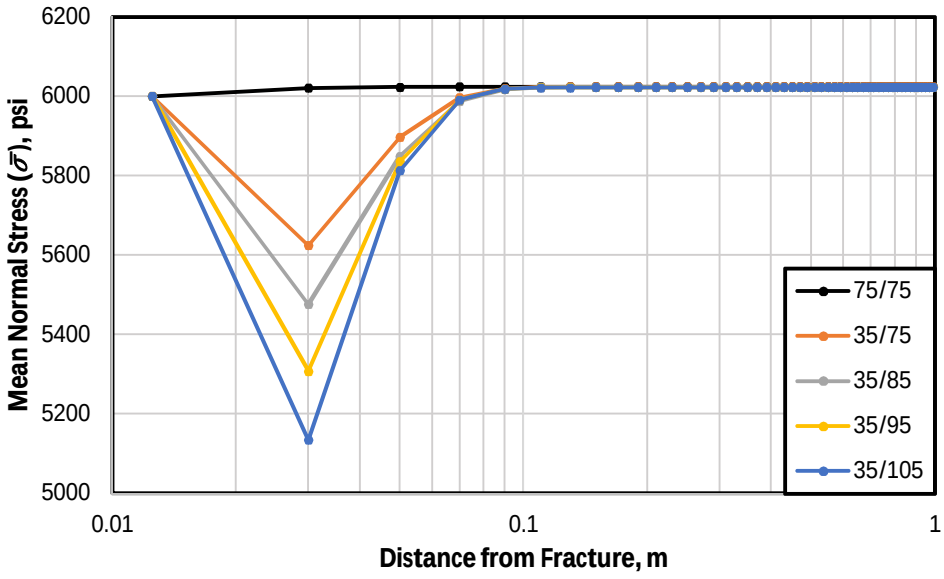

Fig. 23 – Simulation result of mean normal stress profile after 4 minutes shut-in. The black line represents isothermal case and the color lines represent non-isothermal cases. Larger temperature imbalance tends to lower mean normal stress reduction.

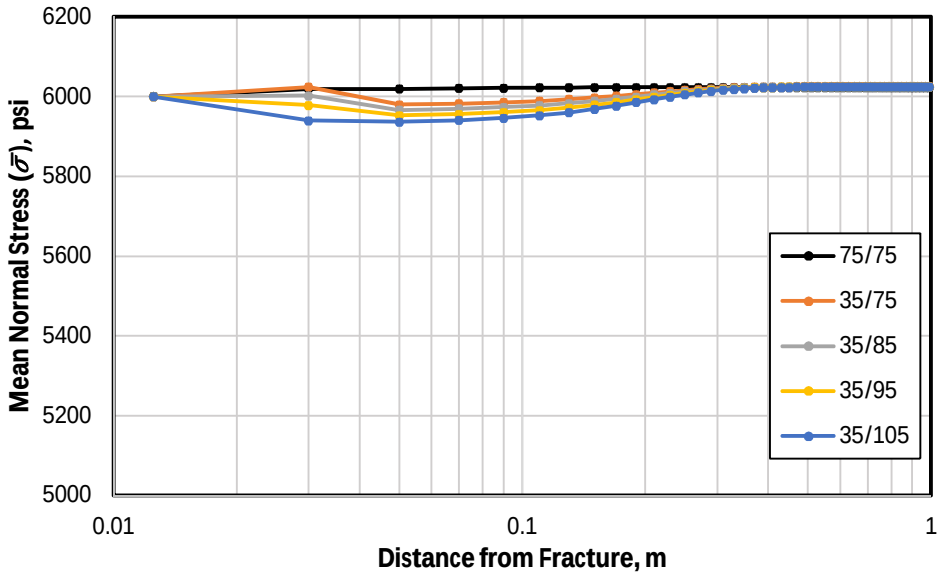

Fig. 24 – Simulation result of mean normal stress profile after 2.4 hour shut-in. The black line represents isothermal case and the color lines represent non-isothermal cases. Mean normal stress reduces in the non-isothermal cases and increases in isothermal case.

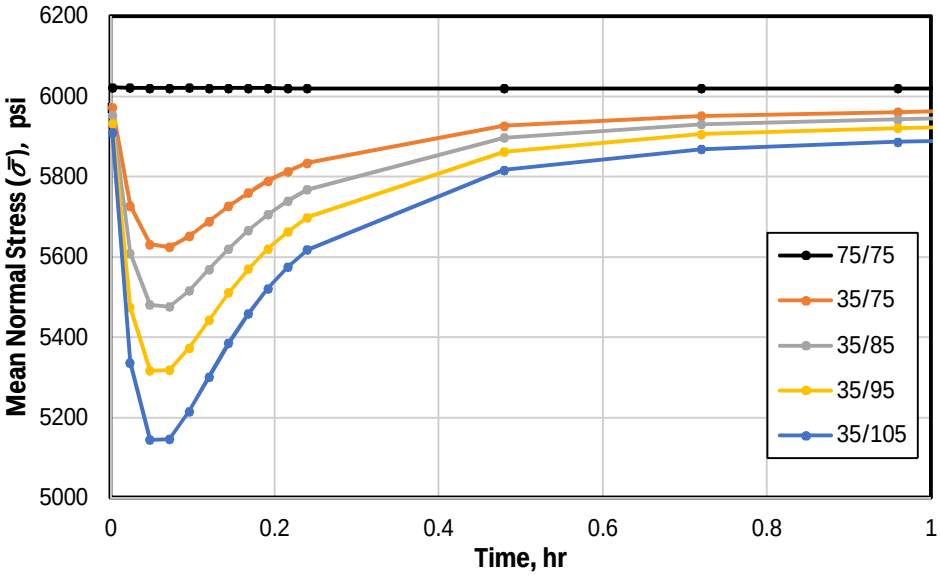

Fig. 25 – Simulation result of mean normal stress vs time on the first matrix grid block during shut-in period. The black line represents isothermal case and the color lines represent non-isothermal cases. Larger temperature imbalance tends to lower mean normal stress reduction.

The impact of temperature change on mean normal stress at the first grid block is shown in **Figure 25**. Temperature imbalance under non-isothermal condition, causes mean normal stress drop drastically at the early time. The impact develops fast, around less than 15 minutes after the shut-in period begins before the normal stress rises back to its initial condition value. On the contrary, the mean normal stress stays low in the first 15 minutes shut-in period before it starts increasing slowly and constantly all the time during simulation in isothermal condition

The opposite result occurs on permeability change. As we can see in **Figure 26** and **Figure 28**, the graph of permeability change percentage looks as the reverse of the mean normal stress graph. While the mean normal stress of the cold region in the formation shows higher reduction condition as the temperature gap between fracture and formation fluid becomes larger during non-isothermal, the shale formation permeability, which initially tight, expands because of thermal process in cold region as shown in **Figure 26**. A decrease in mean normal stress tends to increase the net effective stress. As a results, the formation permeability expands significantly with the decrease in the mean normal stress. The larger temperature imbalance tends to increase permeability more with the range from 7% for the lowest difference gap (orange line) and 17% for the highest (blue line). According to Perkins and Gonzales (1985), the secondary fracture eventually create complex fracture network by extending the cold water injection. This study result confirms their observation since permeability increases with higher temperature differences between formation and the fracture even after the well is shut-in.

After 2.4 hours, when the temperature field reaches a new equilibrium, the permeability of formation drops as shown in **Figure 27**. On the other hand, during simulation in isothermal condition, the change in net effective stress due to pressure drop causes the permeability of the formation decrease constantly.

Figure 28 shows the behavior of permeability vs time at the first grid block. The impact of thermal effect only occurs for around 15 minutes. Larger temperature imbalance tends to increases permeability. After temperature balances is reached, the impact from

water imbibition and pressure withdrawal becomes more dominant on affecting the permeability as well as mean normal stress at **Figure 25**. The mean stress continues increasing slowly which leads to decrease in the permeability.

In addition to this, heat transfer from hot formation to the cold region near the fracture reduces the porosity of the formation. However, the impact of temperature imbalance to the porosity is insignificant, in the range of 0.1– 0.2%.

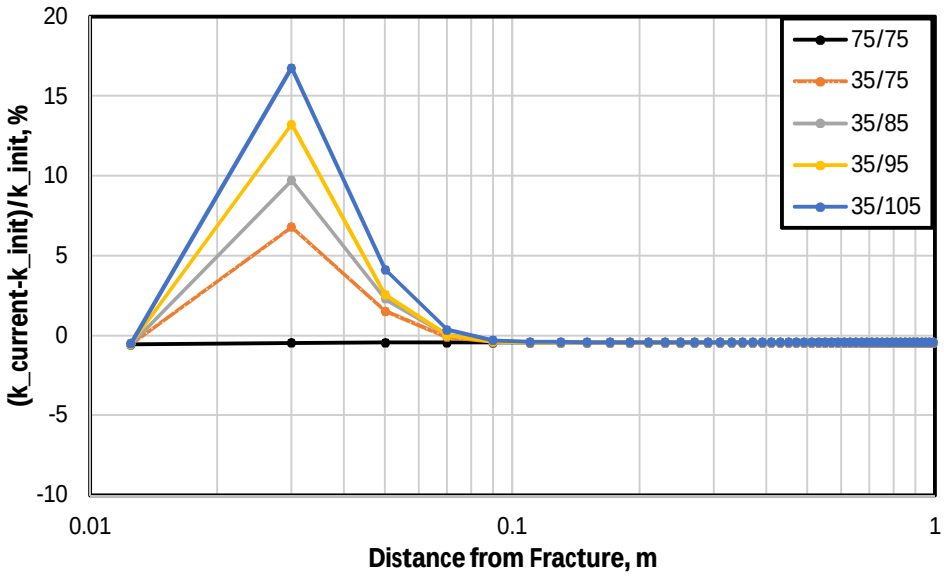

Fig. 26 – Simulation result of permeability change percentage profile after 4 minutes shut-in. The black line represents isothermal case and the color lines represent non-isothermal cases. Larger temperature imbalance tends to increases the formation permeability higher.

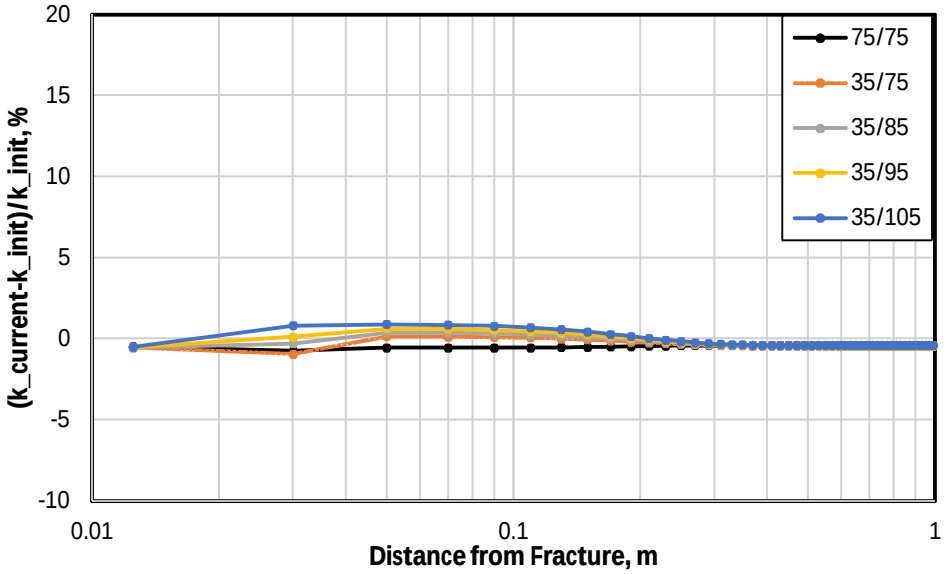

Fig. 27 – Simulation result of permeability change percentage profile after 2.4 hour shut-in. The black line represents isothermal case and the color lines represent non-isothermal cases. Permeability reduction decreases under the non-isothermal condition and increases under isothermal condition.

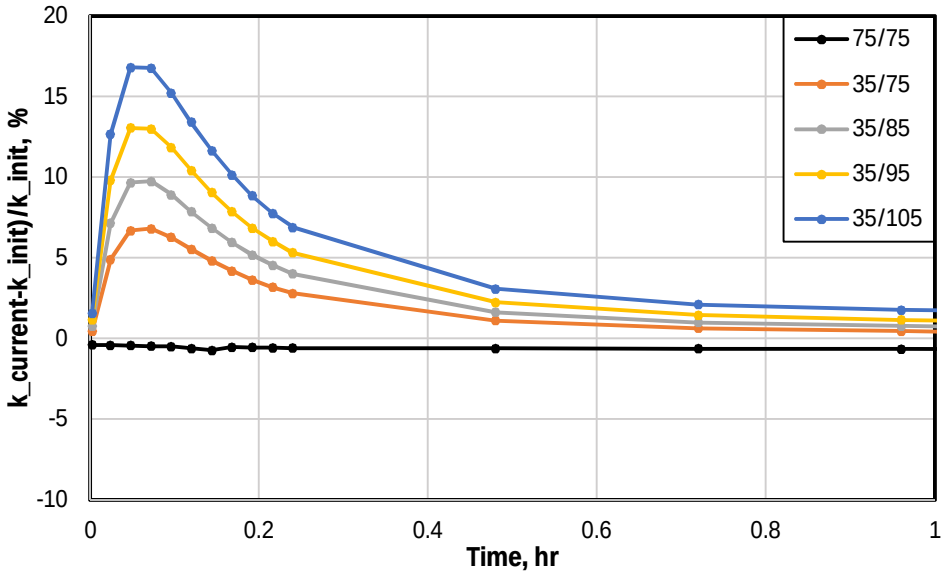

Fig. 28 – Simulation result of permeability change percentage vs time on the first matrix grid block during shut-in period. The black line represents isothermal case and the color lines represent non-isothermal cases. Larger temperature imbalance tends to increase the formation permeability higher.

4.4.2. The Impact of Chemical Imbalance on Shale Formation

This section will investigate the impact of osmosis mechanism in addition to thermal effect on shale formation as part of chemo-thermo-poro-elastic system behavior. In the clay pores, the effective stress does not give any significantly impact to the formation damage. The increase of pore pressure by hydraulic pressure tends to open the clay-pores and makes the permeability larger. However, when the water is invading clay-pores, the clay-pore pressure is also increasing in time and propagate from the grid blocks near hydraulic facture element toward the outer boundary. There is an alternately fluid exchange between micro-cracks and clay pores due to hydraulic pressure and osmosis. When the micro-crack pressure builds up decreases because the fluid saturation and the capillary pressure of hydraulic fracture element are equalized with the nearby matrix elements, the clay-pores pressure takes a charge of the system. An increased net confining stress due to the invasion of fracture water decreases the pore pressure and reduces the permeability.

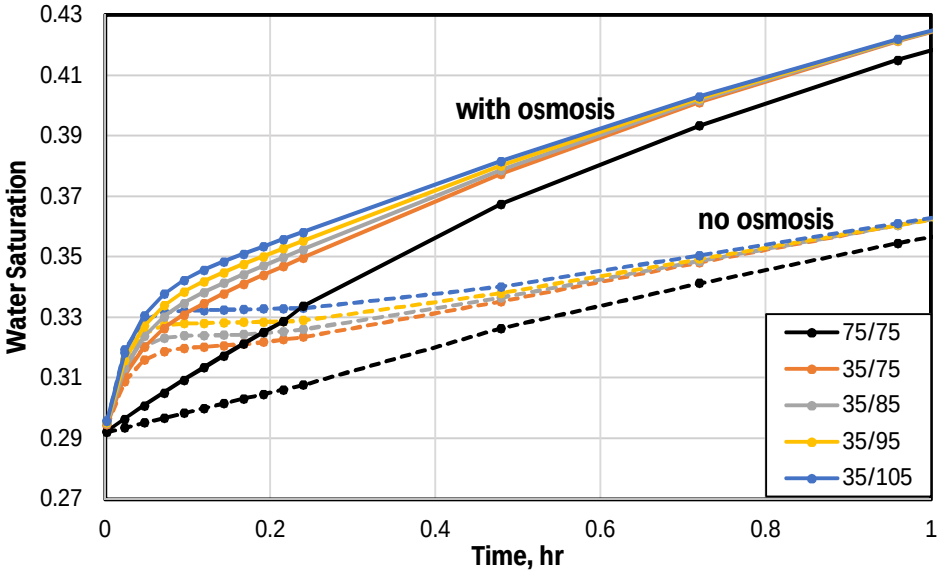

Fig. 29 – Simulation result of the computed water saturation vs time on the first matrix grid block during shut-in period. The dashed lines represent cases without osmosis and the solid lines represent cases with osmosis. Larger temperature imbalances tends to adsorb larger water volume.

Figure 29 shows water saturation condition on the first matrix grid block element. Osmosis causes the water saturation increase because now there are two mechanisms to absorb water; imbibition and osmosis. Furthermore, the plateau region during first half hour on water saturation, which is used formed under non-isothermal condition, also has gone due to osmosis mechanism. The mass exchanges of salt component between clay membrane efficiency cause water saturation increases steadily since the fluid between fracture and formation begins contacting each other. This condition is continued all the time. The larger gap of temperature difference still makes the water saturation rise faster as we discussed in previous study.

The existence of clay pores inside matrix elements increases the value of initial formation capillary pressure as shown in **Figure 30**. The capillary pressure increases around 20% from previous study. The existence of clay pore within matrix elements makes pore throat radius become smaller, which causes capillary pressure higher. The small pore throat also makes the absorption of water volume from fracture through spontaneous imbibition during first half hour shut-in period become faster as shown in **Figure 29**. However, the capillary pressure reduces faster after making a contact with fracture fluid. In the end, the capillary pressure drops at the same point with previous study, which osmosis mechanism is ignored, after 2.4 hour contact with fracture fluid as shown in **Figure 30**.

Interestingly, the chemical concentration has more crucial impact on mean normal stress during simulation in isothermal condition. After 4 minutes shut in, osmosis reduces the impact of temperature imbalance in non-isothermal case but we see no change in isothermal case as shown in **Figure 31**. The mean normal stress reduces in the range of 300 to 700 psi in the presence of osmosis.

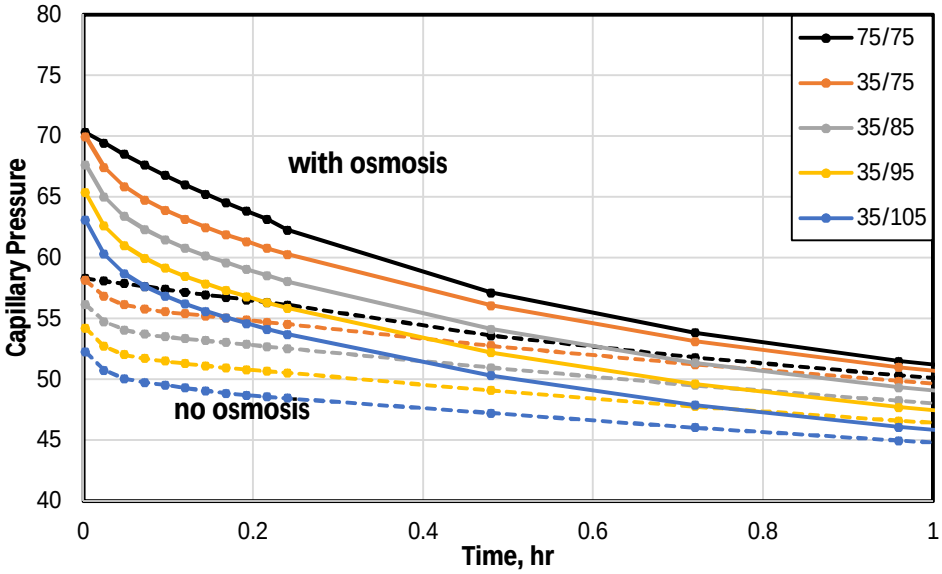

Fig. 30 – Simulation result of capillary pressure vs time on the first matrix grid block during shut-in period. The dashed lines represent cases without osmosis and the solid lines represent cases with osmosis. Clay swelling increases not only the formation capillary pressure but also the decline rate of capillary pressure.

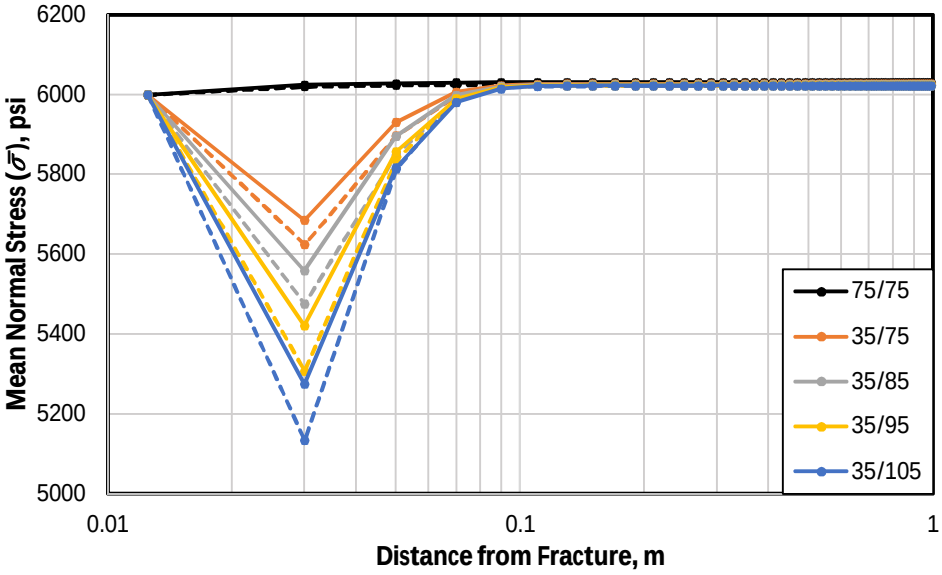

Fig. 31 – Simulation result of mean normal stress profile after 4 minutes shut-in period. The dashed lines represent cases without osmosis and the solid lines represent cases with osmosis. The mean normal stress drops almost one-third because of clay swelling

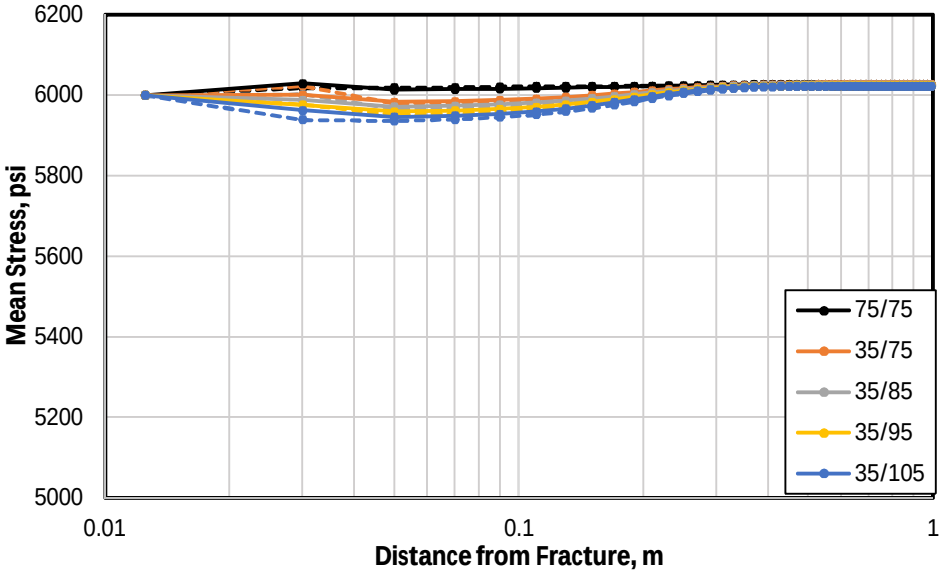

Fig. 32 – Simulation result of mean normal stress profile after 2.4 hours shut-in period. The dashed lines represent cases without osmosis and the solid lines represent cases with osmosis. Clay swelling negates the impact of temperature imbalance.

After 2.4 hours shut-in, osmosis negates the impact of temperature imbalance on the non-isothermal case as shown in **Figure 32**. Meanwhile, the mean normal stress of the first grid block of matrix element near the fracture under isothermal condition drops almost 80%. Previously, the mean normal stress increases drastically into peak position of around 6150 psi at 3 cm away from the fracture when osmosis mechanism is ignored, only reaches around 6030 psi, which make the change become insignificant.

Figure 33 illustrates the osmosis impact on mean normal stress at the first grid block along shut-in period. The mean normal stress increase almost 20% from previous study. We can see here, the mean normal stress stabilizes all the time during isothermal condition. Meanwhile, the impact of temperature gap in non-isothermal condition during ealy time of shut-in is now reduced due to osmosis mechanism. The lowest point of mean normal stress for the case with temperature gap of 70^{o}C (blue line), which drops almost 5100 psi by ignoring osmosis impact, now only drops around 5275 psi.

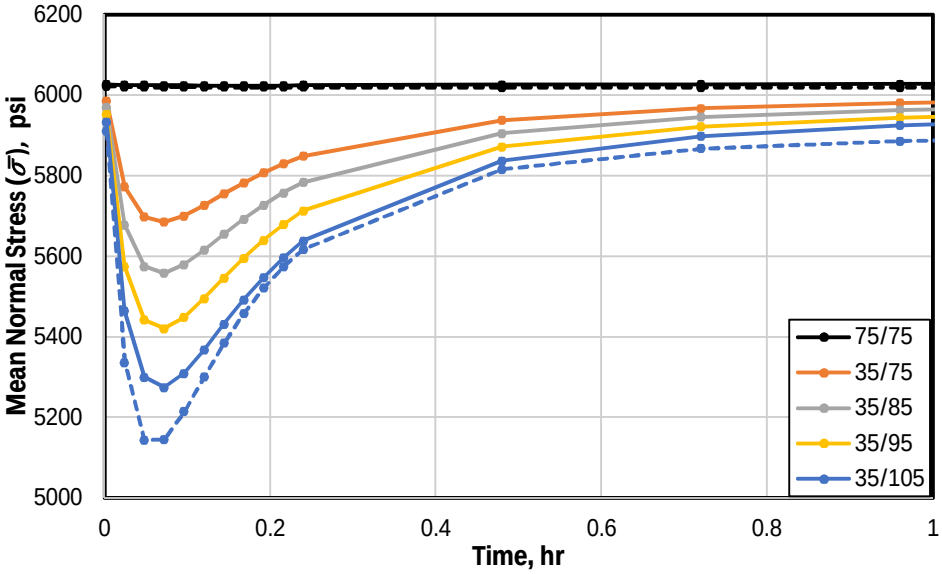

Fig. 33 – Simulation result of mean normal stress vs time on the first matrix grid block during shut-in period. The dashed lines represent cases without osmosis and the solid lines represent cases with osmosis. The mean normal stress become steady during simulation in isothermal condition in time because of clay swelling.

The similar behavior is also observed in permeability reduction profiles as shown in **Figure 34** to **Figure 36**, which are mirroring mean normal stress curves behavior. Clay swelling gives additional stress to confining pressure, thus increases net effect stress and reduces the permeability. Permeability declines almost 20% because of osmosis at the early time of shut-in periods as shown in **Figure 34** and **Figure 36** . The permeability change become insignificant and the impact of temperature gap become unnoticeable after 2.4 hours or when the temperature between formation and the fracture has reached balance as shown in **Figure 35**.

We conclude that the impact of temperature imbalance on formation mean normal stress and permeability change percentage is reduced because of chemical imbalance existence. In addition, the porosity of the formation is reduced by osmosis. However, the impact is insignificant, in the range of 0.2-0.4%.

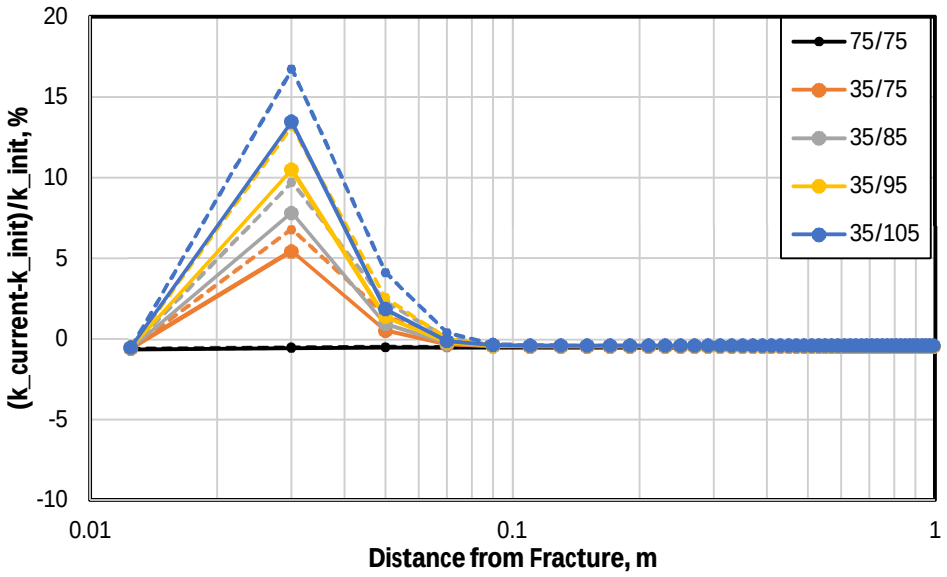

Fig. 34 – Simulation result of permeability reduction profile after 4 minutes shut-in period. The dashed lines represent cases without osmosis and the solid lines represent cases with osmosis. Clay swelling reduces permeability almost 20%.

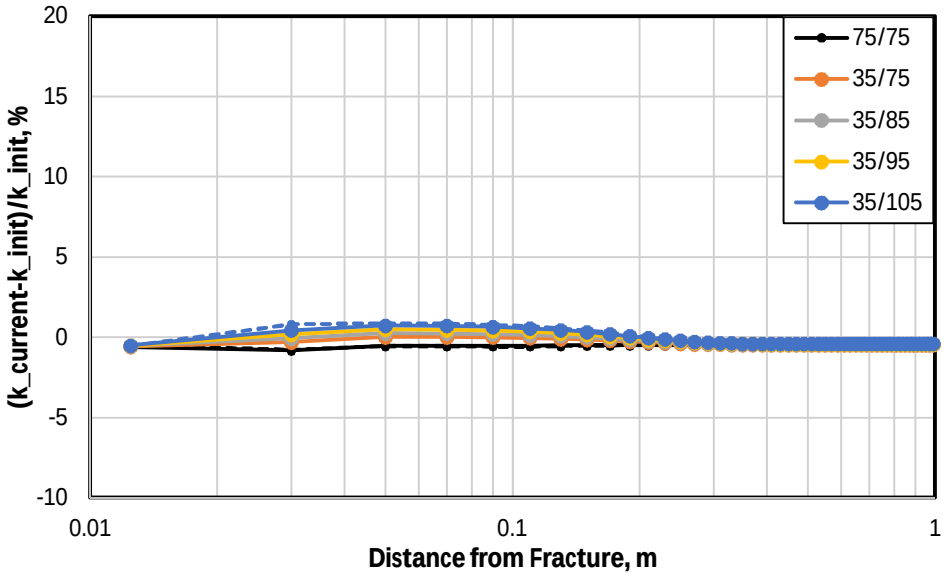

Fig. 35 – Simulation result of permeability reduction profile after 2.4 hour shut-in period. The dashed lines represent cases without osmosis and the solid lines represent cases with osmosis. Clay swelling negates the impact of heat transfer.

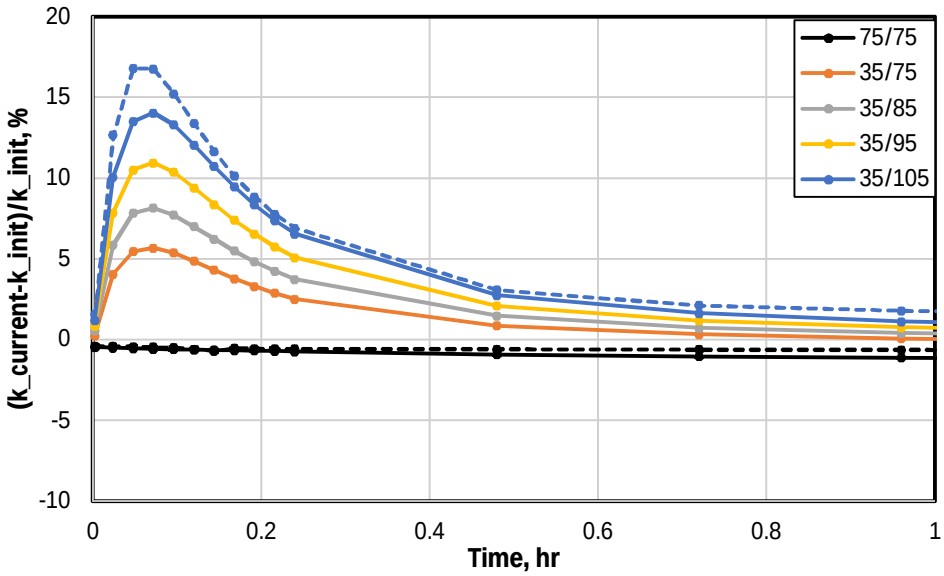

Fig. 36 – Simulation result of permeability reduction vs time on the first matrix grid block during shut-in period. The dashed lines represent cases without osmosis and the solid lines represent cases with osmosis. The permeability become steady during simulation in isothermal condition in time because of clay swelling.

4.4.3. The Impact of Salt Concentration Difference and Rock Thermal Expansion on Chemo-Thermo-Poro-Elastic System

In this section, the investigation of chemo-thermo-poro elastic on shale formation is continued by changing the salt mass fraction in formation from 0.1 into 0.15, while the other parameters are kept the same. The purpose of this sensitivity is to see its impact on shale formation properties with the formation salt concentration. In addition, we want to see what factors within osmosis mechanism that can change the impact on temperature during shut-in period on hydraulic fracturing. As we can see in **Figure 37**, the small increment on salinity gives a significant influence on capillary pressure. Initial capillary pressure in the formation raises into range 70 – 80 psi for varied temperature. Even though bigger salinity tends to increase capillary pressure almost 15%, it does still not give any

significant impact on pressure drop, water saturation, mean normal stress, or permeability reduction.

The last result in this first study shows the sensitivity of rock thermal expansion (β_t) for simulation during shut-in period under non-isothermal condition. For this sensitivity, the simulation of the largest temperature difference is considered under three different rock thermal expansion values which are 0, 10^{-6}, and 10^{-5} $^{o}C^{-1}$. **Figure 38** shows that increasing rock thermal expansion tends to reduce formation permeability up to 10%. However, when the heating process of the cold fluid region at the early time occurs, the permeability only drops up to 1.6% from the base case result, when the rock thermal expansion is assumed to be zero.

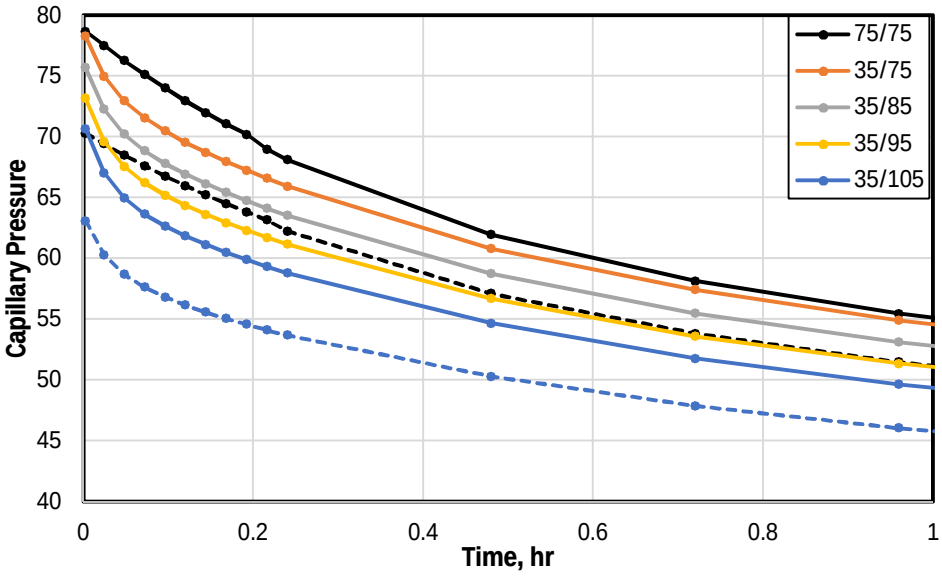

Fig. 37 – Simulation result of capillary pressure vs time on the first matrix grid block during shut-in period. The dashed lines represent cases with 10% salinity and the solid lines represent cases with 15% salinity. The small increment on salinity increases capillary pressure almost 15%.

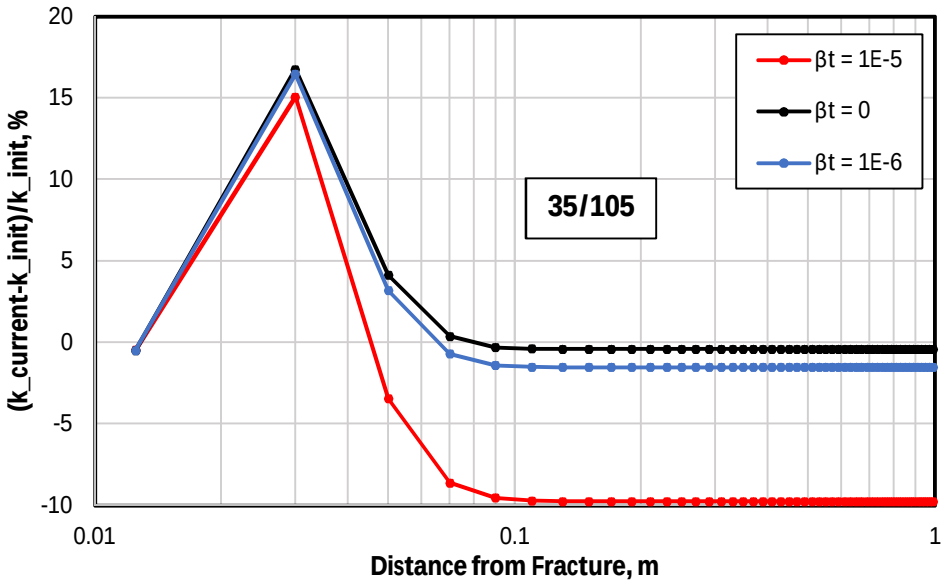

Fig. 38 – Simulation result of permeability profile for non-isothermal case with formation temperature of 105ºC after 4 minutes shut-in. Increasing rock thermal expansion tends to reduce permeability up to 10%.

5. NEAR FRACTURE CAPILLARY END EFFECT ON SHALE GAS AND WATER PRODUCTION*

This chapter discusses the importance of CEE during the flow-back and production. The objective of this modeling effort is to investigate the role of CEE on shale gas production and its impact on shale gas performance. Another objective of this study is to observe several parameters, which affect CEE, so that I can find the solution to reduce or minimize the CEE during shale gas production. In addition, the damage caused by CEE also will be investigated and compared with the damage resulted from stress effect.

The chapter is organized as follows. First, the numerical simulation of new simulator including CEE correction is introduced. The CEE correction following Huang and Honarpour approach is described in **Chapter 2**. Next, the reservoir parameters used for the investigation are introduced and a forward simulation study is performed predicting a one-month well shut-in (or shut-in) period followed by two-months of production. The production simulations are performed at constant fracture pressure at two separate -high and low- fracture pressure values. The produced gas and water rates are investigated near the fracture-matrix interface as a function of the distance to the fracture and as a function of shut-in and production times. The predicted non-linearity in water and gas flow rates near the fracture are analyzed in the presence of CEE and compared to the case in the absence of the effect. In the next part of the study, the impact of the stress change on the micro-fracture network permeability is introduced into the simulation model in order to compare the impairment to that caused by CEE.

---

* Part of this chapter is reprinted with permission: "Near Fracture Capillary End Effect on Shale Gas and Water Production" by Elputranto, R., & Akkutlu, I. Y., 2017. In *Unconventional Resources Technology Conference, Houston, Texas, 23-25 July 2018* (pp. 756-769). Society of Exploration Geophysicists, American Association of Petroleum Geologists, Society of Petroleum Engineers., whose permission is required for further use.

5.1. Numerical Simulation Model

The simulation model for this study is based on mass balances for the two-phase (gas-water) flow problem, which has been modified to include CEE. The mathematical model of mass balance, numerical solution, and discretization method in this chapter have been described in **Chapter 3**.

There are three thermo-physical states establish in the matrix and fracture domain during simulation. The states are the aqueous single-phase, the gaseous single-phase, and the aqueous-gaseous two-phase in matrix domain and the aqueous-gaseous two-phase in fracture domain. Each domain and each state consist of six primary variables (X_i) as the unknown to solve six residual equations. These primary variables are described in **Table 12**.

Table 12 – Primary Variables and States in Multi-Porosity Shale Gas Reservoir System

Primary Variable (X_i)	State
$P_A, y_A^{CH_4}, y_A^{Salt}, y_{A,Clay}^{Salt}, P_{Clay}, T$	Aqueous single-phase
$P_A, y_G^{CH_4}, y_{A,Clay}^{Salt}, y_{A,Clay}^{H_2O}, P_{Clay}, T$	Gaseous single-phase
$P_A, S_G, y_A^{Salt}, y_{A,Clay}^{Salt}, P_{Clay}, T$	Aqueous-gaseous two-phase

The subscript $Clay$ following parameter molar fraction ($y_{A,Clay}^{Salt}; y_{A,Clay}^{H_2O}$) and pressure ($P_{Clay}$) in **Table 12**, represents that the variables are simulated in the clay pore. Other unknown variables are solved by using constitutive, equilibrium restriction, and constraint equations which has been explained in previous **Chapter 3**.

The relative permeability and capillary pressure equation on tight formation is not well-establish yet. However, some measurement principle in conventional reservoir can be adapted into unconventional reservoir. Corey function is used on tight formation by fitting the Corey exponent as suggested by previous investigators (Dacy, 2010; Honarpour et al., 2012). In this simulation model, the relative permeability and capillary pressure can be represented by Standing (1975) correlation, which includes further modifications to model by Brooks and Corey (1964):

$$k_{rg}\big]_{imbibition} = k_{rg}\big|_{S_{iw}} \left(S^*_{gF}\right)^2 \left[1 - \left(1 - S^*_{gF}\right)^{\left(\frac{2}{\lambda}\right)+1}\right] \quad (108)$$

$$k_{rg}\big]_{drainage} = k_{rg}\big|_{S_{iw}} (1 - S^*_w)^2 \left[1 - (S^*_w)^{\left(\frac{2}{\lambda}\right)+1}\right] \quad (109)$$

$$k_{rw} = k_{rw}\big|_{S_{gr}} (S^*_w)^{\left(\frac{2}{\lambda}\right)+3} \quad (110)$$

$$P_c\big]_{imbibition} = P_d \left(1 - S^*_{gF}\right)^{-\left(\frac{1}{\lambda}\right)} \quad (111)$$

$$P_c\big]_{drainage} = P_d (S^*_w)^{-\left(\frac{1}{\lambda}\right)} \quad (112)$$

where k_{rg} is relative permeability of gas, k_{rw} is relative permeability of water, P_d is the displacement pressure (also called "threshold pressure"), and the subscript S_{iw} and S_{gr} represent the value of relative permeability at interstitial water saturation and

at residual gas saturation. S_w^* can be defined as normalized water saturation based on the mobile saturation range, $1 - S_{iw} - S_{gr}$, while S_{gF}^* is normalized "free" (mobile) gas saturation. Both S_w^* and S_{gF}^* can be expressed as:

$$S_w^* = \frac{S_w - S_{iw}}{1 - S_{iw} - S_{gr}} \quad (113)$$

$$S_{gF}^* = \frac{1}{2}\left[\left(S_g^* - S_{gr}^*\right) + \sqrt{\left(S_g^* - S_{gr}^*\right)^2 + \frac{4}{C}\left(S_g^* - S_{gr}^*\right)}\right] \quad (114)$$

Here S_g^* and S_{gr}^* are defined as normalized gas saturation and normalized residual gas saturation, which can be expressed as:

$$S_g^* = \frac{S_g - S_{gr}}{1 - S_{iw} - S_{gr}} \quad (115)$$

$$S_{gr}^* = \frac{S_{gi}^*}{CS_{gi}^* + 1} \quad (116)$$

Here, S_{gi}^* is normalized initial gas saturation and C is the "trapping constant" of the rock determined in the laboratory. In the absence of laboratory results, C's value is taken in between 1 and 3 based on the previous water flooding studies (Standing, 1975). In Equations (108) – (112), λ is the pore-size distribution index as known as Corey's exponent. It takes smaller value for a formation with a wide range of pore size and larger

values for a relatively uniform pore size media (Brooks and Corey, 1964). During the drainage process under influence of CEE, this parameter as well as the interstitial water saturation distribution will be predicted as a function of distance from fracture using the approach of Huang and Honarpour (1998) based on their core flood experiments.

We used the same derivation steps to expand the range of Corey's exponent in Huang and Honarpour model so that the approach method not only cover conventional reservoir but also tight gas and shale formation. However, the Corey's exponent on this model is limited in the range of 0.7 – 3.1. Huang and Honarpour method is introduced into the flow simulation model of this study by introducing the input data of relative permeability and interstitial water saturation into the charts given in **Figure 14** and **Figure 15**.

The CEE model requires that the exact same value of λ and the pressure drop ratio from both charts will be predicted iteratively. These values are then applied in Equation (113) – (118) so that, the distribution of the interstitial water saturation (S_{iw}) can be calculated as a function of the distance x, from inlet to the outer boundary of the model using another iteration process as shown in **Figure 13** (bottom).

$$\frac{L-x}{L} = \frac{P_d}{|\Delta P_L|}\left\{(S_w^*)^{-\frac{1}{\lambda}} - \frac{2\lambda^2(\lambda+2)(6\lambda^2+\lambda+1)}{(\lambda^2-1)(4\lambda^2-1)(3\lambda+1)} + \frac{2(S_w^*)^{1-\frac{1}{\lambda}}}{\lambda+1} - \frac{(S_w^*)^{2-\frac{1}{\lambda}}}{2\lambda+1} + \frac{(S_w^*)^{1+\frac{1}{\lambda}}}{\lambda+1} - \frac{2(S_w^*)^{2+\frac{1}{\lambda}}}{2\lambda+1} + \frac{(S_w^*)^{3+\frac{1}{\lambda}}}{3\lambda+1}\right\} \quad (117)$$

$$\frac{P_d}{|\Delta P_L|} = \frac{k\bar{k}_{rg}\big|_{\bar{S}_{iw}} AP_d}{Lq_g\mu_g} \quad (118)$$

In equations above, ΔP_L is the pressure drop of entire grid block, k is absolute permeability, L is the total length of the grid block from fracture to outer boundary and $L - x$ is the distance from fracture to the center of the measured grid block for which the saturation is computed. Lastly, this corrected interstitial water saturation profile along with corrected λ value are used to calculate the relative permeability and capillary pressure curves for the flow simulation. This process is executed in every grid block at a given time step. The major steps of this calculation are shown in **Figure 39**.

5.2. Validation of the Numerical Model with the Experiment

The numerical simulation with CEE is validated by comparing with a core flooding experiment published by Huang and Honarpour (1998). The experiment was conducted using oil/water displacement in a carbonate core, which possesses water-wet characteristics at reservoir temperature.

The experiment began by conducting an oil flooding to the core, which initially has a certain residual gas saturation. By performing this constant rate injection, the averaged interstitial water saturation and the averaged terminal oil relative permeability in the presence of capillary end effect is measured at the end of oil flood. The experiment is continued by placing a water-wet porous plate at the core outlet end. The injection method is changed from constant rate into contact pressure so that the water saturation profile during oil flooding become uniform and the true interstitial water saturation can be measured. In the last steps of the experiment, the porous plate is removed and the injection is changed back to constant rate injection so that the true terminal oil relative permeability without the presence of capillary end effect can be determined.

To simulate the problem in the presence of CEE, I used 11 elements attributed as carbonate core. The parameters information used in core flooding experiment is described in **Table 13.** The simulation is run by applying a closed boundary with no-flow in the inner boundary wall and a constant rate in the outer boundary wall. The comparison between values from simulation results and experiment data is shown in **Figure 40.**

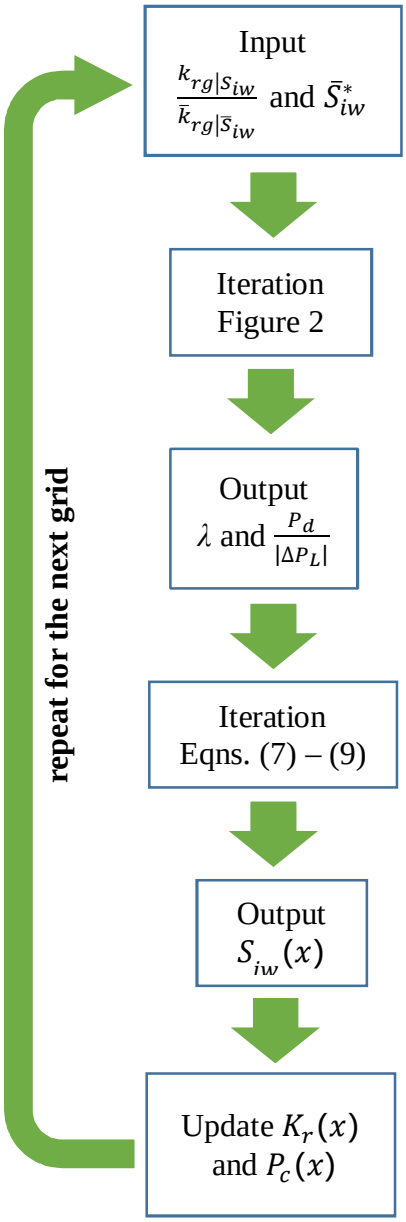

Fig. 39 – Flowchart of interstitial water saturation distribution calculation.

Table 13 – Parameters used in the Simulation of the Core Flooding Experiment (Adopted from Huang and Honarpour, 1998)

Parameter	Value	Unit
Core length	10	cm
Core diameter	1.83	cm
Initial temperature	150	°F
Permeability	5	md
Porosity	22.5	%
Rate	1.39E-04	cm^2/s

Parameter	Value	Unit
Viscosity	6	cp
S_{or}	0.251	
S_{iw}	0.292	
$\bar{k}_{ro}$	0.65	
$\bar{S}_{iw}$	0.324	
k_{ro}	0.51	

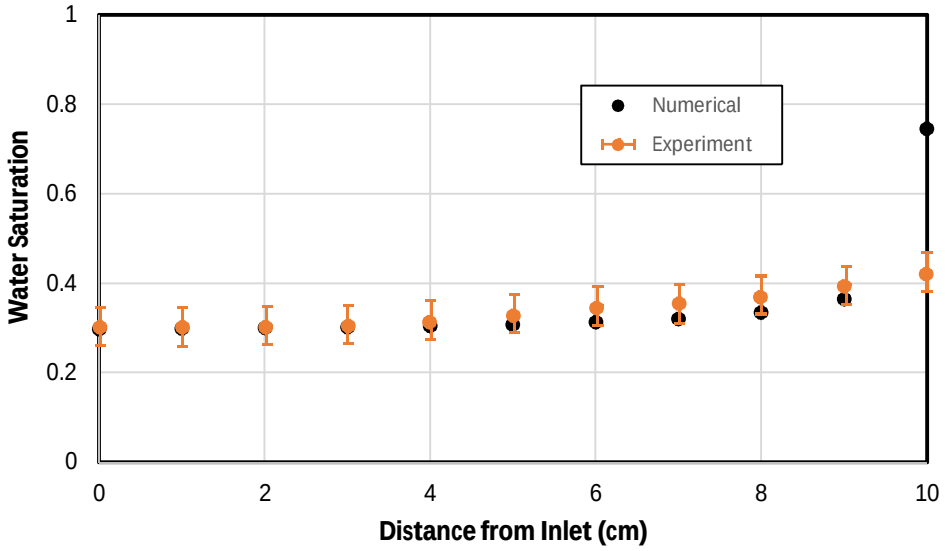

Fig. 40 – Comparison of the simulation results with the core flooding experiment data, from Huang and Honarpour (1998). The experimental data is the solid red dot and the numerical simulation results are shown as the black circles.

5.3. Initial, Boundary Conditions and Reservoir Parameters

Initially a multi-scale triple porosity model was developed including gas desorption effect in the kerogen pores and osmosis effect in the clay pores. However, using a separate simulation study, it was previously found that the impact of CEE is much stronger than the gas desorption and osmosis effects. We therefore ignore these effects during CEE study in this chapter and present a uni-pore model. The reader interested in the multi-scale treatment of the problem can refer to Eveline et al. (2017).

Also, for further simplicity in the analysis of the invasion of the fresh slick water from fracture into the formation during hydraulic fracturing operation as shown in **Figure 3**, we considered a one-dimensional reservoir flow simulation model in this study to represent a quarter of a single vertical hydraulic fracture perpendicular to a horizontal well and the adjacent stimulated shale gas volume. The model has length of 2m on x-direction, which is divided into 200 grid blocks with the first grid block on the left considered as the fracture element as illustrated in **Figure 13**. The input parameters for the matrix elements used in the simulation study are presented in **Table 14**. Recent studies estimated λ values for shales in a range of 0.2 – 7.54 (Donnelly, 2015; Donnelly et al., 2016). In this study, λ value of 2 as used in simple Brooks-Corey correlation is used in the absent of CEE condition.

At initial time, the water saturation of the matrix grid blocks is assumed to be at 29% irreducible water saturation with maximum capillary pressure value, while the fracture element, which has quite large permeability compare to other grid blocks, is assumed to hold 100% fracturing water. Initially, there is no capillary pressure within the fracture because only water exists. In order to investigate the impact of capillary discontinuity at near the fracture, the profiles of interstitial water saturation, gas relative permeability at interstitial water saturation, and capillary pressure used in this simulation are generated using Huang and Honarpour (1998) approach.

Table 14 – Input Matrix Parameters and Their Base Values for the Simulation Study

Parameter	Value	Unit
Initial pore pressure	3000	psi
Initial temperature	60	Celsius
Permeability	220	nD
Porosity	18	percent
k_{rw} at S_{gr}		
- Strong Water Wet Rock	0.06	fraction
- Less water Wet Rock	0.5	fraction
k_{rg} at S_{iw}	0.65	fraction
Grid System	2m x 100m x 10m (200 x 1 x 1)	

Parameter	Value	Unit
S_{iw}	29	percent
λ	2.0	

Crack Permeability Model Parameters

k_0	0.01	mD
m	0.5	
P_1	26000	psi
P_{conf}	15000	psi
α	0.5	

The pressure is initially uniform and equal to 3,000 psi in all the elements. A constant pressure of 3,000 psi is maintained at the fracture element for 30 days to simulate the shut-in period after the hydraulic fracturing treatment. This period is followed by the production period. The two-phase flow develops along the x-direction perpendicular to the fracture during the production. We considered two separate rock models with different water relative permeability curves, which are still in the range of water-wet rock characteristic, for the simulation study to show the capillary end effect with varying levels of wettability. These relative permeability and the capillary pressure models curve, which are used in simulation study, are shown in **Figure 41** and **Figure 42.** Here, the gas relative permeability and the capillary pressure curves of the models are divided into drainage and imbibition curves as explained in Equations (108) – (112). The imbibition curve is applied during shut-in period or when the water flow to the formation. On the other hand, the drainage curve is applied during production period or when the water is produced to the fracture element.

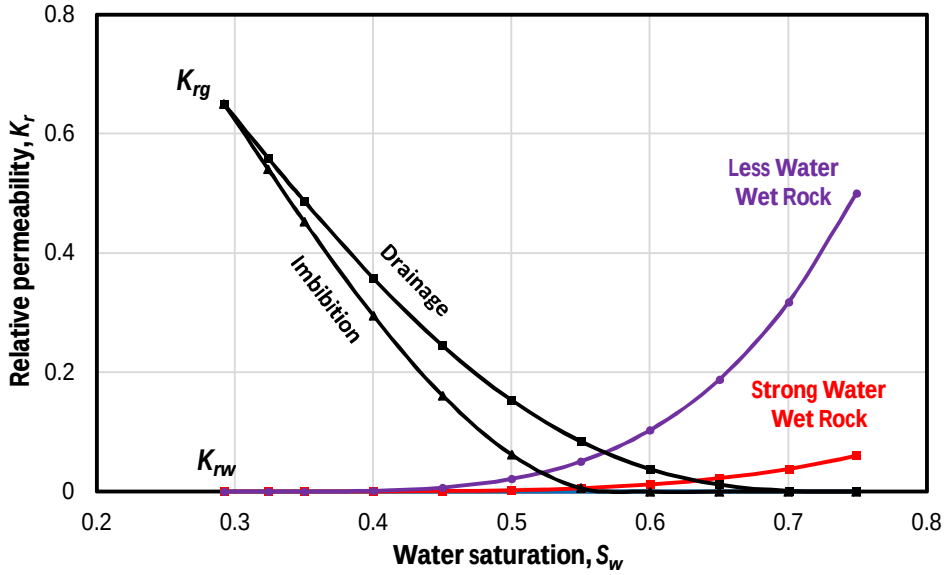

Fig. 41 – Tight gas and shale formation gas-water relative permeability used in the simulation study. Drainage curve is used during production period, while imbibition curve is used during shut-in period.

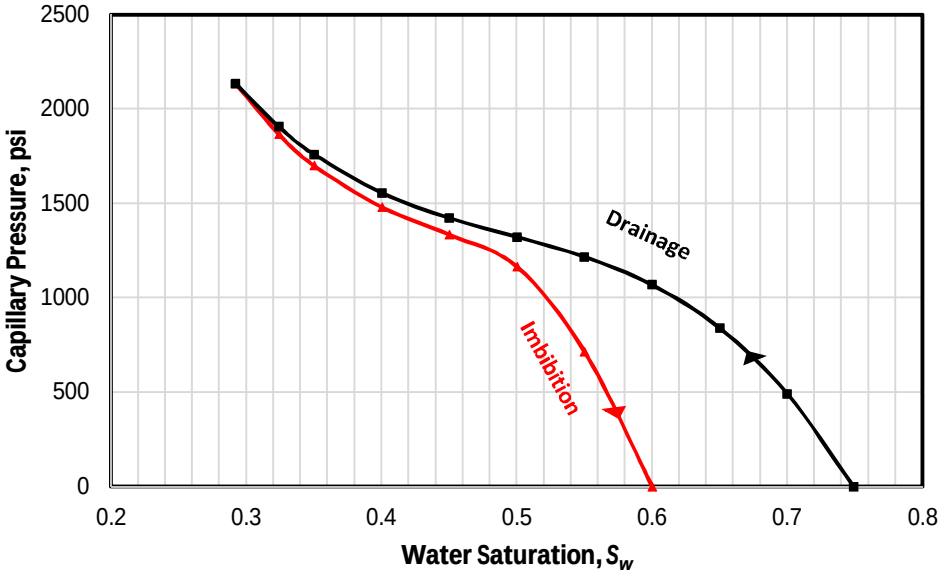

Fig. 42 – Tight gas and shale formation capillary pressure used in the simulation study. Drainage curve is used during production period, while imbibition curve is used during shut-in period.

5.4. Simulation Results and Discussion

Simulation study is performed for two separate operations in the field: (i) the well shut-in (or shut-in) period after the fracturing, followed by (ii) the water flow-back and gas production, or briefly the production period. The shut-in period was necessary in our study only because it allows us to distribute fracturing water into the formation in the presence of two-phase flow dynamics. Following 30 days of shut-in, with its non-uniform saturations in the formation, the model is used to simulate the production period at constant flowing pressure. During the production the fracture cell on the left is kept at constant pressure at two separate pressure values in order to see the impact of pressure drawdown on CEE. First, the fracture pressure is kept at 2,500 psi to represent the production in low pressure drawdown case and, in the second part, the fracture pressure is kept at 500 psi to represent the production at high pressure drawdown.

5.4.1. The Impact of CEE on Reservoir Properties

Simulation results show that CEE changes the drainage characteristics of gas relative permeability near the fracture, **Figure 43**. The interstitial water saturation becomes higher closer to the fracture, while both gas and water become less immobile. The water saturation profiles corresponding to shut-in and production periods are shown in **Figure 44** and **Figure 45**. CEE has yet to occur during the shut-in period. However, simulation results show that the fresh fracturing water invades shale matrix during shut-in period and creates a fluid invasion region as shown in **Figure 3**. In this region, a high water saturation region, rather a saturation wave, develops near the matrix-fracture interface due to spontaneous imbibition caused by high capillary pressure in the formation. The saturation wave penetrates into the formation and propagates towards the outer boundary. Note that this is a relatively slow process due to tight nature of the formation; the leading edge of the saturation wave has reached 3 – 4 cm into the formation after 30 days of shut-in period.

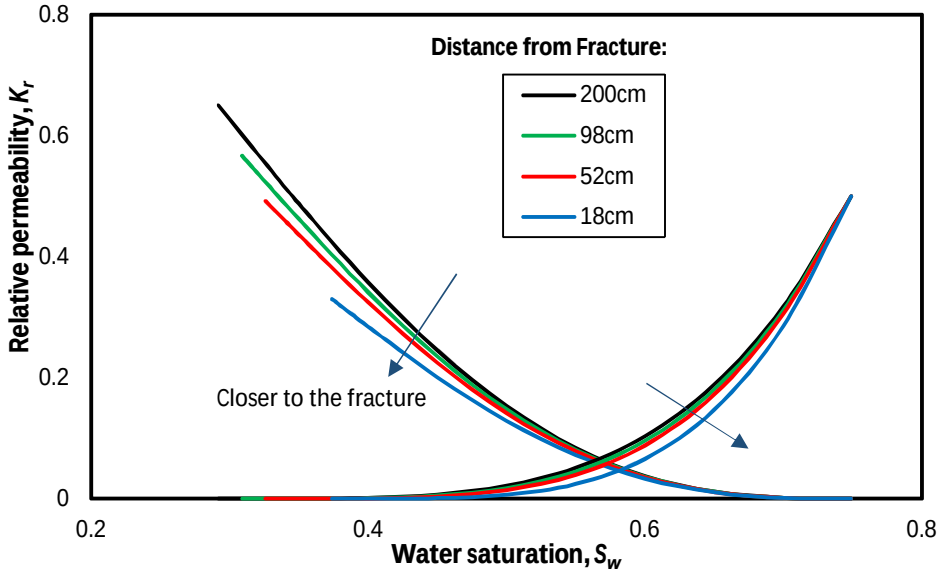

Fig. 43 – The computed gas-water relative permeability during production period. Simulation results with CEE show changes in the drainage curve such that, as the fracture is approached, S_{iw} increases, and both water and gas become less mobile.

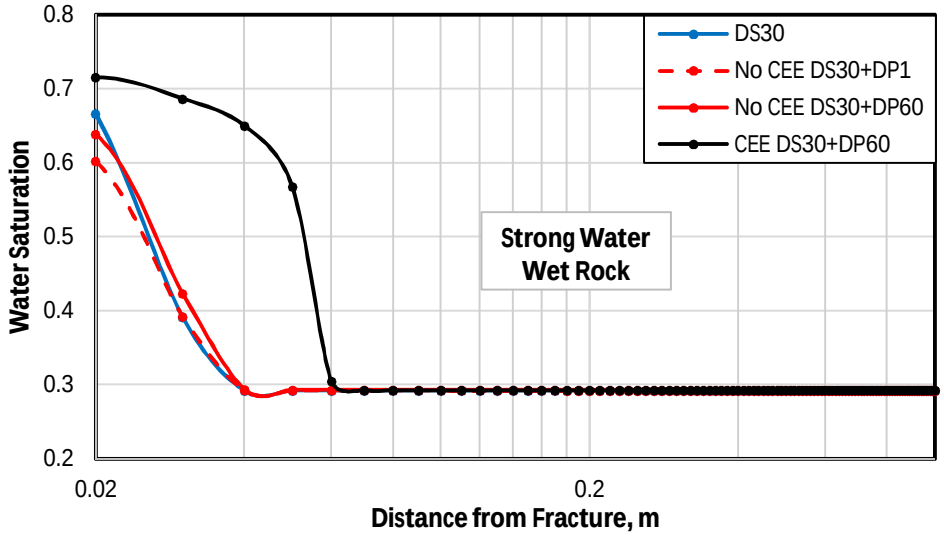

Fig. 44 – The predicted water saturation profile of strong water wet rock case during 30 days of the shut-in (DS30) and additional 1 and 60 days of production (DP1 and DP60) periods. The production runs without CEE (red) and with CEE (black). Note that CEE increases water saturation in the vicinity of the fracture. The fracture pressure is kept at 2,500 psi during the production to represent a relatively low-pressure drawdown.

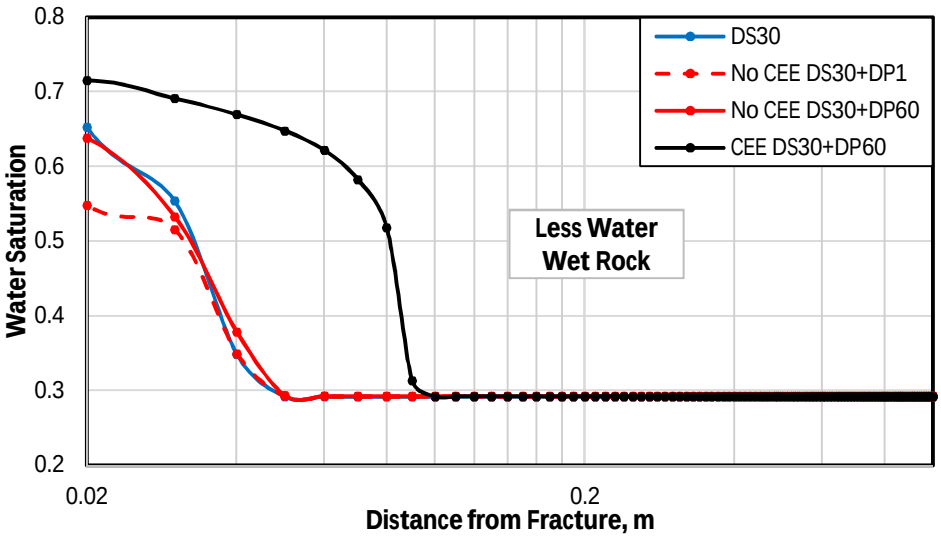

Fig. 45 – The predicted water saturation profile of less water wet rock case during 30 days of the shut-in (DS30) and additional 1 and 60 days of production (DP1 and DP60) periods. The production runs without CEE (red) and with CEE (black). Note that CEE increases water saturation in the vicinity of the fracture. The fracture pressure is kept at 2,500 psi during the production to represent a relatively low-pressure drawdown.

During the flow-back, in the absence of CEE as shown by the red line in **Figure 44**, this large volume of water is allowed to flow back into the fracture. The instantaneous pressure drop at the fracture element causes the pressure force to overcome capillary force during the production, as shown by the red line in **Figure 47**. As a result, water saturation near the fracture drops immediately, while reservoir is producing in the absence of CEE. After 60 days of production, the pressure has dropped in all elements. This condition bring back the capillary forces to take control over the imposed pressure gradient due to low pressure drawdown left in the flow system; consequently, the water continues to imbibe into the matrix during the production.

However, we notice that in the presence of CEE as shown by the black line in **Figure 44**, this large volume of water resists to flow back and creates a high water saturation region in between the fracture and the flowing gas. The interstitial water

saturation build up toward the fracture. The water now hardly moves near the matrix-fracture interface, accumulates. The water level in the saturation wave tends to stay higher during the production period due to this immobile water saturation build up. Note that the capillary pressure has increased dramatically at the leading edge of the saturation wave. As a result, the capillary forces still repress the pressure forces effectively when compared to the case in the absence of CEE. Consequently, the injected water does not move to the fracture due to pressure drop during flow back, instead it continues to imbibe deeper into the formation. Additionally, the capillary force keeps drawing the water volume in the fracture into the formation. Note that right after the shut-in and before the production begin, the fracture element still contain 100% fracturing water. This leads to increase in the water saturation near the fracture. After 60 days of production, the boundary layer has reached 4 cm into the formation. In the case of less water wet rock as shown in **Figure 45**, the water propagation become deeper since the water now can move more easily. The boundary layer in this case has reached 5.5 cm from the fracture after 60 days of production. In summary, the simulation results show that CEE increases the water invasion and the water saturation builds up in the vicinity of the fracture during the production.

Figure 46 shows the predicted gas relative permeability values at the interstitial water saturation near the fracture. Clearly, CEE decreases the gas relative permeability – hence, mobility- in the vicinity of the fracture even though the change in relative permeability curve has limited influence on the CEE. **Figure 47** shows that water pressure in the formation is maintained high during production in the presence of CEE. This reflects on reduction on well productivity (Christiansen, 2005).

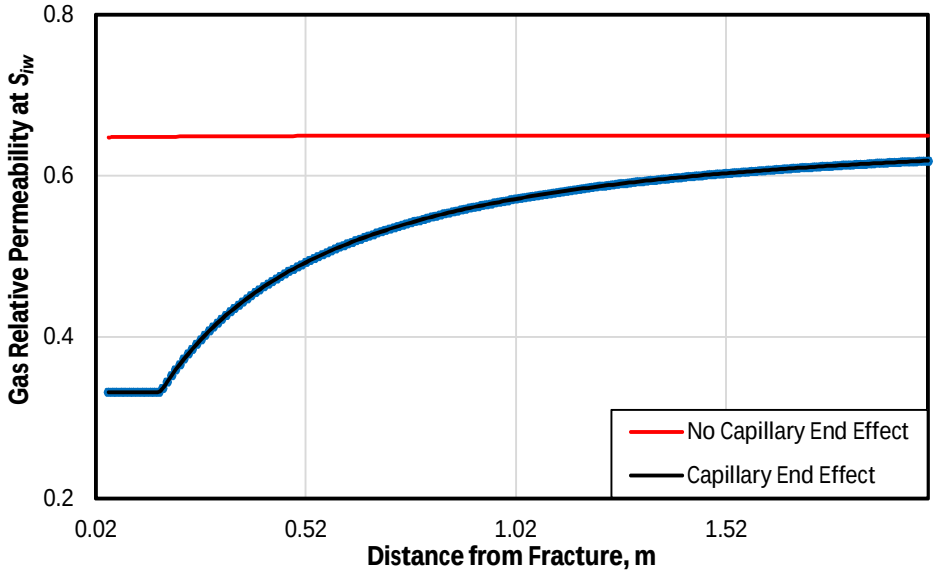

Fig. 46 – Predicted gas relative permeability at interstitial water saturation resulted from numerical simulation. CEE decreases gas relative permeability in the vicinity of the fracture.

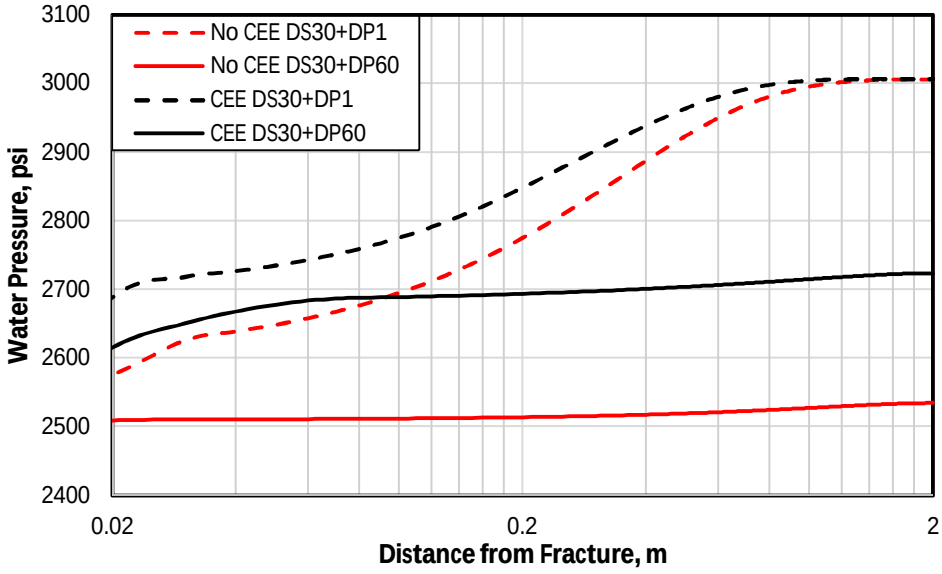

Fig. 47 – Predicted aqueous phase pressure in formation profile resulted from numerical simulation. CEE decreases gas relative permeability in the vicinity of the fracture.

5.4.2. The Impact of CEE on Production Rates

Next, the water and gas flow rates of the simulation are analyzed. We analyzed the rates due to flow in between the fracture element and the first matrix cell. The positive flow rate indicates the fluid movement from formation to the fracture. While negative flow rate indicates the flow into the matrix. During the simulation of the shut-in period, at time equal to zero, the pressure in the fracture and in the formation is the same and equal to 3,000psi. However, as soon as the fracture fluid contacts the nearby matrix element, the matrix cell near the fracture absorbs fresh water from the fracture as shown in **Figure 48**. This process, which is identified with a negative water rate, is the spontaneous imbibition and it occurs due to capillary pressure in the matrix.

The simulation of the production period is performed using the pressure and saturation distributions computed during the shut-in. The simulation of water flow-back and gas production involves the correction due to the presence of CEE. This correction is done dynamically during the simulation. For the low-pressure drawdown case, there exists a 500 psi force that drives the fluids from the formation into the fracture. Clearly, in the absence of CEE, the fracture produces some of the invaded water back due to the pressure drop (see the dashed lines showing positive water flow rates in water rate profile shown by **Figure 49**). This is consistent with the recent results by Eveline et al. (2017). More water flows back, if the formation is less water wet as shown by the black dashed line. As we can see at the water rate vs time graph in **Figure 48**, the water flow rate is high during the first few days of production. However, once the pressure between the fracture and the adjacent formation cell becomes uniform and equal to 2500psi, in about two months, the flow-back and production of water becomes somewhat more difficult because the imposed pressure drop has dissipated into the formation. Instead, now the local capillary forces dominate and the water continues invading the formation due to imbibition. This leads to further increase in water saturation during production, shown as the black line in **Figure 44** and **Figure 45**. Note that this is the behavior in the absence of CEE.

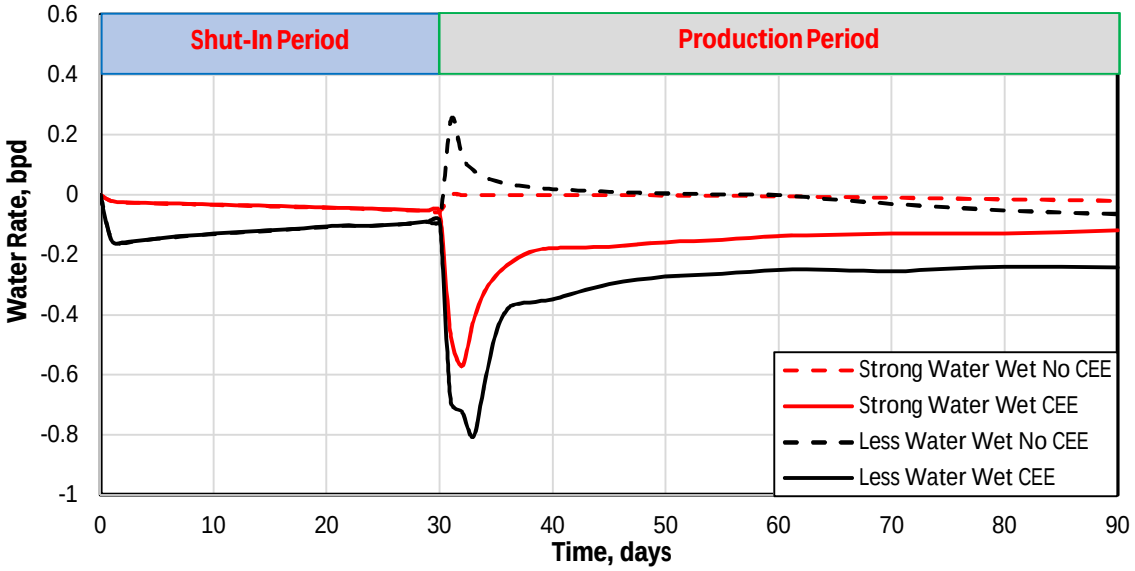

Fig. 48 – Simulation results of water rate at the second matrix element adjacent to the fracture during 30 days shut-in followed by low-pressure drawdown production. The simulation runs without CEE (dash line) and with CEE (solid line).

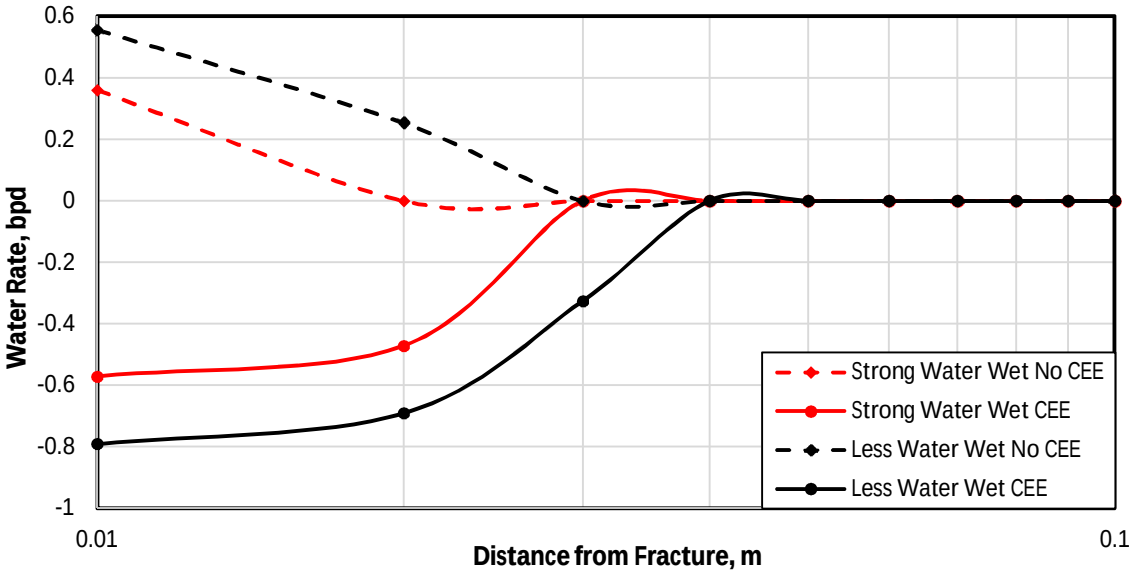

Fig. 49 – Simulation results of water rate after two days low-pressure drawdown production. The simulation runs without CEE (dash line) and with CEE (solid line).

When the CEE is included, shown as the solid lines in **Figure 48**, the simulation model predicts no flowing back of water. Instead, we observe amplified imbibition rates during the first week of the flow back and the water keeps invading the formation along the production time. Only gas flows but, as shown later in **Figure 50** and **Figure 51**, it flows at reduced rates. During the production, CEE becomes dominant, when water leaves the formation and enters the fracture where there is no capillary pressure. This capillary discontinuity at the interface tends to increase the interstitial water saturation at the adjacent element and causes resistance of water to leave the formation. The water accumulates at the boundary and creates water block. Note that the capillary pressure near the boundary is reduced due to the increase in water saturation. Consequently, as the pressure dissipates and the drawdown no longer exceeds the capillary pressure gradient, the water resume the invasion to the formation. As previously discussed from water saturation profile in **Figure 44** and **Figure 45**, the high-water saturation wave continues to propagate into the formation. However, **Figure 49** shows that CEE impact region to the formation is limited. In the strong water wet case, the impact of CEE reached 3 cm from the fracture, while the less water wet case has further distance since the water now can move more freely. Note that the simulation results in **Figure 48** show CEE is time dependent and disappears over time. We predict it takes nearly two months of production time for the CEE to be reduced to zero. This is also the time frame for the pressure depletion of the reservoir system we modeled.

Next, the gas flow rate is analyzed during the production period in **Figure 50.** When CEE is ignored, because a mobile water exists near the fracture, we produce water from the fracture. Due to the water production, the gas saturation near the fracture increases up to 20% higher from its residual value, which in turn leads to production of larger volumes of gas during the first two months of production. After two months, the capillary forces take over the pressure drawdown forces and water begins to imbibe into the formation. This reduces the local gas saturation.

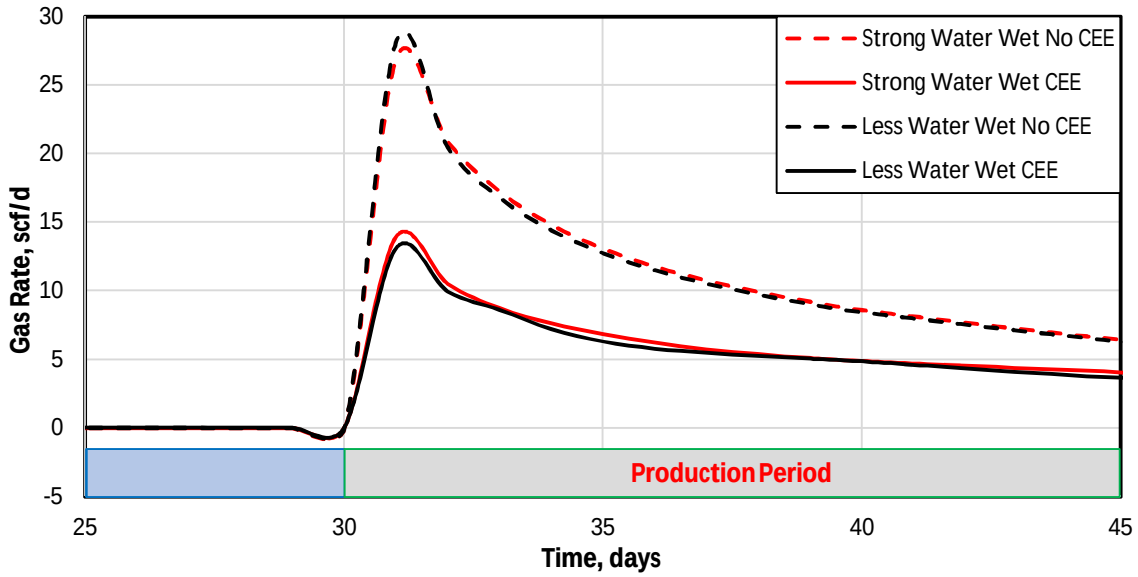

Fig. 50 – Simulation results of gas rate during low-pressure drawdown production. The simulation runs without CEE (dash line) and with CEE (solid line).

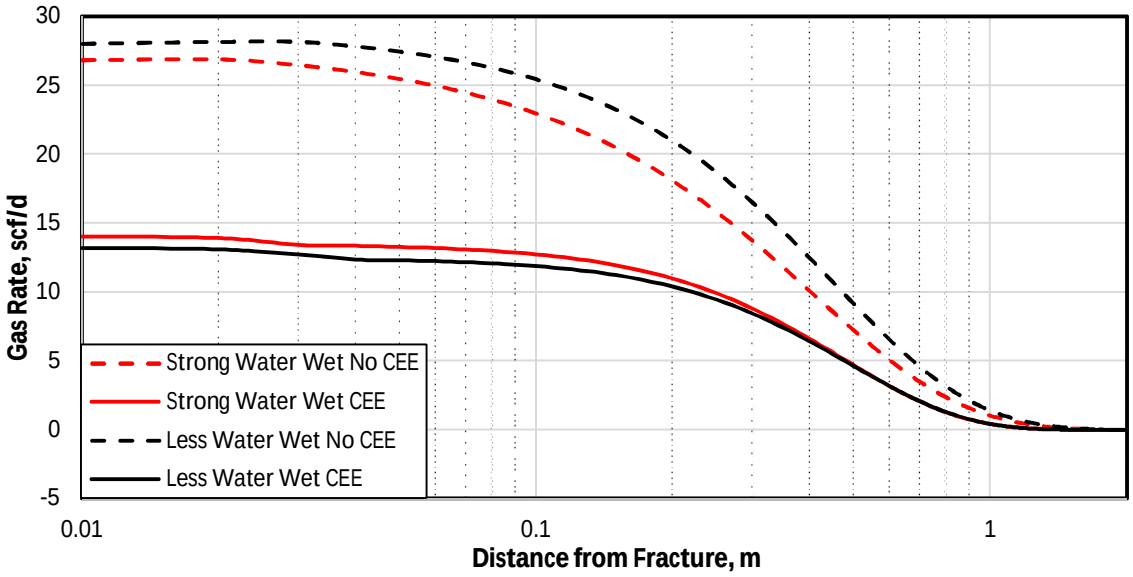

Fig. 51 – Simulation results of gas rate after two days low-pressure drawdown. The simulation runs without CEE (dash line) and with CEE (solid line).

Clearly, significant reduction (nearly 50%) in gas production is observed as a consequence of the hydraulic damage established due to CEE, see solid lines in **Figure 50** and **Figure 51**. Remember that, in this case, a significantly larger volume of water is trapped in the formation near the fracture during the production period. This trapped water tends to decrease the gas productivity in two distinct ways. First, CEE maintains the pressure high and, hence reduces the pressure drop as shown in **Figure 47**, which decreases the productivity. Second, the trapped water can block the flow of gas from the deeper formation by reducing the gas relative permeability. Water saturation build up near the fracture caused by CEE now forces the gas saturation to further drop to values closer to the residual gas saturation.

The gas saturation near the fracture for both rock types is now only around 7% higher from its residual value, or almost one third, compared to the gas saturation from the case without CEE. This results in significant loss in gas production. The gas production rate is reduced nearly by half when CEE is considered. However, the reduction is nearly same for both rock types. This mean the production of gas depends only on the level of the local gas saturation near the fracture, rather than the water mobility. This behavior is different than the case in the absence of the CEE, when the less water-wet rock has a tendency to produce more gas as shown in **Figure 51**.

Figure 51 shows the predicted gas flow rates near the fracture in the formation as a function of distance from the fracture after two days of production. We observe that the pressure transient reaches to about 1.5m distance in the formation in two days. Without CEE, some additional gas production is experienced when the affinity of the formation to water is reduced. Based on the graph of cumulative gas production as shown in **Figure 52**, we observe that the presence of CEE in formation cause formation damage for both water-wet models, which cuts almost the half of the ideal cumulative production.

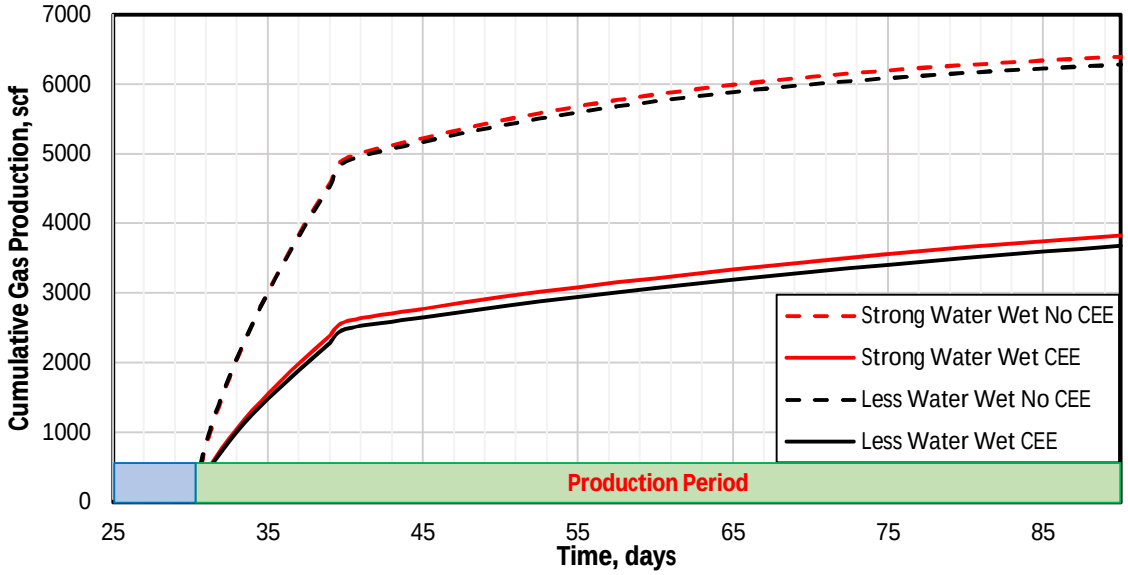

Fig. 52 – Simulation results of cumulative gas production during low-pressure drawdown. The simulation runs without CEE (dash line) and with CEE (solid line).

5.4.3. The Impact of Pressure Drawdown on CEE

The impact of CEE can be reduced by increasing the pressure drop during the production. The large pressure drop increases the viscous forces in the system, which increases the rates of flow. We show this effect by reducing the fracture pressure from 2,500 to 500 psi after 30 days shut-in, i.e., the large drawdown case. The results are shown in water saturation profile for both rock types in **Figure 53** and **Figure 54**. The saturation wave is now somewhat shorter in the presence of CEE and also wave propagation velocity is less.

The simulation results of water flow rate and gas rate during the production are shown in **Figure 55** and **Figure 56.** Indeed, a much lower flowing bottom hole pressure leads to higher flow rates in the formation during the production due to a much larger pressure drawdown imposed. Notice that the gas flow rate is improved to a rate up to 125 bpd when the CEE is ignored. On the graph of the cumulative gas production as shown in **Figure 57**, we observe that the formation models produce gas higher at the first ten day of

production. The formation damage due to CEE now only reduces 30% of the ideal cumulative gas production. It indicate the presence of CEE is weakened. It is suported by **Figure 55** and **Figure 56** that show CEE still exists but the impact is less significant than that at low-pressure drop production. At the 60^{th} day of the production, CEE grows stronger and leads to increase in the immobile water saturation near the fracture and blocks the water migration. However, the trapped water does not force the gas saturation to drop until its saturation reaches the residual water saturation. Moreover, CEE near the fracture can no longer overcome the viscous forces imposed by the higher production rate so that the gas relative permeability stays low. In other words, the gas still can flow to the fracture element and be produced. The result is consistent with the literature (Ashrafi and Helalizadeh, 2014; Hinkley and Davis, 1986; Kyte and Rapoport, 1958): the larger pressure drowdown leads to increases in flow rates and decreases in CEE.

5.4.4. The Impact of Wettability on CEE

During the shut-in, water imbibition develops easier and hence the water saturation wave moves faster into the formation when the formation is less-water wet. Consequently, there will be a larger volume of water invading deeper into the formation. These are shown in **Figure 45**. As consequence, the water movement to the formation become faster and caused the formation area affected by CEE become larger as shown in **Figure 49**. Interestingly, even though wettability has significant impact on the wetting phase of formation fluid by creating high saturation region, this does not cause a further reduction in the gas flow rates as shown in **Figure 51**.

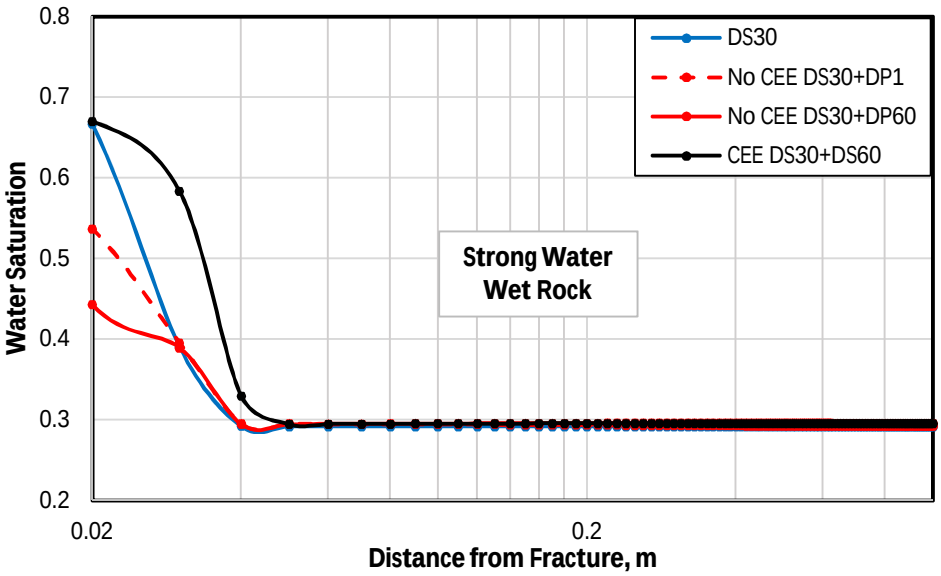

Fig. 53 – Water saturation profile of strong water wet rock during high pressure drop production resulted from numerical simulation. The simulation runs without CEE (red) and with CEE (black) for 30 days of the shut-in (DS30) and continued by 1 and 60 days of production (DP1 and DP60). CEE increases water saturation in the vicinity of the fracture.

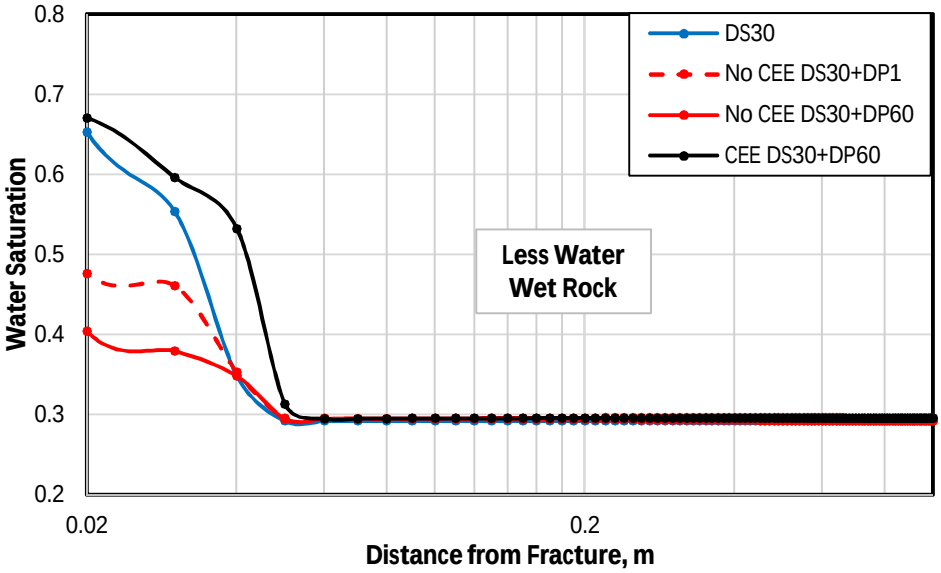

Fig. 54 – Water saturation profile of less water wet rock during high pressure drop production resulted from numerical simulation. The simulation runs without CEE (red) and with CEE (black) for 30 days of the shut-in (DS30) and continued by 1 and 60 days of production (DP1 and DP60). CEE increases water saturation in the vicinity of the fracture.

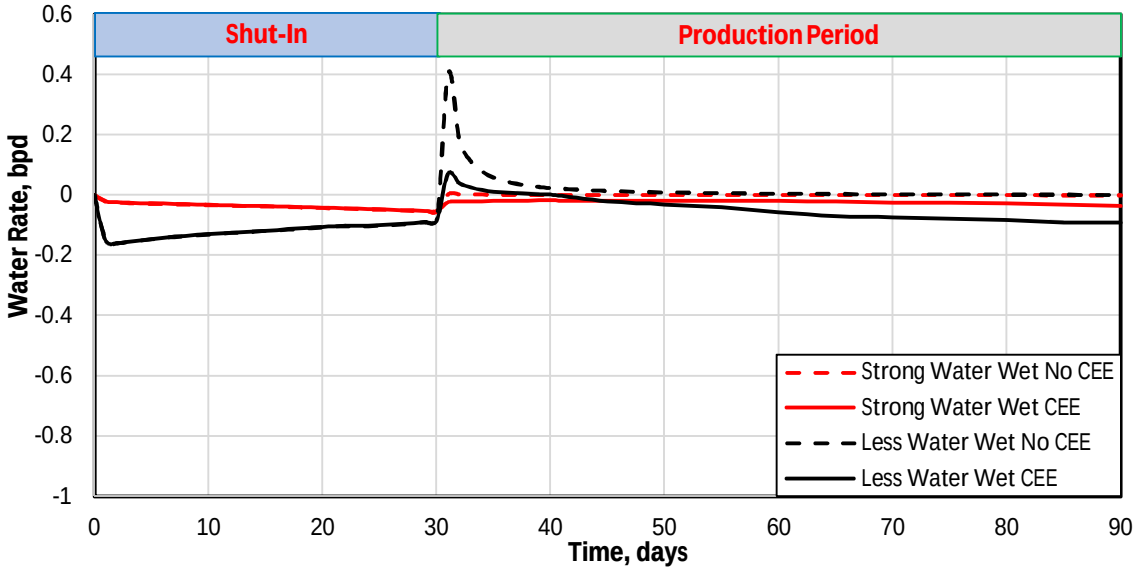

Fig. 55 – Simulation results of water rate during high-pressure drawdown production after 30 days shut-in. The simulation runs without CEE (dash line) and with CEE (solid line).

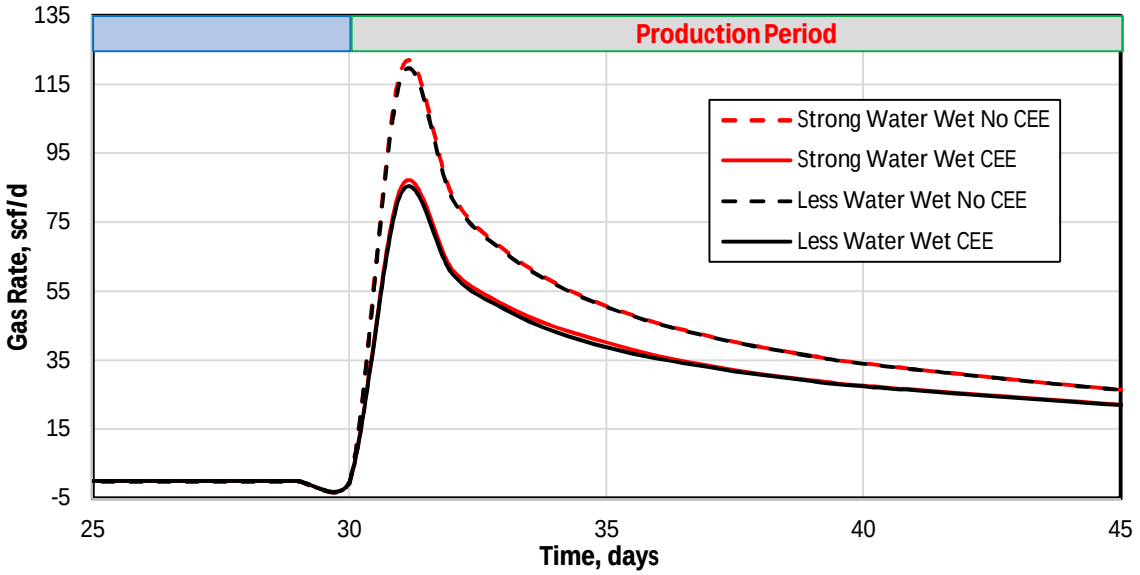

Fig. 56 – Simulation results of gas rate during high-pressure drawdown production after 30 days shut-in. The simulation runs without CEE (dash line) and with CEE (solid line).

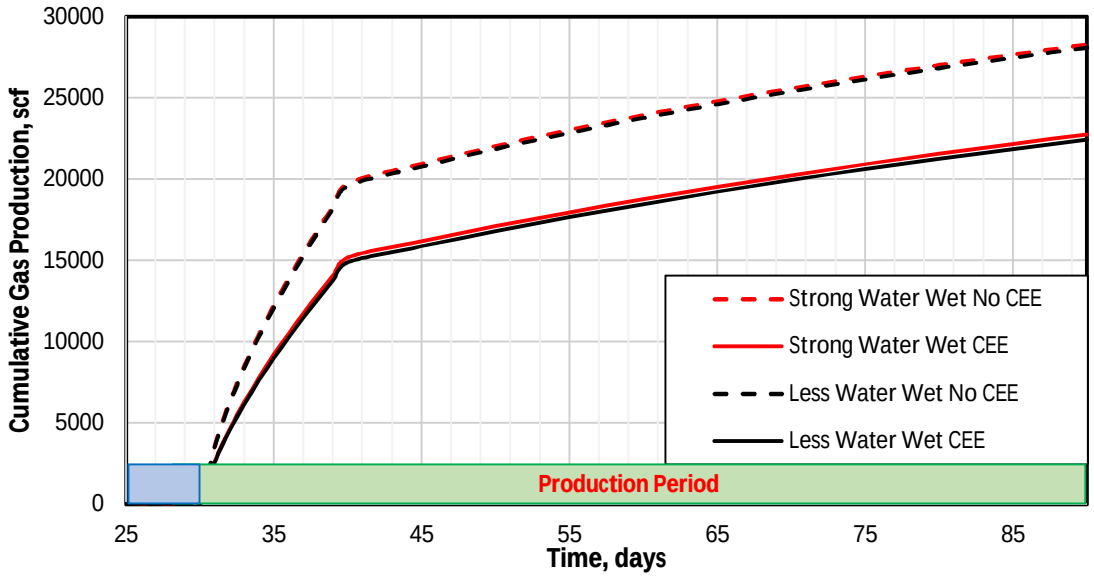

Fig. 57 – Simulation results of cumulative gas production during high-pressure drawdown production after 30 days shut-in. The simulation runs without CEE (dash line) and with CEE (solid line).

5.4.5. The Impact of Gridblock Size

The sensitivity of grid refinement is considered in this section. Here, the previous simulation model, which has length of 2m in x-direction and the block was divided onto 200 blocks each with 10 mm in size. For the sensitivity, we divided into (a) 400 gridblock (Δx = 5mm) in the case of finer gridblock and (b) 40 gridblock (Δx = 50mm) in the case of coarser gridblock. Other simulation parameters including the gridblock size of fracture element are kept the same.

The simulation results in **Figure 58** and **Figure 59** show that the water invasion rate takes longer time with the grid refinement. This makes sense because the water invading into the gridblock needs more time to fill up the pore volume of a smaller gridblock. However, **Figure 60** shows that the change in the water saturation does not

influence the interstitial water saturation that is computed using the CEE model and **Figure 61** shows that no effect on the gas relative permeability. Finally, **Figure 62** and **Figure 63** shows that the computed water pressure values after 1 day or 60 days production do not change with the changing grid size. These results indicate that our simulation results are independent of the grid size.

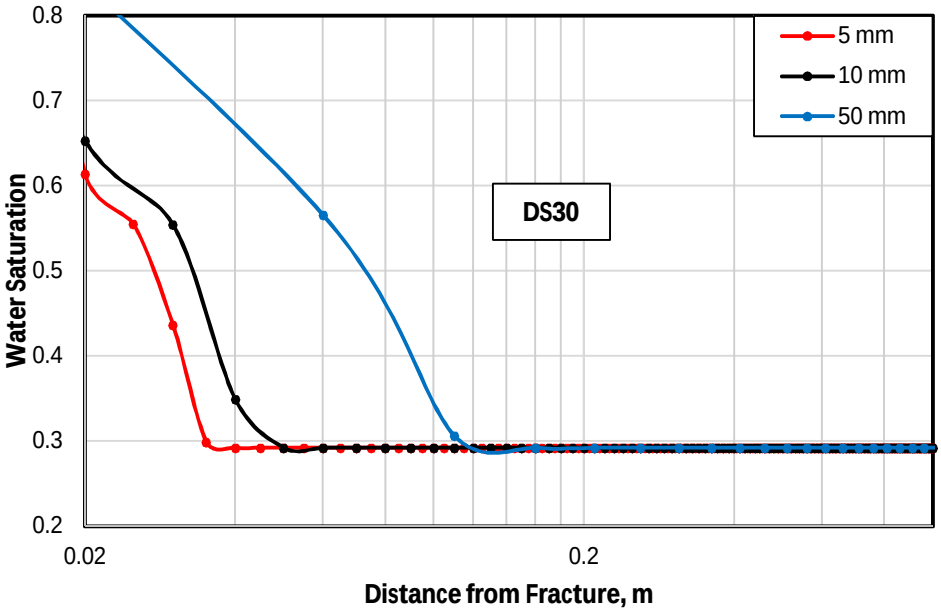

Fig. 58 – Comparison of water saturation using different grid block size, Δx of 5, 10, and 50 mm after 30 days shut-in. Water invasion is further in the case of coarser grid blocks.

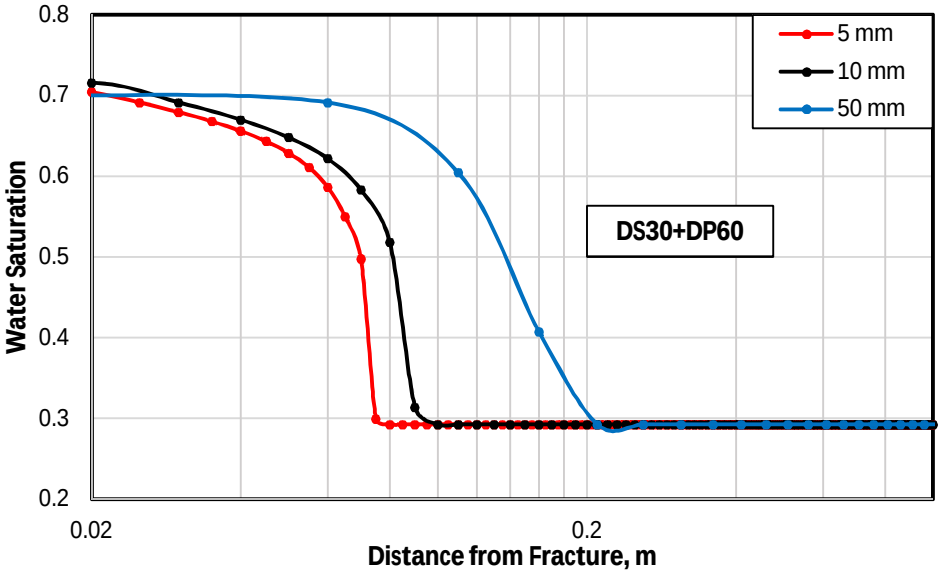

Fig. 59 – Comparison of water saturation using different grid block size, Δx of 5, 10, and 50 mm after 60 days of low pressure drop production in the presence of CEE. Water invasion is further in the case of coarser grid blocks.

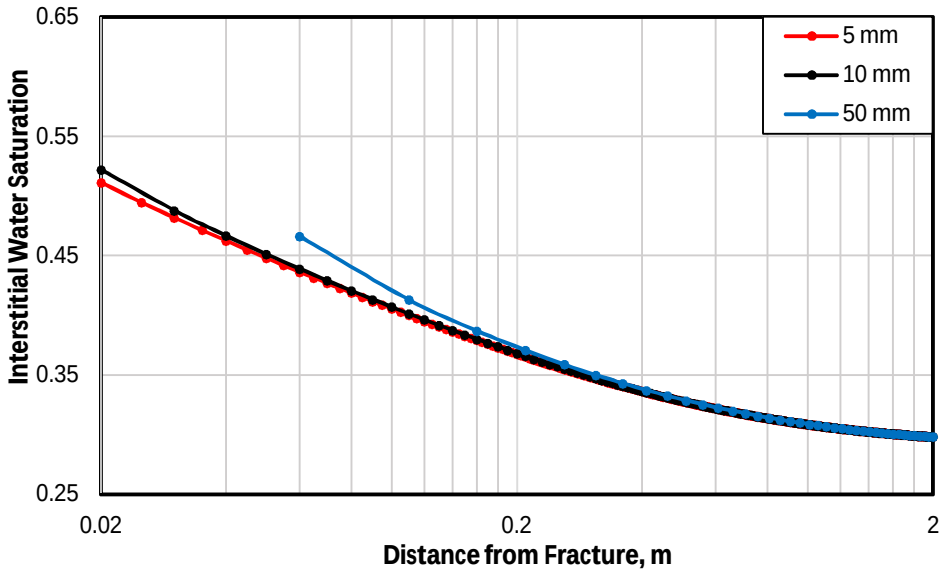

Fig. 60 – Comparison of predicted interstitial water saturation using different grid block size, Δx of 5, 10, and 50 mm during low pressure drop production in the presence of CEE. CEE has a no significant influence on gas relative permeability at S_{iw}.

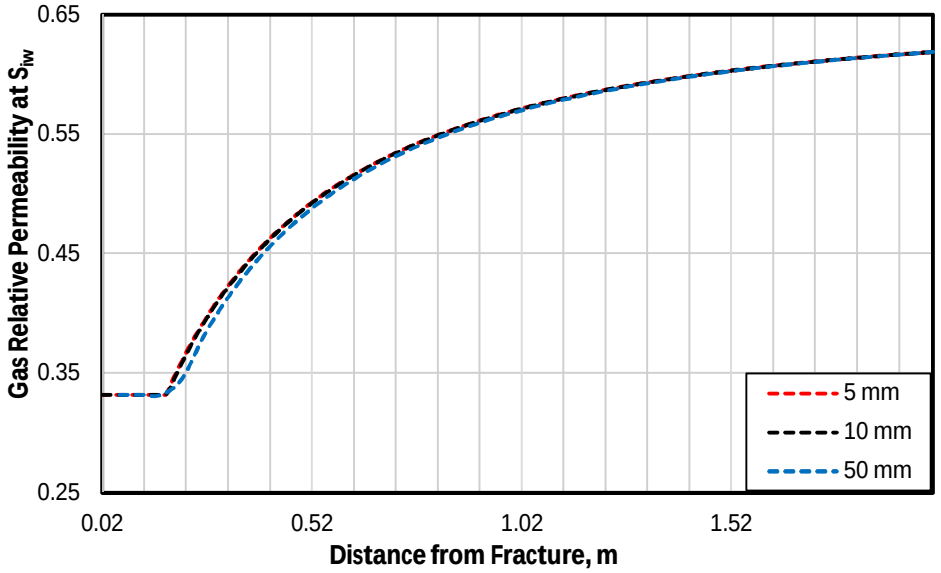

Fig. 61 – Comparison of predicted gas relative permeability at interstitial water saturation using different grid block size, Δx of 5, 10, and 50 mm during low pressure drop production in the presence of CEE. CEE has a no significant influence on gas relative permeability at S_{iw}.

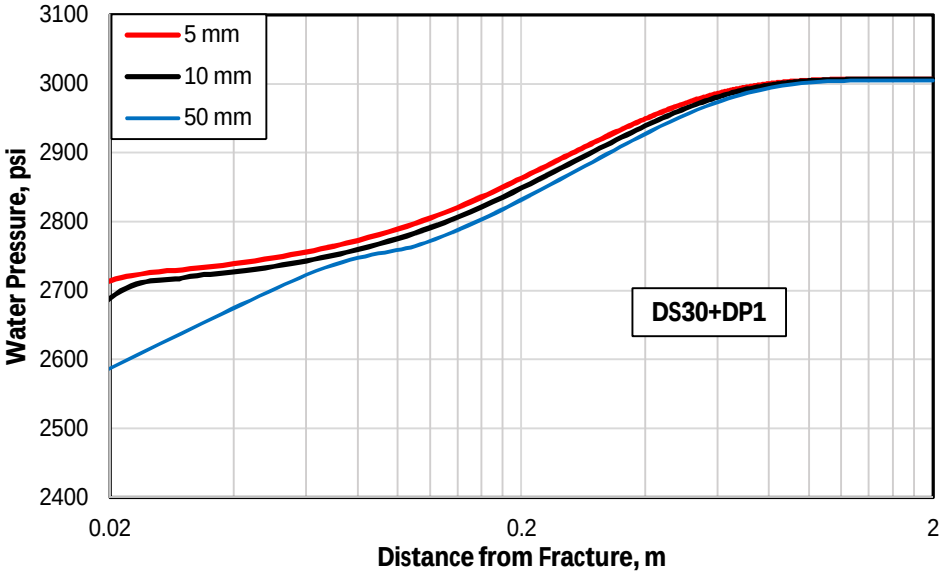

Fig. 62 – Comparison of formation pressure in aqueous phase using different grid block size, Δx of 5, 10, and 50 mm after 30 days shut-in and continued by one day of low pressure drop production in the presence of CEE. The formation pressure drop faster in the case of coarser grid blocks.

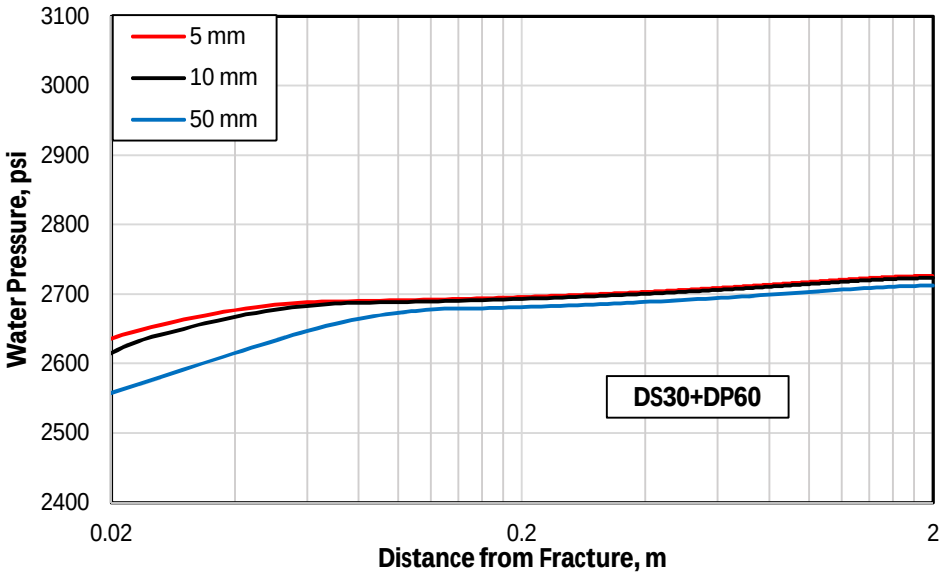

Fig. 63 – Comparison of formation pressure in aqueous phase using different grid block size, Δx of 5, 10, and 50 mm after 30 days shut-in and continued by 60 days of low pressure drop production in the presence of CEE. The formation pressure drop faster in the case of coarser grid blocks.

5.5. Comparison of Formation Damage due to Strees Effect and CEE

High pressure drawdown can solve the CEE problem. However, this can also impact the effective stress the formation experiences near the fracture, which could lead to mechanical damage. One practical consequence of change in the stress is that the permeability of the micro-fractures and cracks could be reduced. According to Gangi's model on Equation (1), the formation pressure drop drastically during the fluids withdrawal from the formation. As a consequence the net effective stress ($P_{conf} - \alpha P$) increases and in the end reduces the permeability. Next, using modeling and numerical simulation approach, we investigate the permeability change due to stress effect and compare to the CEE shown in the previous section.

The parameters used in stress simulation and their values are given in **Table 14**. Now, we repeat the simulations of the previous section in the presence of a dynamic

formation permeability in order to observe the impact of stress-dependent permeability using only the less water wet rock with parameters, given in **Table 14**. The simulation is performed at low-pressure drawdown (2500 psi), when CEE occurs strongly and at high-pressure drawdown (500 psi), which CEE loose its impact, so that we can see the dominance between CEE and stress effects during the production period.

In **Figure 64,** the impact of the changing stress seems weak during the low-pressure drawdown. The stress change reduces the permeability only by 5%, which causes slightly slower absorption of fracturing fluid into formation by spontaneous imbibition. The stress effect is only observed at early time of water flow-back in **Figure 66**. During this time, the water flow rate is controlled dominantly by the changes in conditions near the fracture. Thus, CEE has an important role during the low-pressure drawdown in transporting water from fracture into the formation. At transient flow regime, the impact of both effects are reduced significantly. However, the water is still invading the formation due to CEE, whereas, the 5% permeability reduction due to stress build-up gives insignificant impact on the water production. We also observe that the small permeability change due to stress is not too significant on the gas rate either during the low-pressure drawdown as indicated by the overlapping of the dashed line in **Figure 67**. Meanwhile, by increasing the pressure drop on production, the permeability reduction due to stress becomes more than 35% only in one day of production, as we can see at **Figure 65**, while the impact of CEE is reduced. The impact of stress is indistinguishable at early time production. However, at late time, when the flow now is controlled dominantly by the changes in the formation, the permeability becomes more important factor on the recovery in overcoming the water blocking effect. The large permeability impairment causes additional loss on gas production as shown **Figure 67.**

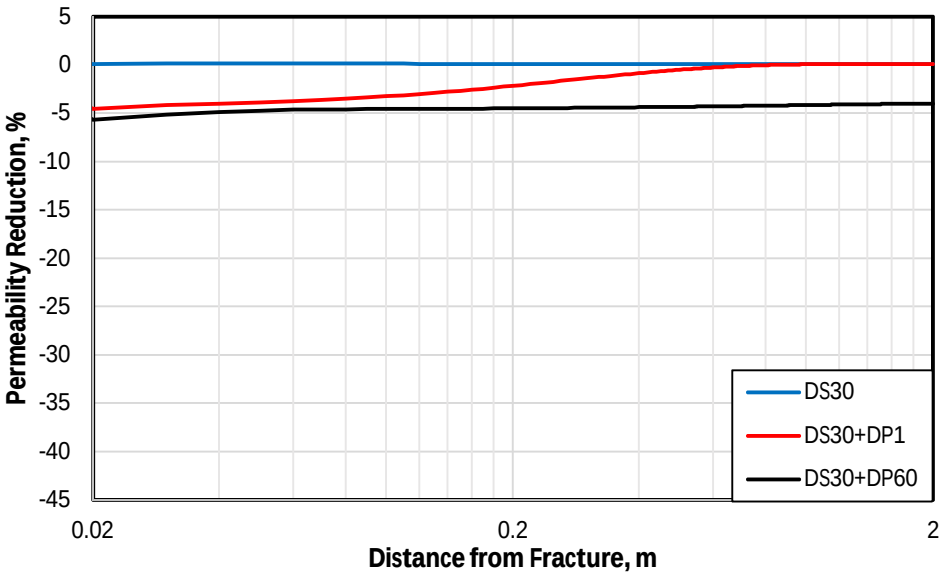

Fig. 64 – Simulation results with dynamic permeability due to stress during low-pressure drawdown production. The simulation runs for 30 days of the shut-in (blue) and continued by 1 (red) and 60 (black) days of production. The permeability reduction due to stress increases by increasing the pressure drop on production.

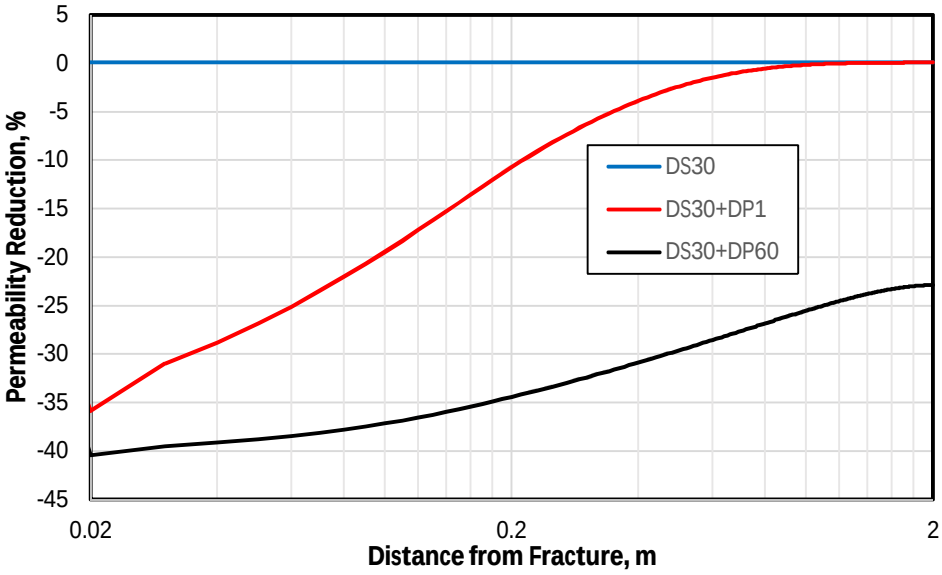

Fig. 65 – Simulation results with dynamic permeability due to stress during high-pressure drawdown production. The simulation runs for 30 days of the shut-in (blue) and continued by 1 (red) and 60 (black) days of production. The permeability reduction due to stress increases by increasing the pressure drop on production.

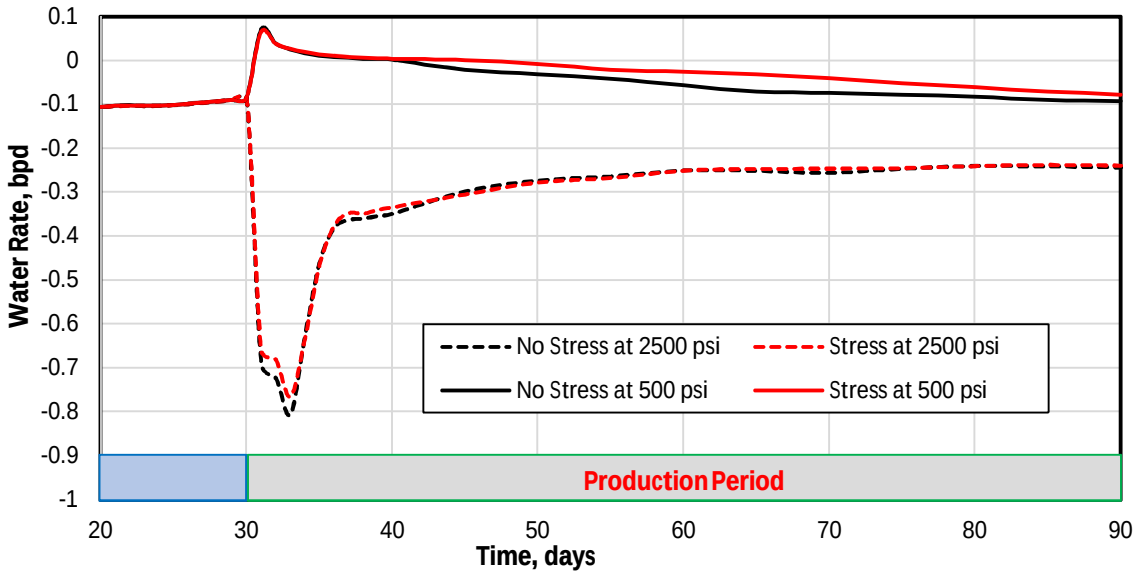

Fig. 66 – Simulation results of water rate during low-pressure (dash line) and high-pressure (solid line) drawdown production. Less water wet rock is used for the simulations. The micro-fracture permeability is considered constant in black lines and stress-dependent in red lines.

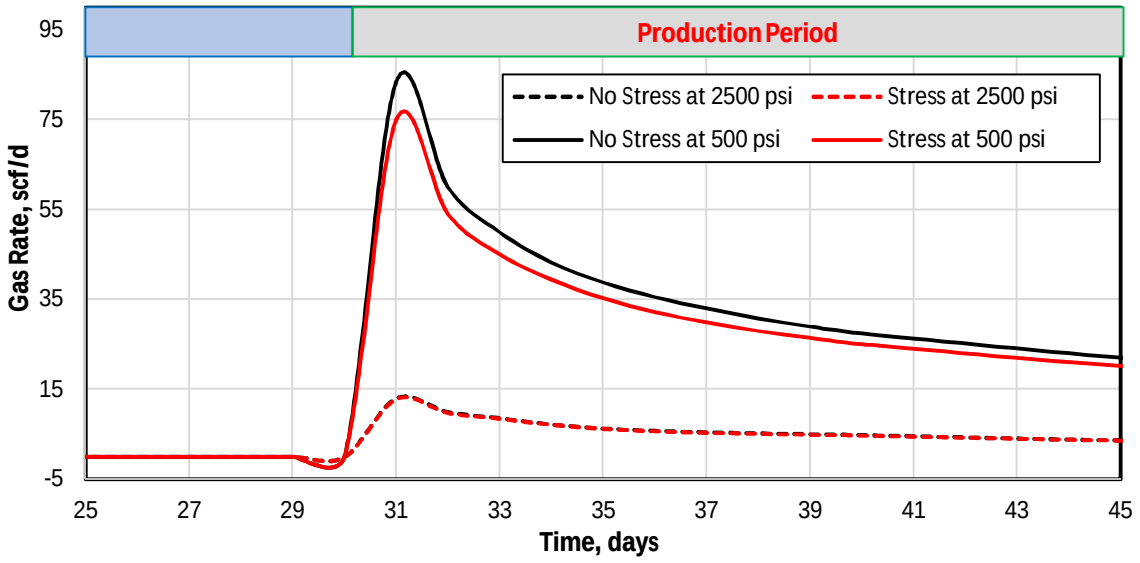

Fig. 67 – Simulation results of gas rate during low-pressure (dash line) and high-pressure (solid line) drawdown production. Less water wet rock is used for the simulations. The micro-fracture permeability is considered constant in black lines and stress-dependent in red lines.

5.5.1. The Impact of Non-Uniform Stress Field Effect during Production Period

The effect of non-uniform stress field during shut-in period is significant change on reservoir properties such as, water saturation, normal mean stress, and permeability, which has been discussed in **Chapter 4**. These changes could potentially impact the well's performance during the flow-back or production. This impact is the topic of this section.

Initially, I use the chemo-thermo-poro-elastic simulation model that solved the problem defined in **Figure 18** using the base values of the parameters given in **Table 10**. In this base case, the impact of temperature and osmosis pressure observed during the first few minutes of shut-in disappear over time. During 2.4 hours shut-in period no effect of temperature and osmosis pressure observed. But the changes in the mean normal stress (hence, permeability) fields and phases saturations prevail over time. These long term effect of the shut-in period is shown in **Figure 68** to **Figure 70**. The flow-back and production can then be simulated considering these non-uniform fields as the initial conditions. Flow-back and production is simulated in the presence of CEE by maintaining a constant pressure of 2500 psi in the fracture element for 72 hours. Now, we shall call the case with a formation temperature of 105^{o}C Case 1. The Case 1 includes the non-uniform fields due to injection of fresh water at 35^{o}C. The similar production process is conducted for the Case 1 including the thermal effect and the osmosis effect during the shut-in. The results are shown in **Figure 71** to **Figure 73**.

Figure 71 shows the graph of water rate vs production time at first matrix grid block near the fracture. Clearly, during the production, water continues to migrate into the formation and this migration takes place at higher rates when Case 1 with non-uniform properties is considered. This is due to the fact that, during early time of shut-in period, the normal stress has decreased due to cold fluid invasion, and consequently, the formation permeability has increased significantly. High water saturation develops and water blocking occurs near the fracture due to CEE during the production period, **Figure 70**. Case 1 with non-uniform fields now has more water volume trapped than the base case, which penetrates to the deeper into the formation. The higher permeability of Case 1 leads

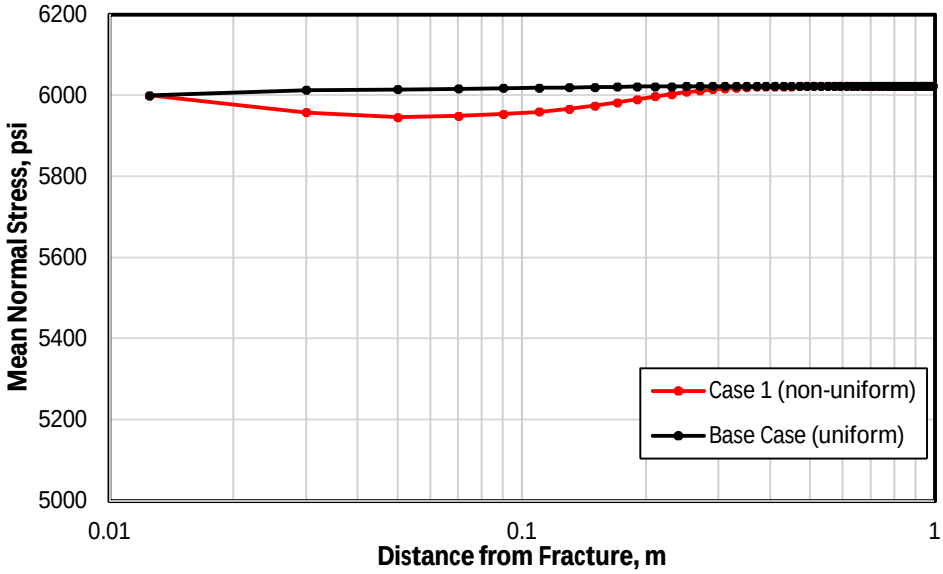

Fig. 68 – The mean normal stress after 2.4 hours shut-in, which is used as initial at production simulation.

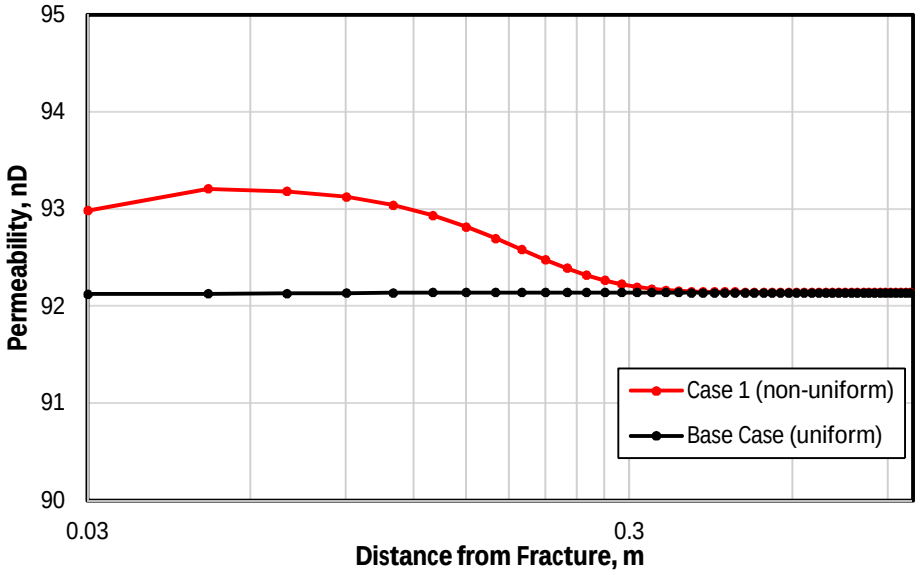

Fig. 69 – The formation permeability after 2.4 hours shut-in, which is used as initial at production simulation.

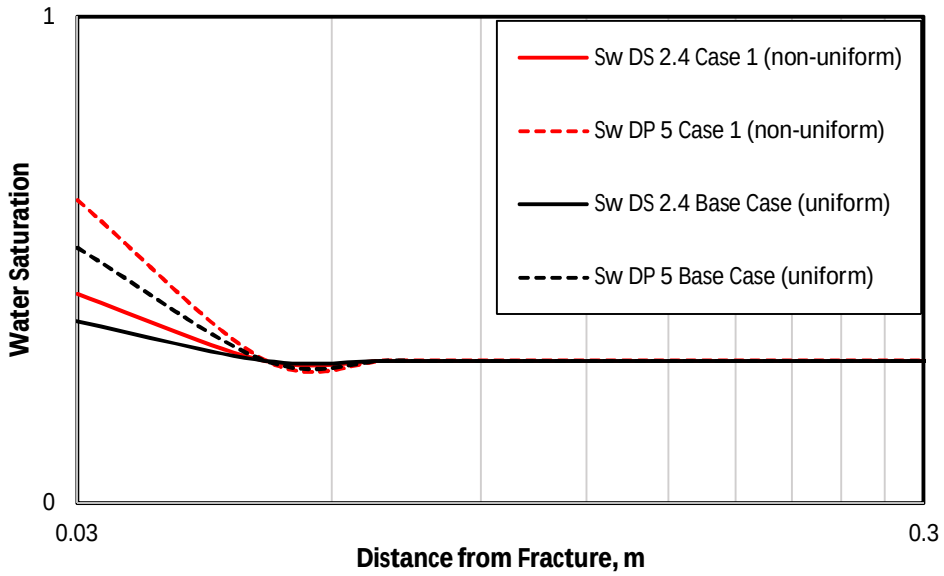

Fig. 70 – The water saturation after 2.4 hours shut-in (DS 2.4) and after 5 hours production (DP 5).

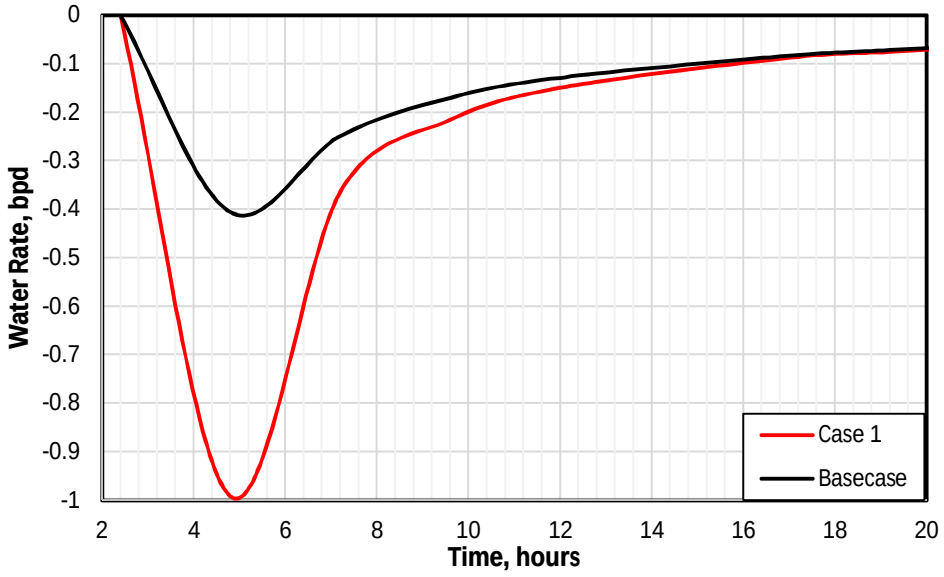

Fig. 71 – Simulation results of water rate first matrix grid block experiences during the production. Higher water absorption during shut-in time because of non-uniform stress fields tends to increase the water blocking caused by CEE.

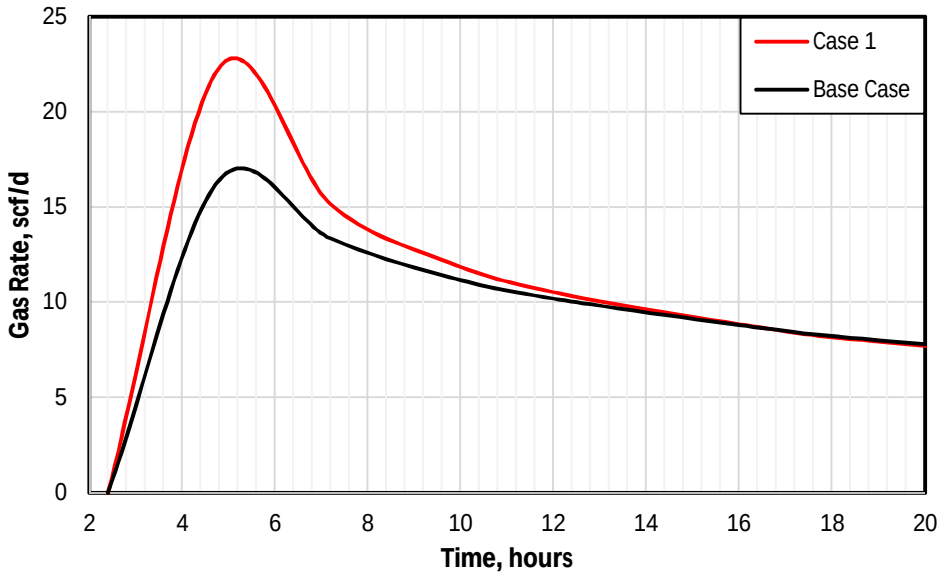

Fig. 72 – Simulation results of gas rate during low-pressure drawdown production. Non-uniform stress field boosts gas rate at early time of production.

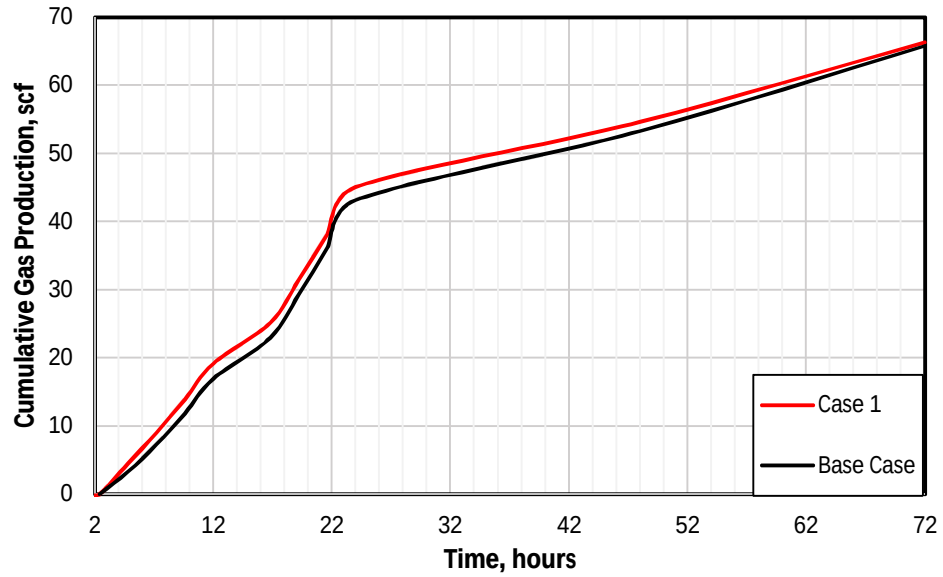

Fig. 73 – Simulation results of cumulative gas production during low-pressure drawdown production. Non-uniform stress field during shut-in gives insignificant impact to cumulative gas production.

to higher gas flow rates at the early time production as shown in **Figure 72**. However, this positive effect on production rate is not large enough to cause a significant impact on the cumulative gas production, **Figure 73**.

6. CONCLUSION

This simulation study shows that non-uniform stress field occurs during hydraulic fracturing and leads to formation damage. The non-uniform stress field occurs fast during the shut-in period, immediately after the formation fluid makes the initial contact with the fracturing fluid which has lower temperature and salinity. A heat transfer from the high-temperature formation to the low-temperature fracture creates a region of changing temperatures. The mean normal stress dynamically changes this region and affects its porosity and permeability.

In addition, the chemical imbalance allows osmosis mechanism through clay semi-permeable membrane and causes clay swelling. The clay swelling increases the net effective stress which leads to changes in permeability. Osmosis reduces the impact of temperature imbalance on mean normal stress and permeability reduction. On the other hand, osmosis makes pressure change stronger. Higher salinity in formation fluids tends to increase formation capillary pressure. However, it gives no significant impact on the other formation properties

The near-fracture capillary end effect has a significant impact on production of water and gas in tight gas and shale formations. The effect increases the water hold-up near the fracture during the flow back and production. The water boundary amplifies the water level of the invading saturation wave into the formation along the production time due to imbibition and creates a liquid block with a more significant impairment for the gas flow, thus, significant loss in gas production. Increasing the pressure drawdown during production is not only increase liquid flowrate but also contributing on CEE reduction.

By changing the formation to less-water wet causes water to invade deeper into formation during the shut-in. Moreover, a higher water saturation region in between the fracture and the flowing gas is created by CEE during the flow back. However, this high saturation region due to wettability does not cause a further reduction in the gas flow rates.

CEE model is independent of the grid size. Furthermore, CEE is a more significant formation damage mechanism compared to changes in stress-dependent permeability. Finally, our results indicate that the CEE could be a serious formation damage mechanism also for tight oil and shale oil formations because these formations experience flow at lower rates during the flow back and production.

REFERENCES

1. Alafnan, S.F.K. and Akkutlu, I.Y. (2018). Matrix-Fracture Interactions during Flow in Organic Nanoporous Materials under Loading. *Transp. Porous Med.* Vol 121:1,69-92.
2. Archer, J. S., & Wong, S. W. (1973). Use of a reservoir simulator to interpret laboratory waterflood data. *Society of Petroleum Engineers Journal*, *13*(06), 343-347.
3. Arthur, J. D., Bohm, B., & Layne, M. (2009). Hydraulic fracturing considerations for natural gas wells of the Marcellus Shale.
4. Arthur, J. D., Langhus, B., & Alleman, D. (2008). An overview of modern shale gas development in the United States. *All Consulting*, *3*, 14-17.
5. Ashrafi, M., & Helalizadeh, A. (2014). Genetic Algorithm for Estimating Relative Permeability and Capillary Pressure from Unsteady-state Displacement Experiments Including Capillary End-effect. *Energy Sources, Part A: Recovery, Utilization, and Environmental Effects*, *36*(22), 2443-2448.
6. Bear, J., 1988, *Dynamics of Fluids in Porous Media*, Chapter 9, Dover, New York.
7. Bennion, D. B., & Thomas, F. B. (2005). Formation damage issues impacting the productivity of low permeability, low initial water saturation gas producing formations. *Journal of Energy Resources Technology*, *127*(3), 240-247.
8. Boyer, C., Kieschnick, J., Suarez-Rivera, R., Lewis, R. E., & Waters, G. (2006). Producing gas from its source. *Oilfield review*, *18*(3), 36-49.
9. Braun, E. M., & Blackwell, R. J. (1981). A steady-state technique for measuring oil-water relative permeability curves at reservoir conditions. In *SPE Annual Technical Conference and Exhibition*. Society of Petroleum Engineers.
10. Brooks, R. H., & Corey, A. T. (1964). Hydraulic properties of porous media, hydrology papers, no. 3, colorado state university, ft. *Collins, Colo*.
11. Bustin, R. M., Bustin, A. M., Cui, A., Ross, D., & Pathi, V. M. (2008). Impact of shale properties on pore structure and storage characteristics. In *SPE shale gas production conference*. Society of Petroleum Engineers.

12. Carman, P. C. (1956). Flow of gases through porous media.
13. Casagrande, I. L. (1949). Electro-osmosis in soils. *Geotechnique*, *1*(3), 159-177.
14. Charlez, P., Lemonnier, P., Ruffet, C., Boutéca, M. J., & Tan, C. (1996, January). Thermally induced fracturing: analysis of a field case in North Sea. In *European Petroleum Conference*. Society of Petroleum Engineers.
15. Chen, G., Chenevert, M. E., Sharma, M. M., & Yu, M. (2003). A study of wellbore stability in shales including poroelastic, chemical, and thermal effects. *Journal of Petroleum Science and Engineering*, *38*(3-4), 167-176.
16. Chen, G., & Ewy, R. T. (2005). Thermoporoelastic effect on wellbore stability. *SPE Journal*, *10*(02), 121-129.
17. Cheng, Y. (2012). Impact of water dynamics in fractures on the performance of hydraulically fractured wells in gas-shale reservoirs. *J. Canadian Petroleum Technology*, *51*(02), 143-151.
18. Choi, S. K., & Tan, C. P. (1998). Modelling of effects of drilling fluid temperature on wellbore stability. In *SPE/ISRM Rock Mechanics in Petroleum Engineering*. Society of Petroleum Engineers.
19. Christiansen, R. 2005. Capillary End Effects and Gas Production from Low Permeability Formations. Paper presented at the *Int. Symposium of the Society of Core Analysts* held in Toronto, Canada, 11-15 August.
20. Cipolla, C. L., Lolon, E. P., Erdle, J. C., & Rubin, B. (2010). Reservoir Modeling in Shale-Gas Reservoirs. Society of Petroleum Engineers. doi:10.2118/125530-PA.
21. Cipolla, C. L., Warpinski, N. R., Mayerhofer, M. J., Lolon, E., & Vincent, M. C. (2008). The Relationship Between Fracture Complexity, Reservoir Properties, and Fracture Treatment Design. Society of Petroleum Engineers. doi:10.2118/115769-MS.
22. Civan, F., & Donaldson, E. C. (1989). Relative permeability from unsteady-state displacements with capillary pressure included. *SPE Formation Evaluation*, *4*(02), 189-193.

23. Cooper, J. R., & Dooley, R. B. (2008). Release of the IAPWS formulation 2008 for the viscosity of ordinary water substance. *The International Association for the Properties of Water and Steam*.

24. Curtis, J. B. (2002). Fractured shale-gas systems. *AAPG bulletin*, *86*(11), 1921-1938.

25. Dacy, J. M. (2010). Core tests for relative permeability of unconventional gas reservoirs. In *SPE Annual Technical Conference and Exhibition*. Society of Petroleum Engineers.

26. Davies, D. K., Bryant, W. R., Vessell, R. K., & Burkett, P. J. (1991). Porosities, permeabilities, and microfabrics of Devonian shales. In *Microstructure of fine-grained sediments* (pp. 109-119). Springer, New York, NY.

27. Davies, J. P., & Davies, D. K. (1999). Stress-Dependent Permeability: Characterization and Modeling. Society of Petroleum Engineers. doi:10.2118/56813-MS.

28. Dirksen, C. (1969). Thermo-Osmosis Through Compacted Saturated Clay Membranes 1. *Soil Science Society of America Journal*, *33*(6), 821-826.

29. Dong, J. J., Hsu, J. Y., Wu, W. J., Shimamoto, T., Hung, J. H., Yeh, E. C., ... & Sone, H. (2010). Stress-dependence of the permeability and porosity of sandstone and shale from TCDP Hole-A. *International Journal of Rock Mechanics and Mining Sciences*, *47*(7), 1141-1157.

30. Donnelly, B. M. (2015). Measurement of Hysteretic Shale Capillary Pressure–Saturation Relationships using a Water Activity Meter.

31. Donnelly, B., Perfect, E., McKay, L. D., Lemiszki, P. J., DiStefano, V. H., Anovitz, L. M., ... & Cheng, C. L. (2016). Capillary pressure–saturation relationships for gas shales measured using a water activity meter. *Journal of Natural Gas Science and Engineering*, *33*, 1342-1352.

32. Eveline V.F., Akkutlu, I.Y. & Moridis, G.J. (2017). Numerical Simulation of Hydraulic Fracturing Water Effects on Shale Gas Permeability Alteration. *J. Transport in Porous Media*, Vol. 116, No 2, 727-752.

33. Fakcharoenphol, P., Torcuk, M., Kazemi, H., & Wu, Y. S. (2016). Effect of shut-in time on gas flow rate in hydraulic fractured shale reservoirs. *Journal of Natural Gas Science and Engineering*, *32*, 109-121.

34. Fan, L., Thompson, J. W., & Robinson, J. R. (2010, January). Understanding gas production mechanism and effectiveness of well stimulation in the Haynesville Shale through reservoir simulation. In *Canadian Unconventional Resources and International Petroleum Conference*. Society of Petroleum Engineers.

35. Firoozabadi, A., & Ramey Jr, H. J. (1988). Surface tension of water-hydrocarbon systems at reservoir conditions. *Journal of Canadian Petroleum Technology*, *27*(03).

36. Fisher, M. K., Wright, C. A., Davidson, B. M., Steinsberger, N. P., Buckler, W. S., Goodwin, A., & Fielder, E. O. (2005). Integrating fracture mapping technologies to improve stimulations in the Barnett shale. *SPE Production & Facilities*, *20*(02), 85-93.

37. Fritz, S. J. (1986). Ideality of clay membranes in osmotic processes: a review. *Clays and clay minerals*, *34*(2), 214-223.

38. Gabriel, G. A., & Inamdar, G. R. (1983). An experimental investigation of fines migration in porous media. In *SPE Annual Technical Conference and Exhibition*. Society of Petroleum Engineers.

39. Gangi, A. F. 1978. Variation of whole and fractured porous rock permeability with confining pressure. In *International Journal of Rock Mechanics and Mining Sciences & Geomechanics Abstracts*, Pergamon, Vol. 15, No. 5, pp. 249-257.

40. Gensterblum, Y., & Krooss, B. M. (2013). Fluid-dynamical and poro-elastic coupling of gas permeability of inert and sorbing gases on an Australian sub-bituminous coal. In *AGU Fall Meeting Abstracts*.

41. Ghanbari, E., Xu, M., Dehghanpour, H., & Bearinger, D. (2014). Advances in understanding liquid flow in gas shales. In *SPE/CSUR Unconventional Resources Conference–Canada*. Society of Petroleum Engineers.

42. Ghassemi, A., & Diek, A. (2002). Porothermoelasticity for swelling shales. *Journal of Petroleum Science and Engineering*, *34*(1-4), 123-135.

43. Gonzalez, M. E., Bloys, J. B., Lofton, J. E., Pepin, G. P., Schmidt, J. H., Naquin, C. J., ... & Laursen, P. E. (2004). Increasing effective fracture gradients by managing wellbore temperatures. In *IADC/SPE Drilling Conference*. Society of Petroleum Engineers.

44. Guidry, K., Luffel, D., & Curtis, J. (1996). *Development of laboratory and petrophysical techniques for evaluating shale reservoirs. Final technical report, October 1986-September 1993* (No. PB-96-174859/XAB). ResTech Houston, Inc., TX (United States).

45. Gupta, R., & Maloney, D. R. (2016). Intercept Method--A Novel Technique To Correct Steady-State Relative Permeability Data for Capillary End Effects. *SPE Reservoir Evaluation & Engineering*, *19*(02), 316-330.

46. Hadley, G. F., & Handy, L. L. (1956). A Theoretical and Experimental Study of the Steady-state Capillary End Effect. In *Fall Meeting of the Petroleum Branch of AIME*. Society of Petroleum Engineers.

47. Haluszczak, L. O., Rose, A. W., & Kump, L. R. (2013). Geochemical evaluation of flowback brine from Marcellus gas wells in Pennsylvania, USA. *Applied Geochemistry*, *28*, 55-61.

48. Hanshaw, B. B. (1962). *Membrane properties of compacted clays* (Doctoral dissertation, Harvard University, Cambridge).

49. Hinkley, R. E., & Davis, L. A. (1986). Capillary Pressure Discontinuities and End Effects in Homogeneous Composite Cores: Effect of Flow Rate and Wettability. Presented during the *SPE Annual Technical Conference and Exhibition*. Society of Petroleum Engineers.

50. Honarpour, M. M., Nagarajan, N. R., Orangi, A., Arasteh, F., & Yao, Z. (2012). Characterization of critical fluid PVT, rock, and rock-fluid properties-impact on reservoir performance of liquid rich shales. In *SPE Annual Technical Conference and Exhibition*. Society of Petroleum Engineers.

51. Huang, D. D., & Honarpour, M. M. (1998). Capillary End Effects in Coreflood Calculations. *Journal of Petroleum Science and Engineering*, *19*(1), 103-117.

52. Huber, M. L., Perkins, R. A., Friend, D. G., Sengers, J. V., Assael, M. J., Metaxa, I. N., ... & Vogel, E. (2012). New international formulation for the thermal conductivity of H2O. *Journal of Physical and Chemical Reference Data*, *41*(3), 033102.

53. Jaeger, J. C., Cook, N. G. W., & Zimmermann, R. W. (2007). Fundamentals of rock mechanics, edited by Chapman and Hall. *New York, United States of America*, 1-593.

54. King, G. E. (2012). Hydraulic fracturing 101: what every representative, environmentalist, regulator, reporter, investor, university researcher, neighbor and engineer should know about estimating frac risk and improving frac performance in unconventional gas and oil wells. In *SPE hydraulic fracturing technology conference*. Society of Petroleum Engineers.

55. Kuila, U., & Prasad, M. (2013). Specific surface area and pore-size distribution in clays and shales. *Geophysical Prospecting*, *61*(2), 341-362.

56. Kyte, J. R., & Rapoport, L. A. (1958). Linear Waterflood Behavior and End Effects in Water-wet Porous Media. *Journal of Petroleum Technology*, *10*(10), 47-50.

57. Lal, M. (1999). Shale stability: drilling fluid interaction and shale strength. In *SPE Asia Pacific Oil and Gas Conference and Exhibition*. Society of Petroleum Engineers.

58. Leverett, M.C. (1941). Capillary behavior in porous solids. *Trans. AIME* Vol. 142, No. 01, 152-169.

59. Li, X., Cui, L., & Roegiers, J. C. (1998). Thermoporoelastic analyses of inclined boreholes. In *SPE/ISRM Rock Mechanics in Petroleum Engineering*. Society of Petroleum Engineers.

60. Liang, T., Longoria, R. A., Lu, J., Nguyen, Q. P., & DiCarlo, D. A. (2017). Enhancing Hydrocarbon Permeability after Hydraulic Fracturing: Laboratory Evaluations of Shut-ins and Surfactant Additives. *SPE Journal*, 22(4), 1011-1023.

61. Lubinski, A. (1954, June). The theory of elasticity for porous bodies displaying a strong pore structure. In *Proc* (pp. 247-256).
62. Madsen, F. T., & Müller-Vonmoos, M. (1989). The swelling behaviour of clays. *Applied Clay Science*, *4*(2), 143-156.
63. Makhanov, K., Dehghanpour, H., & Kuru, E. (2012). An experimental study of spontaneous imbibition in Horn River shales. In *SPE Canadian unconventional resources conference*. Society of Petroleum Engineers.
64. Marine, I. W., & Fritz, S. J. (1981). Osmotic model to explain anomalous hydraulic heads. *Water Resources Research*, *17*(1), 73-82.
65. Maury, V., & Idelovici, J. L. (1995). Safe drilling of HP/HT wells, the role of the thermal regime in loss and gain phenomenon. In *SPE/IADC Drilling Conference*. Society of Petroleum Engineers.
66. Mayerhofer, M. J., Lolon, E., Warpinski, N. R., Cipolla, C. L., Walser, D. W., & Rightmire, C. M. (2010). What is stimulated reservoir volume?. *SPE Production & Operations*, *25*(01), 89-98.
67. McClure, M. W., Babazadeh, M., Shiozawa, S., & Huang, J. (2016). Fully coupled hydromechanical simulation of hydraulic fracturing in 3D discrete-fracture networks. *SPE Journal*, *21*(04), 1-302.
68. McTigue, D. F. (1986). Thermoelastic response of fluid-saturated porous rock. *Journal of Geophysical Research: Solid Earth*, *91*(B9), 9533-9542.
69. Medved, I., & Černý, R. (2013). Osmosis in porous media: A review of recent studies. *Microporous and Mesoporous Materials*, *170*, 299-317.
70. Meng, M., Ge, H., Ji, W., Shen, Y., & Su, S. (2015). Monitor the process of shale spontaneous imbibition in co-current and counter-current displacing gas by using low field nuclear magnetic resonance method. *Journal of Natural Gas Science and Engineering*, *27*, 336-345.
71. Moghaddam, R. N., & Jamiolahmady, M. (2019). Steady-State Relative Permeability Measurements of Tight and Shale Rocks Considering Capillary End Effect. *Transport in Porous Media*, 1-22.

72. Moridis, G. (2014). *User's Manual of the TOUGH+ Core Code v1. 5: A General-Purpose Simulator of Non-Isothermal Flow and Transport through Porous and Fractured Media* (No. LBNL-6871E). Ernest Orlando Lawrence Berkeley National Laboratory, Berkeley, CA, USA.

73. Mueller, M., Amro, M., Haefner, F. K. A., & Hossain, M. M. (2012). Stimulation of Tight Gas Reservoir using coupled Hydraulic and CO2 Cold-frac Technology. Society of Petroleum Engineers. doi:10.2118/160365-MS.

74. Narasimhan, T. N., & Witherspoon, P. A. (1976). An integrated finite difference method for analyzing fluid flow in porous media. *Water Resources Research*, *12*(1), 57-64.

75. Neuzil, C. E. (1994). How permeable are clays and shales?. *Water resources research*, *30*(2), 145-150.

76. Orangi, A., Nagarajan, N. R., Honarpour, M. M., & Rosenzweig, J. J. (2011). Unconventional shale oil and gas-condensate reservoir production, impact of rock, fluid, and hydraulic fractures. In *SPE hydraulic fracturing technology conference*. Society of Petroleum Engineers.

77. Osoba, J. S., Richardson, J. G., Kerver, J. K., Hafford, J. A., & Blair, P. M. (1951). Laboratory Measurements of Relative Permeability. *Journal of Petroleum Technology*, *3*(2), 47-56.

78. Ougier-Simonin, A., Renard, F., Boehm, C., & Vidal-Gilbert, S. (2016). Microfracturing and Microporosity in shales. *Earth-Science Reviews*, *162*, 198-226.

79. Moghadams, M., Hinkel, J. J., & Willberg, D. M. (2012). Measuring capillary pressure tells more than pretty pictures. In *SPE International Symposium and Exhibition on Formation Damage Control*. Society of Petroleum Engineers.

80. Pagels, M., Willberg, D. M., Edelman, E., Zagorski, W., & Frantz, J. (2013). Quantifying fracturing fluid damage on reservoir rock to optimize production. In *Unconventional Resources Technology Conference* (pp. 1766-1774). Society of

Exploration Geophysicists, American Association of Petroleum Geologists, Society of Petroleum Engineers.

81. Palisch, T. T., Vincent, M., & Handren, P. J. (2010). Slickwater fracturing: food for thought. *SPE Production & Operations*, *25*(03), 327-344.

82. Passey, Q. R., Bohacs, K., Esch, W. L., Klimentidis, R., & Sinha, S. (2010). From oil-prone source rock to gas-producing shale reservoir-geologic and petrophysical characterization of unconventional shale gas reservoirs. In *International oil and gas conference and exhibition in China*. Society of Petroleum Engineers.

83. Peng, D. Y., & Robinson, D. B. (1976). A new two-constant equation of state. *Industrial & Engineering Chemistry Fundamentals*, *15*(1), 59-64.

84. Perkins, T. K., & Gonzalez, J. A. (1984). Changes in earth stresses around a wellbore caused by radially symmetrical pressure and temperature gradients. *Society of Petroleum Engineers Journal*, *24*(02), 129-140.

85. Perkins, T. K., & Gonzalez, J. A. (1985). The effect of thermoelastic stresses on injection well fracturing. *Society of Petroleum Engineers Journal*, *25*(01), 78-88.

86. Perrodon, A. (1983). *Dynamics of oil and gas accumulations* (Vol. 5). Editions TECHNIP.

87. Poling, B. E., Prausnitz, J. M., & O'connell, J. P. (2001). *The properties of gases and liquids* (Vol. 5). New York: Mcgraw-hill.

88. Pruess, K., Oldenburg, C., & Moridis, G. (1998). Overview of TOUGH2, version 2.0. *LBNL–Lawrence Berkeley National Laboratory, Report: LBNL-41995, Univ. of California, Lawrence Berkeley National Lab.*, 307-314.

89. Qin, B. (2007). *Numerical study of recovery mechanisms in tight gas reservoirs* (Doctoral dissertation, University of Oklahoma).

90. Reed, R. M., John, A., & Katherine, G. (2007). Nanopores in the Mississippian Barnett Shale: distribution, morphology, and possible genesis. In *GAS Annual Meeting & Exposition. Denver*.

91. Richardson, J. G., Kerver, J. K., Hafford, J. A., & Osoba, J. S. (1952). Laboratory Determination of Relative Permeability. *Journal of Petroleum Technology*, *4*(08), 187-196.

92. Romanenko, K., & Balcom, B. J. (2013). An assessment of non-wetting phase relative permeability in water-wet sandstones based on quantitative MRI of capillary end effects. *Journal of Petroleum Science and Engineering*, *110*, 225-231.

93. Rutqvist, J., & Tsang, C. F. (2002). A study of caprock hydromechanical changes associated with CO 2-injection into a brine formation. *Environmental Geology*, *42*(2-3), 296-305.

94. Scott, H., Patey, I. T. M., & Byrne, M. T. (2007). Relative Permeability Measurements Proceed With Caution. Presented during the *European Formation Damage Conference*, Society of Petroleum Engineers.

95. Shaoul, J. R., van Zelm, L. F., & De Pater, C. J. (2011). Damage Mechanisms in Unconventional-gas-well Stimulation--A New Look at an Old Problem. *SPE Production & Operations*, *26*(04), 388-400.

96. Soeder, D. J. (1988). Porosity and permeability of eastern Devonian gas shale. *SPE Formation Evaluation*, *3*(01), 116-124.

97. Soliman, M. Y., Hunt, J. L., & Azari, M. (1996). Fracturing Horizontal Wells In Gas Reservoirs. Society of Petroleum Engineers. doi:10.2118/35260-MS.

98. Somerton, W. H., El-Shaarani, A. H., & Mobarak, S. M. (1974). High temperature behavior of rocks associated with geothermal type reservoirs. In *SPE California Regional Meeting*. Society of Petroleum Engineers.

99. Standing, M. B. (1975). Notes on Relative Permeability Relationships. *Lecture Notes, Trondheim, Norway*.

100. Stoneburner, R. K. (2009). The Haynesville and Hawkville Fields: two world-class gas shale plays.

101. Sun, X., & Mohanty, K. (2005). Simulation of Methane Hydrate Reservoirs. In *2005 SPE Reservoir Simulation Symposium, Proceedings*.

102. Sun, Z., Li, X., Shi, J., Zhang, T., & Sun, F. (2017). Apparent permeability model for real gas transport through shale gas reservoirs considering water distribution characteristic. *International Journal of Heat and Mass Transfer, 115*, 1008-1019.

103. Svendson, A. P., Wright, M. S., Clifford, P. J., & Berry, P. J. (1991,). Thermally Induced Fracturing of Ula Water Injectors. Society of Petroleum Engineers. doi:10.2118/20898-PA.

104. Tang, L., & Luo, P. (1998). The Effect of the Thermal Stress on Wellbore Stability. In *SPE India Oil and Gas Conference and Exhibition*. Society of Petroleum Engineers.

105. Taylor, R. S., McIntosh, G., Litun, R., Munn, D., Bennion, B., Piwowar, M., ... & Hoch, O. (2009). Montney fracturing-fluid considerations. In *Canadian International Petroleum Conference*. Petroleum Society of Canada.

106. Trémosa, J., Gonçalvès, J., Matray, J. M., & Violette, S. (2010). Estimating thermo-osmotic coefficients in clay-rocks: II. In situ experimental approach. *Journal of colloid and interface science*, *342*(1), 175-184.

107. Van Oort, E. (2003). On the physical and chemical stability of shales. *Journal of Petroleum Science and Engineering*, *38*(3-4), 213-235.

108. Virnovsky, G. A., Skjaeveland, S. M., Surdal, J., & Ingsoy, P. (1995). Steady-state Relative Permeability Measurements Corrected for Capillary Effects. Paper presented during the *SPE Annual Technical Conference and Exhibition*. Society of Petroleum Engineers.

109. Wagner, W., J. Cooper, A. Dittmann et al. (2000). The IAPWS industrial formulation 1997 for the thermodynamic properties of water and steam. *Journal of engineering for gas turbines and power* 122 (1): 150-184.

110. Wang, F., Pan, Z., & Zhang, S. (2017). Impact of chemical osmosis on water leakoff and flowback behavior from hydraulically fractured gas shale. *Journal of Petroleum Science and Engineering*, *151*, 264-274.

111. Wang, F. P., & Reed, R. M. (2009). Pore networks and fluid flow in gas shales. In *SPE annual technical conference and exhibition*. Society of Petroleum Engineers.

112. Wang, M., & Leung, J. Y. (2015). Numerical Investigation of Coupling Multiphase Flow and Geomechanical Effects on Water Loss During Hydraulic Fracturing Flow Back Operation. In *Unconventional Resources Technology Conference, San Antonio, Texas, 20-22 July 2015* (pp. 1224-1243). Society of Exploration Geophysicists, American Association of Petroleum Geologists, Society of Petroleum Engineers.

113. Wang, Y., & Papamichos, E. (1994). Conductive heat flow and thermally induced fluid flow around a well bore in a poroelastic medium. *Water Resources Research*, *30*(12), 3375-3384.

114. Warpinski, N. R., Mayerhofer, M. J., Vincent, M. C., Cipolla, C. L., & Lolon, E. P. (2009). Stimulating unconventional reservoirs: maximizing network growth while optimizing fracture conductivity. *Journal of Canadian Petroleum Technology*, *48*(10), 39-51.

115. Wasaki, A., & Akkutlu, I. Y. (2015). Permeability of organic-rich shale. *SPE Journal*, *20*(06), 1-384.

116. Weng, X., Kresse, O., Cohen, C. E., Wu, R., & Gu, H. (2011). Modeling of Hydraulic Fracture Network Propagation in a Naturally Fractured Formation. Society of Petroleum Engineers. doi:10.2118/140253-MS.

117. Wilson, R. K., & Aifantis, E. C. (1982). On the theory of consolidation with double porosity. *International Journal of Engineering Science*, *20*(9), 1009-1035.

118. Winterfeld, P. H., & Wu, Y. S. (2016). Simulation of coupled thermal/hydrological/mechanical phenomena in porous media. *Spe Journal*, *21*(03), 1-041.

119. Yu, M. (2002). *Chemical and thermal effects on wellbore stability of shale formations* (Doctoral dissertation).

APPENDIX A - MEAN NORMAL STRESS GEOMECHANICAL FORMULATION

This appendix discusses the detail derivation of the coupled geomechanical equation used in the numerical simulation. The derivation of the governing geomechanical and thermo-poro-elastic behavior is based on the poro-elasticity model proposed by Jaeger et al., 2007; Fakcharoenphol et al., 2013.

The mean normal stress geomechanical formula is a stress-strain relation of a nonporous material. Jaeger et al. (2007) expressed this relation in terms of the elastic shear modulus or rigidity (G) and Poisson ratio (v) as follows:

$$\varepsilon_{xx} = \frac{1}{2G}\left[\sigma_{xx} - \frac{v}{(1+v)}\left(\sigma_{xx} + \sigma_{yy} + \sigma_{zz}\right)\right] \quad (119)$$

$$\varepsilon_{yy} = \frac{1}{2G}\left[\sigma_{yy} - \frac{v}{(1+v)}\left(\sigma_{xx} + \sigma_{yy} + \sigma_{zz}\right)\right] \quad (120)$$

$$\varepsilon_{zz} = \frac{1}{2G}\left[\sigma_{zz} - \frac{v}{(1+v)}\left(\sigma_{xx} + \sigma_{yy} + \sigma_{zz}\right)\right] \quad (121)$$

In matrix form, which is assumed infinitesimal condition (I):

$$\varepsilon = \frac{\sigma}{2G} - \frac{v}{2G(1+v)} tr(\sigma)\mathsf{I} \quad (122)$$

where I is the identity vector $[1,1,1]^{-1}$.

A pore pressure increment must be added to each longitudinal strain for isotropic fluid filled porous rocks since the bulk volume is a subject to change in stress in poroelastic medium. The Equation (122) become:

$$\varepsilon = \frac{\sigma}{2G} - \frac{v}{2G(1+v)} tr(\sigma)\mathsf{I} - \frac{C_{bp}}{3} P_p \mathsf{I} \quad (123)$$

where C_{bp} and P_p are the pore compressibility and pore pressure of the rock. Biot's coefficient for a double porosity medium have been presented by Wilson and Aifantis (1982) and expressed as:

$$\alpha = 1 - \frac{K}{K_m} = 1 - \frac{C_m}{C_{bc}} = \frac{C_{bc} - C_m}{C_{bc}} \quad (124)$$

where K is the bulk modulus and C_m and C_{bc} are rock matrix and bulk compressibility. Since $C_{bp} = C_{bc} - C_m$ and $C_{bc} = \frac{1}{K}$, substituting Biot's coefficient into Equation (123) results:

$$\varepsilon = \frac{\sigma}{2G} - \frac{v}{2G(1+v)} tr(\sigma)\mathrm{I} - \frac{\alpha}{3K} P_p \mathrm{I} \quad (125)$$

or

$$\sigma = 2G\varepsilon + \frac{v}{(1+v)} tr(\sigma)\mathrm{I} + \frac{2G}{3K} \alpha P_p \mathrm{I} \quad (126)$$

The shear modulus (G) is defines as:

$$2G(1+v) = 3K(1-2v) \quad (127)$$

After substituting shear modulus into Equation (125), the volumetric strain and mean normal stress can be written in a trace form as follows:

$$tr(\varepsilon) = \varepsilon_{xx} + \varepsilon_{yy} + \varepsilon_{zz} = \varepsilon_{vol} \quad (128)$$
$$= \frac{(1-2v)}{2G(1+v)} tr(\sigma) - \frac{\alpha}{K} P_p$$

or

$$tr(\sigma) = \sigma_{xx} + \sigma_{yy} + \sigma_{zz} = 3\bar{\sigma} \quad (129)$$
$$= \frac{2G(1+v)}{(1-2v)} tr(\varepsilon) + 3\alpha P_p$$

Substitutes Equation (129) into Equation (126) results equation relating stress and strain as follows:

$$\sigma = 2G\varepsilon + \frac{2Gv}{(1-2v)}tr(\varepsilon)\mathrm{I} + \frac{3v}{(1+v)}\alpha P_p\mathrm{I} + \frac{2G}{3K}\alpha P_p\mathrm{I} \qquad (130)$$

Now we introduce a lame parameter which is defined in term of the bulk and shear modulus as follows:

$$\lambda = K - \frac{2}{3}G = \frac{2Gv}{1-2v} = \frac{3Kv}{1+v} \qquad (131)$$

Re-apply the shear modulus, Equation (127) and lame parameter, Equation (131) into equation relating stress and strain, Equation (130) results the stress/strain behavior of an isothermal elastic material equation, which is described by Hooke's law for porous medium as follows:

$$\sigma = 2G\varepsilon + \lambda tr(\varepsilon)\mathrm{I} + \frac{3v}{(1+v)}\alpha P_p\mathrm{I} + \frac{(1-2v)}{(1+v)}\alpha P_p\mathrm{I} \qquad (132)$$

$$\sigma - \alpha P_p\mathrm{I} = 2G\varepsilon + \lambda tr(\varepsilon)\mathrm{I} \qquad (133)$$

Since a porous medium is a subject to change in both temperature and stress in a thermos-poro-elastic medium, McTigue (1986) added a pore pressure and temperature term in to Hooke's law to become:

$$\sigma - \alpha P\mathrm{I} - 3\beta_t K\left(T - T_{ref}\right)\mathrm{I} = 2G\varepsilon + \lambda tr(\varepsilon)\mathrm{I} \qquad (134)$$

where T_{ref} is reference temperature for a thermally unstrained state and β_t is linear thermal-expansion coefficient. Recall Equation (128), (129), and (131), so that Equation (133) can be written in non-matrix form as follows:

$$\bar{\sigma} - \alpha P_p - 3\beta_t K(T - T_{ref}) = \left(\lambda + \frac{2}{3}G\right)\varepsilon_{vol} \qquad (135)$$

$$\sigma_{kk} = \left[\alpha P_p + 3\beta_t K\left(T - T_{ref}\right)\right] + 2G\varepsilon_{kk} + \lambda\left(\varepsilon_{xx} + \varepsilon_{yy} + \varepsilon_{zz}\right) \qquad (136)$$

where the subscript $k = x, y, z$. The derivation is continued under the static equilibrium equation, where F_b is the body force as described as followed:

$$\nabla \cdot \sigma + F_b = 0 \qquad (137)$$

Substitute Equation (136) into Equation (137) to become:

$$\alpha \frac{\partial P}{\partial x} + 3\beta_t K \frac{\partial T}{\partial x} + 2G \frac{\partial \varepsilon_{xx}}{\partial x} + 2G \frac{\partial \varepsilon_{yx}}{\partial y} + 2G \frac{\partial \varepsilon_{zx}}{\partial z} + \lambda \frac{\partial}{\partial x}\left(\varepsilon_{xx} + \varepsilon_{yy} + \varepsilon_{zz}\right) + F_{bx} = 0 \qquad (138)$$

$$\alpha \frac{\partial P}{\partial y} + 3\beta_t K \frac{\partial T}{\partial y} + 2G \frac{\partial \varepsilon_{yy}}{\partial y} + 2G \frac{\partial \varepsilon_{xy}}{\partial x} + 2G \frac{\partial \varepsilon_{zy}}{\partial z} + \lambda \frac{\partial}{\partial y}\left(\varepsilon_{xx} + \varepsilon_{yy} + \varepsilon_{zz}\right) + F_{by} = 0 \qquad (139)$$

$$\alpha \frac{\partial P}{\partial z} + 3\beta_t K \frac{\partial T}{\partial z} + 2G \frac{\partial \varepsilon_{zz}}{\partial z} + 2G \frac{\partial \varepsilon_{xz}}{\partial x} + 2G \frac{\partial \varepsilon_{yz}}{\partial y} + \lambda \frac{\partial}{\partial z}\left(\varepsilon_{xx} + \varepsilon_{yy} + \varepsilon_{zz}\right) + F_{bz} = 0 \qquad (140)$$

Other fundamental equations in the linear elasticity theory, which are used to generate mean-stress geomechanical formula are the relation between the strain tensor (ε) and the displacement vector u as described as followed:

$$\varepsilon = \frac{1}{2}(\nabla u + \nabla u') \qquad (141)$$

The divergence of the displacement vector (∇u) is the sum of the normal strain component, which makes the volumetric strain as:

$$\nabla u = \frac{\partial u_x}{\partial x} + \frac{\partial u_y}{\partial y} + \frac{\partial u_z}{\partial z} = \varepsilon_{xx} + \varepsilon_{yy} + \varepsilon_{zz} = \varepsilon_{vol} \qquad (142)$$

After rearranging Equation (123) – (125) and combining with Equation (127) in term of displacement vector can be written as:

$$\alpha\frac{\partial P}{\partial x} + 3\beta_t K\frac{\partial T}{\partial x} + (G+\lambda)\left\{\frac{\partial^2 u_x}{\partial x^2} + \frac{\partial^2 u_y}{\partial y \partial x} + \frac{\partial^2 u_z}{\partial z \partial x}\right\} + G\left\{\frac{\partial^2 u_x}{\partial y^2} + \frac{\partial^2 u_x}{\partial x^2} + \frac{\partial^2 u_x}{\partial z^2}\right\} + F_{bx} = 0 \quad (143)$$

$$\alpha\frac{\partial P}{\partial y} + 3\beta_t K\frac{\partial T}{\partial y} + (G+\lambda)\left\{\frac{\partial^2 u_y}{\partial y^2} + \frac{\partial^2 u_x}{\partial x \partial y} + \frac{\partial^2 u_z}{\partial z \partial y}\right\} + G\left\{\frac{\partial^2 u_y}{\partial x^2} + \frac{\partial^2 u_y}{\partial y^2} + \frac{\partial^2 u_y}{\partial z^2}\right\} + F_{by} = 0 \quad (144)$$

$$\alpha\frac{\partial P}{\partial z} + 3\beta_t K\frac{\partial T}{\partial z} + (G+\lambda)\left\{\frac{\partial^2 u_z}{\partial z^2} + \frac{\partial^2 u_x}{\partial z \partial x} + \frac{\partial^2 u_y}{\partial z \partial y}\right\} + G\left\{\frac{\partial^2 u_z}{\partial x^2} + \frac{\partial^2 u_z}{\partial y^2} + \frac{\partial^2 u_z}{\partial z^2}\right\} + F_{bz} = 0 \quad (145)$$

For the shorter, Equation (143) – (145) can be written as the equilibrium equation as follows:

$$\alpha\nabla P + 3\beta_t K\nabla T + (\lambda+G)\nabla(\nabla\cdot u) + G\nabla^2 u + F_b = 0 \quad (146)$$

For dual porosity medium which consist of a network of fracture and rock matrix, the thermos-multi-poro-elastic Navier equation is obtained using a summation over multi-porosity continua, where each temperature term is weighted by the porous continuum volume fracture (ω_j), as follows:

$$\nabla\left[\sum_j \left(\alpha_j P_j + 3\beta_t K\omega_j T_j\right)\right] + (\lambda+G)\nabla(\nabla\cdot u) + G\nabla^2 u + F_b = 0 \quad (147)$$

Taking the divergence of previous equation yields

$$\nabla^2\left[\sum_j\left(\alpha_j P_j + 3\beta_t K\omega_j T_j\right)\right] + (\lambda + 2G)\nabla^2(\nabla\cdot u) + \nabla\cdot F_b = 0 \qquad (148)$$

By substituting the volumetric strain from Equation (135) and (142) into Equation (148) resulting:

$$\nabla^2\left[\sum_j\left(\alpha_j P_j + 3\beta_t K\omega_j T_j\right)\right] + (\lambda + 2G)\nabla^2\left\{\frac{\bar{\sigma} - \alpha P_p - 3\beta_t K(T - T_{ref})}{\left(\lambda + \frac{2}{3}G\right)}\right\} + \nabla\cdot F_b = 0 \qquad (149)$$

After substituting the relationship between Poisson's ratio and shear modulus, Equation (127) and the lame parameter, Equation (131), and continue with Equation (149), we obtain the governing geomechanical equation:

$$\frac{3(1-v)}{1+v}\nabla^2\bar{\sigma} - \frac{2(1-2v)}{1+v}\left[\sum_j\left\{\alpha_j\nabla^2 P_j + 3\beta_t K\omega_j\nabla^2 T_j\right\}\right] + \nabla\cdot F_b = 0 \qquad (150)$$

n